Comparison of alkane activation over supported and bulk transition metal oxide catalysts and transition metal free carbon nano structures

vorgelegt von
Diplom-Chemiker
Pierre Kube
geboren in Berlin

von der Fakultät II – Mathematik und Naturwissenschaften
der Technischen Universität Berlin
zur Erlangung des akademischen Grades

Doktor der Naturwissenschaften
Dr. rer. nat.

genehmigte Dissertation

Promotionsausschuss:

Vorsitzender: Prof. Dr. Martin Lerch
Gutachter: Prof. Dr. Robert Schlögl
Gutachter: Prof. Dr. Reinhard Schomäcker
Gutachter: Prof. Dr. Klaus Rademann

Tag der wissenschaftlichen Aussprache: 11. Juni 2018

Berlin, 2018

Acknowledgement

First and foremost, I would like to express my sincere thanks to Professor Dr. Robert Schlögl, Director of the Department of Inorganic Chemistry at the Fritz Haber Institute of the Max Planck Society. Your immense support and claim for a continuous development of my knowledge taught me to take never anything for granted and question always everything.

Secondly, I am deeply thankful to my supervisor, Dr. Annette Trunschke, for her continuous support, many discussions and great ideas. Your invested time improved my scientific skills and helped me to develop a critical eye about my own and other works.

My very special thanks goes to the additional PhD Committee members Prof. Dr. Reinhard Schomäcker and Prof. Dr. Klaus Rademann for reviewing my thesis. Additional gratitude goes to Prof. Dr. Martin Lerch for taking the chair of the examination board.

A big word of thank goes to Dr. Benjamin Frank for discussing kinetic data and helping with the reactors for catalytic measurements.

Furthermore, I thank following colleagues (in no particular order) for performing experiments, technical assistance and discussions: Dr. Sabine Wrabetz (microcalorimetry), Dr. Johannes Noack (Raman), Jutta Kröhnert (IR), Dr. Benjamin Frank (catalytic setups, synthesis, and discussions), Dr. Juan Velasco-Vélez (XPS), Dr. Michael Hävecker (XPS), Gisela Lorenz (N_2 physisorption), Maike Hashagen (N_2 physisorption), Achim Klein-Hoffmann (XRF), Olaf Timpe (XRF), Dr. Frank Girgsdies (XRD), Gisela Weinberg (SEM), Dr. Maricruz Sanchez-Sanchez (synthesis), and Dr. Till Wolfram (synthesis).

I also thank my current and previous office mates and the members of the “Reactivity group” for the warm atmosphere and inspiring discussions.

Finally I thank my dear wife for her patience and my sons for fruitful discussions.

Eidesstattliche Versicherung

Hiermit versichere ich, Pierre Kube, dass die vorgelegte Dissertation von mir selbständig angefertigt wurde. Alle von mir genutzten Hilfsmittel und Hilfen, sowie wörtlich oder dem Sinn nach übernommene Stellen anderer Veröffentlichungen sind kenntlich gemacht. Eine Auflistung der in den einzelnen Kapiteln verwendeten Originalquellen befindet sich am Ende eines jeden Kapitels.

Die Arbeit ist in Zusammenarbeit mit anderen Wissenschaftler(inne)n entstanden und im Folgenden erfolgt eine Auflistung dieser.

Dr. Annette Trunschke
Dr. Sabine Wrabetz
Dr. Johannes Noack
Jutta Kröhnert
Dr. Raoul Naumann
Dr. Benjamin Frank
Dr. Juan Velasco-Vélez
Dr. Michael Hävecker

Inhalte der Dissertation wurden und werden nicht in gleicher oder abgewandelter Form für andere Promotionen verwendet.

Abstract

Vanadium-based and transition metal-free catalysts have been extensively studied during the last decades in the partial oxidation of ethane and propane due to the high activity and good selectivity. The selectivity to the desired olefin is, however, still too low for industrial application. Improvements require at first an in-depth understanding of the entire reaction network and the relation of desired and undesired pathways to surface and bulk properties of the catalyst.

In the present thesis, the reaction network of ethane and propane oxidation was investigated under equal reaction conditions on three different catalysts, namely crystalline MoVTeNb oxide with orthorhombic M1 structure, sub-monolayer vanadium oxide supported on mesoporous silica (V_xO_y/SiO_2), and functionalized carbon nanotubes (P/oCNT) that contain no redox active metal and bulk oxygen. Catalytic performance and kinetic modelling indicate similarities in the reaction network over all three catalysts implying that differences in selectivity in the investigated range of reaction conditions are the result of different rate constants of the individual reaction pathways over the three catalysts. Different rates for alkane activation are attributed to differences in the density of alkane adsorption sites. Electronic structure and surface dynamics of the catalysts have an influence on oxygen activation and individual reaction steps. Barriers for propane activation, experimentally estimated using adsorption enthalpies and apparent activation energies, increase in the order P/oCNT (139 kJ mol^{-1}) ≤ M1 (143 kJ mol^{-1}) < V_xO_y/SiO_2 (162 kJ mol^{-1}).

A deeper investigation of the reaction network in propane oxidation, with respect to the number of formed products, propane activation, and formation pathways of carbon oxides was performed over MoVTeNb oxide and V_xO_y/SiO_2. Temperature programmed reaction reveals the same 12-13 intermediates in propane oxidation over the two catalysts that can be desorbed into the gas phase, suggesting that the reaction network is similar. Kinetic isotope effect measurements for native and deuterium labelled propane under steady state conditions imply a quasi-simultaneous hydrogen abstraction over MoVTeNb oxide on neighbouring surface sites and a stepwise hydrogen abstraction over V_xO_y/SiO_2. Experiments with ^{13}C labelled propane indicate that oxygen insertion into the CHO group of acrolein under formation of acrylic acid is faster over MoVTeNb oxide than oxidation at the CH_2 group and decarbonylation to acetaldehyde. Sub-monolayer vanadium oxide supported on silica shows the opposite behaviour.

In summary, the results of the thesis contribute to the establishment of catalyst design concepts, which can lead to improved selectivity in oxidation of alkanes.

Zusammenfassung

Vanadium-basierte und übergangsmetallfreie Katalysatoren wurden während der letzten Jahrzehnte wegen ihrer hohen Aktivität und guten Selektivität intensiv in der partiellen Oxidation von Ethan und Propan untersucht. Die bislang erreichte Selektivität rechtfertigt eine industrielle Anwendung jedoch noch nicht. An erster Stelle in der Forschung steht daher das Ziel, das vollständige Reaktionsnetzwerk aufzuklären und die Verbindung der einzelnen Reaktionspfade zu Oberflächen- und Volumeneigenschaften des Katalysators zu verstehen.

In der vorliegenden Dissertation wurden die Reaktionsnetzwerke der Ethan- und Propanoxidation unter gleichen Reaktionsbedingungen an drei verschiedenen Katalysatoren untersucht: kristallines MoVTeNb-Oxid mit orthorhombischer M1 Struktur, Vanadiumoxid-Submonolagen auf mesoporösem Siliciumdioxid (V_xO_y/SiO_2) und funktionalisierte Kohlenstoffnanoröhren (P/oCNT), die kein redoxaktives Metall sowie Gittersauerstoff enthalten. Katalysatorleistung und kinetische Modellierung zeigen Gemeinsamkeiten im Reaktionsnetzwerk der drei Katalysatoren, weshalb Selektivitätsunterschiede mit unterschiedlichen Geschwindigkeitskonstanten der einzelnen Reaktionspfade erklärt werden. Aktivitätsunterschiede werden auf verschiedene Dichten an Alkan-Adsorptionsplätzen zurückgeführt. Elektronische Struktur und Oberflächendynamik haben Einfluss auf die Sauerstoff-Aktivierung. Barrieren für die Propan-Aktivierung, die experimentell aus Adsorptionsenthalpien und scheinbaren Aktivierungsenergien abgeschätzt wurden, nehmen in der Reihenfolge P/oCNT (139 kJ mol^{-1}) ≤ M1 (143 kJ mol^{-1}) < V_xO_y/SiO_2 (162 kJ mol^{-1}) zu.

Eine weitergehende Untersuchung des Reaktionsnetzwerkes der Propanoxidation, bezüglich der Anzahl gebildeter Produkte, der Propan-Aktivierung und den Bildungswegen von CO und CO_2 wurde an MoVTeNb-Oxid und Vanadiumoxid-Submonolage auf Siliciumdioxid durchgeführt. Temperaturprogrammierte Reaktionsexperimente deuten auf Ähnlichkeiten in den Netzwerken hin, da die selben Zwischenprodukte gebildet werden. Messungen des kinetischen Isotopeneffektes für natives und Deuterium-markiertes Propan unter stationären Bedingungen deuten auf eine quasi-simultane Wasserstoffabstraktion an MoVTeNb-Oxid hin, wohingegen die Wasserstoffabstraktion an V_xO_y/SiO_2 schrittweise erfolgt. Experimente mit ^{13}C markiertem Propan zeigen, das die Sauerstoffinsertion in die CHO-Gruppe von Acrolein unter Bildung von Acrlysäure an MoVTeNb-Oxid schneller ist, als die Oxidation an der CH_2-Gruppe und die Decarbonylierung zu Acetaldehyd. Vanadiumoxid-Submonolage auf Siliciumdioxid zeigt das entgegengesetzte Verhalten.

Die Erkenntnisse dieser Arbeit tragen dazu bei, neue Designkonzepte für selektivere Oxidationskatalysatoren entwerfen zu können.

Table of contents

Chapter 1 Introduction

1.1 Oxidative dehydrogenation of short-chain hydrocarbons

The demand for light olefins, especially ethylene and propylene, and their supply shortage is a consequence of the extensive use of these compounds as monomers/co-monomers and the relative decrease in production capacity triggered by changes in operation conditions, respectively. At the moment, the main production routes of olefins are steam cracking, fluid-catalytic-cracking (FCC) and catalytic dehydrogenation, which are characterized by certain limitations.[1] Steam cracking and FCC mainly produce ethylene, which is not in line with the forecasted market demand, because the demand rate of ethylene grows slower compared to propylene. Thermodynamic restriction during catalytic dehydrogenation limits the conversion. Steam cracking is a strong endothermic reaction and needs the supply of heat at high temperature. Formation of coke during catalytic dehydrogenation and steam cracking results in catalyst and reactor fouling. Complicated product separation is needed for all three processes, due to side reactions and by-products formation.

An attractive reaction, which overcomes most of the drawbacks, is the oxidative dehydrogenation of ethane (ODE) and propane (ODP). Introduction of oxygen into the reaction mixture leads to the formation of water instead of hydrogen. As a consequence, the reaction becomes exothermic and can be operated at lower temperatures. Side reactions (cracking of alkanes and coke formation) are minimized or completely suppressed and thermodynamic limitations don't exist longer. In spite of these advantages, the ODH has some significant drawbacks that prevent its implementation at an industrial scale: difficult control of the consecutive oxidation to carbon oxides, removal of reaction heat, flammability of the reaction mixture, and the possibility of a reaction runaway. The demand requires the development of a catalyst with improved selectivity to olefins at high conversion and reduced carbon oxide formation.

Applied ODH catalysts show often higher activities in ODP compared to ODE, which leads to usually lower applied reaction temperatures for ODP than for ODE. The hypothesis that the bond breaking of the different types of C-H bonds in ethane (methyl -423 kJ mol^{-1}) and propane (methyl -422 kJ mol^{-1}; methylene -412.5 kJ mol^{-1}) are the main reason for the observed different activities seems to be not true, because various carbon based catalysts, studied by Frank *et al.*,[2] and vanadia and molybdena supported on TiO_2 or γ-Al_2O_3, studied by Heracleous *et al.*[3] show nearly equal apparent activation energies for ethane and propane consumption (Table 1-1). Another possibility

for activity differences in the ODE and ODP could be different adsorption properties / sites for ethane and propane at the same catalyst surface.

Table 1-1 Apparent activation energy (E_a) for ethane and propane consumption.

Catalyst	$E_{a,\ ethane}$ [kJ mol^{-1}]		$E_{a,\ propane}$ [kJ mol^{-1}]	Ref.
o-CNTs	100	>	72	2
B-oCNTs	108	≈	101	2
P-oCNTs	110	≈	105	2
5VTi	67	≈	70	3
14VAl	85	≈	80	3
5MoTi	104	>	97	3
15MoAl	91	≈	87	3

With respect to selectivity, ethylene is unique in the series of olefins, because it contains only vinylic C-H bonds (464 kJ mol^{-1})[4] that are stronger than the bonds in ethane and one could expect a high selectivity to this product. In contrast to that, propylene has additional to the vinylic C-H bonds also methyl C-H bonds (369 kJ mol^{-1}),[4] which are weaker than the bonds in propane, and could therefore be activated more easily than bonds in propane, promoting secondary reactions.[5]

Main products in the oxidative dehydrogenation of ethane and propane are the desired olefins ethylene and propylene and the undesired carbon oxides CO and CO_2. Oxygenated products like acetaldehyde, acetic acid, acrylic acid, acetone, acrolein, and propionaldehyde are only rarely reported for ODE and ODP catalysts.[6,7,8,9] Based on the products that are found, different reaction networks are reported in the literature. The simplest reaction network (Figure 1-1) that contains only the alkane with corresponding olefin and the carbon oxides (CO and CO_2) is very often reported in the literature and the basis for most kinetic modelling studies.[1,10]

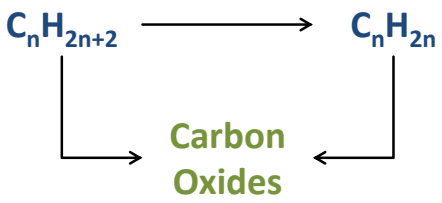

Figure 1-1 Simplest reaction network for oxidative dehydrogenation of hydrocarbon, including alkane, olefin and carbon oxides.

The simplicity of the approach allows an easy and fast analysis of measured catalyst performance for the investigated parameter space. Predictions out-side of the parameter space with the simple approach are little satisfactorily. Nor does it help to identify kinetic reasons for low selectivity.

1.2 Catalysts for oxidative dehydrogenation of ethane and propane

Several types of catalysts were reported for the ODH of propane and ethane[11,12] and can be divided into bulk metal oxides, supported metal oxides, and metal free catalysts.[1,11]

Transition metal oxides, containing often V or Mo as the active component, have been investigated in the oxidative dehydrogenation as bulk metal oxide and supported metal oxide catalysts. MoVTeNb oxide with M1 phase is a well known example for bulk metal oxides with high activity in the conversion of short chain alkanes.[13,14,15,16,17,18,19] Typical representative for supported systems is vanadia supported on mesoporous silica SBA-15 that shows good performance in oxidative dehydrogenation of propane.[20,21] A new group of catalysts for ODH reactions are nanostructured carbons, like carbon nanotubes (CNTs) that represent a sustainable metal-free alternative to metal oxide catalysts.[2,22,23,24,25,26,27] Oxidized CNTs, impregnated with P_2O_5 to improve the thermal stability, is a catalyst with moderate activity and high selectivity to olefins.

Activity and selectivity of the catalysed ODH reactions are not only a result of the chosen catalyst but also of the selected reaction conditions.[1,11,12] Consequently, the great variety of published catalysts for ODE and ODP cannot be compared among each other due to differences in the applied reaction conditions. Among the numerous catalysts suitable for the oxidative transformation of short chain alkanes, it appears that the best catalytic active materials for the ODH of ethane (ODE) are poor in the ODH of propane (ODP) and vice versa.

1.3 Different aspects in the reaction mechanism of propane ODH

1.3.1 Activation of propane

Activation of propane by C-H bond cleavage is assumed to be a rate determining step (RDS) in the ODH of propane. Cleavage of the methylene C-H bonds (D°298 = 411 kJ mol^{-1}) is proposed to be the initial step, due to the weaker bond strength than for methyl C-H bonds (D°298 = 422 kJ mol^{-1}).[28,29] Quantum chemical calculations on molybdenum and vanadium oxide based systems reveal that H abstraction at the methylene group by terminal oxygen M=O (M = V or Mo) is the most feasible reaction pathway.[30,31] Exchange of hydrogen by deuterium at selected positions in propane was used to probe, if C-H bond cleavage is a RDS in the reaction mechanism by studying the isotope effect on reaction rates. The large mass differences of H vs. D and the differences in the bonding energies of C-H vs. C-D bond result in kinetic and thermodynamic differences.[32,33,34] The reasons are different zero point energies (ground state) of C-H and C-D bonds ($E_{C-D} < E_{C-H}$).[33] Measurement of the kinetic isotope effect (KIE, defined as the ratio of $k_{i,C-H}/k_{i,C-D}$) using $CH_3CH_2CH_3$, $CH_3CD_2CH_3$ or $CD_3CD_2CD_3$ as reactants and comparison among each other gives information, whether methylene or methyl C-H bond cleavage are kinetically relevant. For instance, if $CH_3CD_2CH_3$ reacts slower than $CH_3CH_2CH_3$, then methylene C-H bond dissociation has an influence on the reaction kinetic. Slower reaction rates for $CD_3CD_2CD_3$ than for $CH_3CD_2CH_3$ indicate that breaking of methyl C-H bonds are rate-determining for the reaction. Equal reaction rates would indicate that the respective position is kinetically irrelevant.

Stern and Grasselli measured the KIE for the oxidative dehydrogenation of propane and for the partial oxidation of propylene over $Ni_{0.5}Co_{0.5}MoO_4$ and $Mg_4V_2Sb_2O_x$ catalysts using $CH_3CH_2CH_3$ and $CD_3CD_2CD_3$.[8] They obtained KIE values greater than 1, confirming that C-H bond breaking is kinetically relevant for the partial oxidation of propane and propylene. Chen *et al.* could show that C-H bond dissociation of the methylene is a kinetically relevant step (KIE's > 1) in the ODP over 10 wt% VO_x/ZrO_2[57] and 11 wt% MoO_x/ZrO_2[35] (Table 1-2).

Adsorption of propane at the catalyst surface is rarely the object of scientific research, although it is an important part of the propane activation. Frank *et al.* investigated propane adsorption on two different CNT catalysts (CNTs and B_2O_3-CNTs) and observed initial differential heats of about 45 and 40 kJ mol^{-1}, which they assigned to adsorption on oxygen surface groups.[2] Readsorption yields nearly the same initial heats, indicating no crucial changes/modifications of the adsorption sites.

Theoretical calculations on supported vanadium oxide species and MoVTeNb oxide cluster showed weak propane adsorption.[36,37]

Table 1-2 Kinetic Isotope Effects over 10 wt% VO_x/ZrO_2 Catalyst (593 K, 14.2 kPa Propane, 1.7 kPa O_2, balance He) and 11 wt% MoO_x/ZrO_2 Catalyst (688 K, 14.2 kPa Propane, 1.7 kPa O_2, balance He).[35,57]

Isotope	$CH_3CH_2CH_3$/ $CD_3CD_2CD_3$	$CH_3CH_2CH_3$/ $CH_3CD_2CH_3$	$CH_3CD_2CH_3$/ $CD_3CD_2CD_3$
10 wt% VO_x/ZrO_2 Catalyst			
Primary dehydrogenation, $k_{1,C-H}/k_{1,C-D}$	2.8	2.7	1.0
Secondary combustion, $k_{3,C-H}/k_{3,C-D}$	2.6	1.1	2.5
Primary combustion, $k_{2,C-H}/k_{2,C-D}$	1.9	1.8	1.1
11 wt% MoO_x/ZrO_2			
Primary dehydrogenation, $k_{1,C-H}/k_{1,C-D}$	2.3	1.7	1.4
Secondary combustion, $k_{3,C-H}/k_{3,C-D}$	2.1	1.1	1.8
Primary combustion, $k_{2,C-H}/k_{2,C-D}$	1.6	1.3	1.2

1.3.2 Interaction of propylene with the catalyst surface

Investigation of the interaction of propylene with the catalyst surface is very limited in the literature. Chen *et al.* investigated the interaction of formed propylene with a 4 wt% VO_x/ZrO_2 catalyst by using a feed of $C_3H_8/C_3D_8/O_2$/He (7.1/7.1/7.1/balance) and obtained a binominal distribution of deuterium in propylene as a result of H/D exchange with the surface. H/D exchange in propylene was also observed when D_2O was added to a C_3H_8/O_2 reaction mixture. The results prove a pronounced hydrogen mobility at the catalyst surface and an unavoidable interaction of propylene with the VO_x/ZrO_2 catalyst.

Frank *et al.* studied propylene adsorption on CNTs and B_2O_3-CNTs and found out that propylene adsorbs with slightly higher initial heats of adsorption (+5 kJ mol^{-1}) than propane.[2] During

propylene adsorption the CNT-catalyst changes, because the adsorption profile of readsorption is different than for the first cycle.

1.3.3 Formation pathways of total oxidation products CO and CO_2

Studies on the formation pathways of CO and CO_2 are often part of kinetic measurements with the aim to identify if CO or CO_2 are primary and/or secondary products. Another possibility for investigating the formation pathways of CO and CO_2 is the use of ^{13}C labeled propane. Chen *et al.* used ^{13}C labeled propane at the methylene position (^{13}C-2-propane) in the ODH of propane on 15 wt% VO_x/ZrO_2[58] and 11 wt% MoO_x/ZrO_2[35] together with unlabeled propylene (ratio of ^{13}C-2-propane/unlabeled propylene = 5). On VO_x/ZrO_2, CO is produced via propylene combustion, whereas CO_2 comes from combustion of propane and propylene. MoO_x/ZrO_2 forms CO and CO_2 via combustion of propane and propylene.

1.4 Reaction networks over selected catalysts for ODH of ethane and propane

1.4.1 MoVTeNb oxide with M1 structure

The complex mixed oxide of molybdenum, vanadium, tellurium and niobium with the so called M1 phase (ICSD no. 55097) is active and selective in the ammoxidation of propane to acrylonitrile,[14] partial oxidation of propane to acrylic acid,[13,15,16] and oxidative dehydrogenation of ethane[17,18] and propane.[19] In the crystal structure of the M1 phase (unit cell comprises 44 metal atoms) corner-linked MO_6 (M = Mo, V) octahedra are arranged in 6- and 7-membered rings that are partially filled by tellurium oxide. Niobium is most likely in the centre of the MO_7 pentagonal bipyramidal unit, which shares edges with the surrounding octahedra. The (001) planes are stacked on top of each other forming a bronze like structure similar to $Cs_{0.7}(Nb_{2.7}W_{2.3})O_{14}$ (ICSD 67974[38]).[39]

The efficiency of M1 was originally attributed to the distortion of the octahedral units on its terminating basal plane[40] towards the open channels. It was also considered that vanadyl groups at the crystallographic positions M3 and M7 of the terminating plane could be responsible for C-H activation of propane.[41,42] A verification of this hypothesis by a series of experiments gave conflicting results.[43,44,45]

Recent results suggest that M1 is a self-supporting system forming an active monolayer under reaction conditions with a different chemical composition compared to the bulk. This active monolayer shows a dynamic behavior of Te^{4+} and V^{5+} sites in connection with changes of the

chemical potential of the feed in the partial oxidation of propane to acrylic acid.[46,47] The active sites in the formed active monolayer probably consist of V_xO_y species with strictly 2D structure.[48] Apparently, these active sites with their strictly 2D nature, survive the internal structural dynamics during the catalytic redox cycle. It is also considered that the active monolayer works as a shield to protect the M1 matrix from reactive molecules resulting in high stability of the bulk phase. One explanation therefore gives the developed model by Eichelbaum *et al*. in which the active monolayer acts as a chemical diode for separating the free charge carriers of the semiconducting M1 from active sites.[49] This leads to a slowdown of electron transfer between bulk and monolayer preventing simultaneous activation of O_2 and formation of electrophilic oxygen species, which cause total oxidation of hydrocarbons.

Figure 1-2 shows the proposed reaction network for propane oxidation over phase pure M1 MoVTeNb oxide proposed by Naumann *et al*.[46] First step is the formation of a surface alkoxide intermediate that can be transformed into propylene by abstraction of a second hydrogen atom. Decomposition of the alkoxide to CO is a reaction pathway with minor relevance. Propylene is transformed into acrylic acid via allylic oxidation in a subsequent step. Acrylic acid can be decarboxylated into CO_2 and ethylene, which is an undesired pathway. Formed ethylene can be further oxidized to acetic acid, where the latter is totally oxidized to CO or CO_2. The proposed reaction network in Figure 1-2 is probably much simpler than the real reaction network over M1.

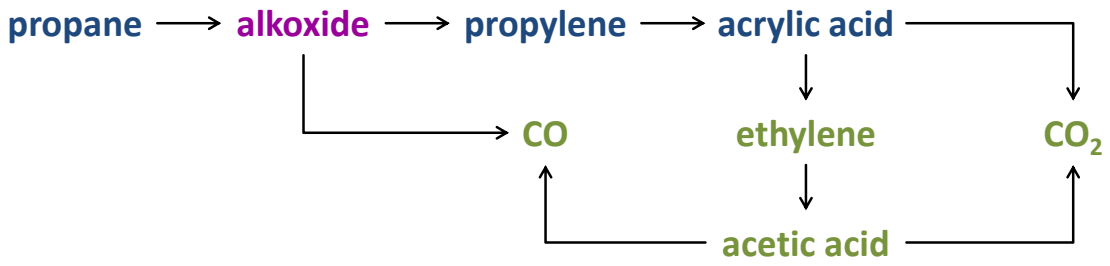

Figure 1-2 Proposed reaction network of propane oxidation over phase-pure M1 MoVTeNb oxide.[46]

In ethane oxidation over M1, formation of acetic acid is only a minor reaction pathway in the whole reaction network while formation of ethylene is the main route. Reason for this might be the high strength of the vinylic C-H bonds of ethylene compared to the C-H bonds of ethane. The use of ethanol instead of ethane as reactant avoids these kinetic hurdles and enables an insight into the formation pathway of acetic acid.[50,51] Sobolev *et al.* could show that a MoVTeNb mixed oxide is a

good catalyst for oxidation of ethanol to acetic acid with high yields.[51] Figure 1-3 shows a proposed reaction network for ethanol oxidation over a MoVNb oxide supported on TiO_2 by Li *et al.*[50] Transformation of ethanol into acetic acid takes place via the intermediate product acetaldehyde. Formation of ethyl acetate from acetic acid is possible as long as adequate amounts of ethanol are present. CO and CO_2 can be formed from all C_2 oxygenates.

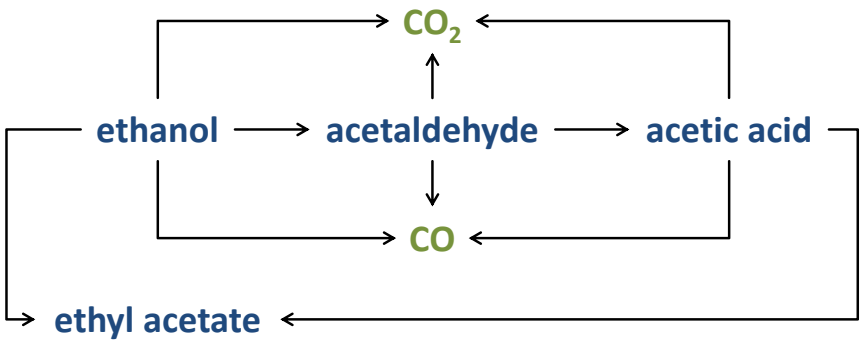

Figure 1-3 Proposed reaction network of ethanol oxidation over a MoVNb oxide supported on TiO_2.[50]

The results of Sobolev *et al.* and Li *et al.* suggest that the formation of acetic acid in the reaction network of ethane oxidation runs via the intermediate product acetaldehyde.

1.4.2 Vanadium oxide supported on mesoporous silica SBA-15

Vanadia supported on mesoporous silica SBA-15 is a well-known active and selective catalyst for the oxidative dehydrogenation of propane.[21] The mesoporous SBA-15 has uniform hexagonal channels with a narrow pore size distribution.[52,53] The large surface area of SBA-15 allows to deposit a large amount of well-defined 2D vanadia species at the surface including monomeric species without V-O-V bonds and oligomers with different chain lengths. A recent study shows that similar structures composed of monomeric and polymeric tetrahedral V_xO_y species are achieved on the dehydrated material up to a loading of 3.1 V nm^{-2}.[21] The ratio between monomeric and oligomeric species can be tuned by the amount of vanadia. A loading above 3.1 V nm^{-2} can lead to the formation of not only tetrahedral V_xO_y but also of 3D vanadia species.

Vanadium-oxygen-silicon bonds have been proposed as the catalytic active sites for the abstraction of hydrogen from the methylene group during ODP, which is considered a rate determining step.[54] Areas with no vanadia loading are supposed to be the cause of primary and secondary

combustion.[55,56] The similar structures of V_xO_y species of low loaded catalyst ($\leq$ 3.1 V nm^{-2}) are reflected in the catalytic performance of these catalysts in the ODH of propane.[21] Determined apparent activation energies as well as reaction orders of propane and oxygen for these materials show no large deviations.[21] The transition in the degree of oligomerization of the vanadia species between 2V atoms nm^{-2} with dominating monomeric species and 3V atoms nm^{-2} with dominating oligomeric species, show no qualitative changes in reactivity. For high loaded samples it was observed that the apparent activation energy changes with reaction conditions. This behaviour reflects probably structural changes during time on stream of the vanadia species between amorphous, bulk-like and two-dimensional highly dispersed species.[21]

Figure 1-4 shows the proposed reaction network for the oxidative dehydrogenation of propane over V_2O_5 supported on ZrO_2 (10 wt%) by Chen *et al.*[57,58] The reaction takes place via parallel and sequential oxidation steps and shows that propylene is directly formed from propane. Both propane and propylene can be transformed into carbon oxides (CO and CO_2). Chen *et al.* showed that the overall reaction rate is dependent on the partial pressure of propane (reaction order of 1) and independent on the oxygen partial pressure (reaction order of 0).

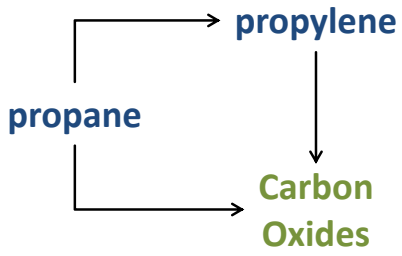

Figure 1-4 Proposed reaction network for the oxidative dehydrogenation of propane over V_2O_5 supported on ZrO_2 (10 wt%).[57,58]

Oyama *et al.*[6] studied the kinetics of ethane oxidation on a V_2O_5 supported SiO_2 catalyst and proposed a reaction network based on their observed products, which is shown in Figure 1-5. Conversion of ethane runs via three reaction pathways, one to the desired product ethylene and two other to the undesired products acetaldehyde and carbon oxides (CO and CO_2). Ethylene can be further oxidized to both undesired products. Acetaldehyde can be also transformed into carbon oxides. Investigation of the dependence of the partial pressure for ethane, oxygen and water on the

individual product formation rates yielded positive reaction orders for ethane (1 to 1.2) and oxygen (0.1) and a negative reaction order for water (-0.5 to -1.2).

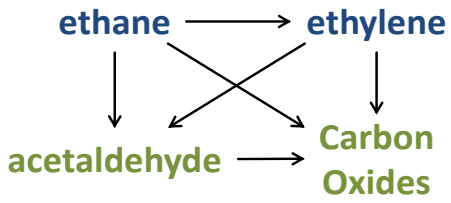

Figure 1-5 Proposed reaction network for ethane oxidation over a V_2O_5 supported on SiO_2.[6]

1.4.3 Oxidized carbon nano tubes stabilized with phosphorous oxides

CNTs based catalysts are a young group of catalytic active materials for ODH reactions that comprise an attractive metal-free alternative to metal oxide systems. These tubes consist of one or more concentrically arranged bent graphene layers (denoted as single wall or multi wall CNTs, respectively) with open or closed ends.[59,60] Typical diameters of single wall and multiwall CNTs are in a range of 0.8 to 2 nm and 5 to 20 nm,[61] respectively, but can also exceed 100 nm in the case of multiwall CNTs. The lengths of CNTs can vary between less than 100 nm up to several centimetres. Ideal CNTs are those in which all carbon atoms are bonded in a hexagonal lattice except at their ends. Pentagons, heptagons and other imperfections in the sidewalls as well as oxygen functional groups on the surface are defects in the structure, which influence macroscopic properties (e.g. thermal and electronic conductivities, combustibility, redox properties). The different oxygen containing functional groups on the surface are interesting due to their ability of catalysing different reactions. The abundance of the functional groups can be controlled by synthesis.

Electron rich groups, like ketonic and quinoidic groups, are proposed to be the active sites for the oxidative dehydrogenation of hydrocarbons.[2,22,23,24,25,26,27] It is proposed that these groups abstract hydrogen from alkanes to form the corresponding alkenes. Oxidation with O_2 of the resulting phenolic groups leads to the formation of the original groups and water. [22,23] Figure 1-6 shows the proposed reaction network for the oxidative dehydrogenation of alkanes over functionalized CNTs. Such a reaction network can also be found for other carbon materials like carbon nanofilaments.[62]

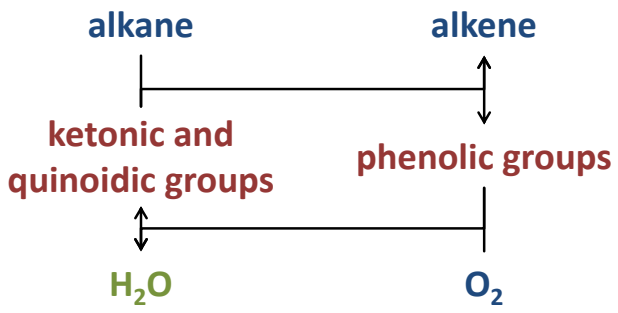

Figure 1-6 Proposed reaction network for the oxidative dehydrogenation of alkanes over functionalized CNTs.[23]

Disadvantage of CNT catalysts is the propensity towards combustion under oxidative conditions during ODH reaction with electrophilic oxygen containing groups as intermediate. These electrophilic groups can cause the combustion of hydrocarbons by attack at the carbon chain. Modification of the CNTs with B_2O_3 or P_2O_5 decreases the combustibility with simultaneous enhancement of the alkene selectivity due to the suppression of electrophilic groups.[23]

1.4.4 The different oxygen species of the selected catalysts

One main difference between all three catalyst types is the number and nature of different oxygen species in the catalysts, which can have different influence on the catalysed reaction. The M1 phase of MoVTeNb oxide has following different oxygen species, namely bulk oxygen, surface bridging oxygen and terminal oxo groups in the (dynamic) active surface layer. The role of the bulk oxygen during the catalytic cycle is still unclear. One possibility could be that the bulk phase acts as an oxygen reservoir to transport oxygen to the surface during the catalytic cycle. Surface bridging oxygen and terminal oxo groups on the surface are part of the (dynamic) active monolayer, which contains the active sites for the catalysis.

Vanadia supported on mesoporous silica SBA-15 has three different catalytic relevant oxygen species, which are bridging oxygen between a vanadium and a silicon (V-O-Si), bridging oxygen of the polymeric vanadia species (V-O-V), and oxygen of the vanadyl group (V=O). It is assumed that the latter two oxygen species are involved in the activation of hydrocarbons during ODH.[30,36,54] Oxygen from silica (Si-O-Si) shows no relevance for the partial oxidation of hydrocarbons.

In contrast to metal oxide systems, carbon materials are equipped with functional groups at surface edges and defects, such as carboxylic, phenol, ketone, lactone, ether, and quinonic groups and no bulk oxygen.[63] Comparing these functional groups with terminal groups of metal oxide catalysts,

e.g. on vanadia, similar types can be found, like terminal hydroxyl groups, bridging oxygen and terminal oxygen (Figure 1-7).

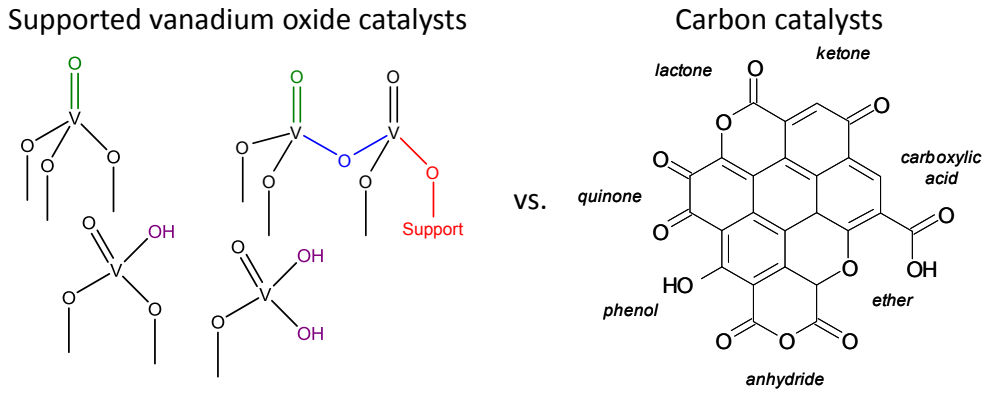

Figure 1-7 Comparison of functional groups of vanadium oxide catalysts with carbon catalysts.

Relevant functional groups for the oxidative dehydrogenation of hydrocarbons are the ketone and quinone groups.[64] Figure 1-8 shows a simplified comparative scheme for the different amount of oxygen species in the three catalysts.

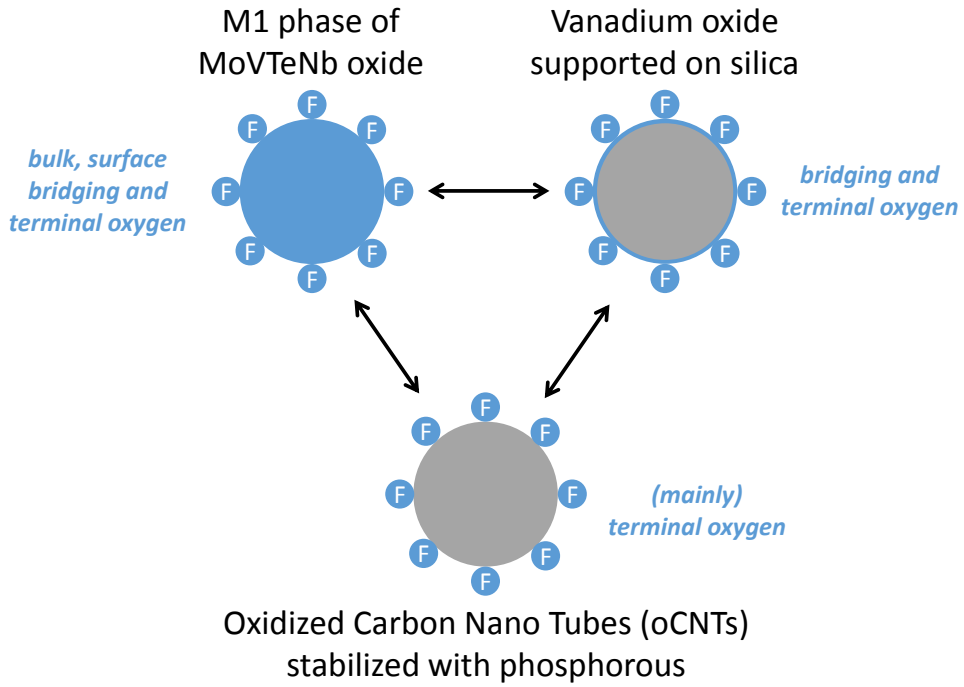

Figure 1-8 Simplified illustration of the three catalyst types with their different oxygen species (blue coloured parts = location of oxygen species; F = functional group).

1.4.5 Electronic properties of the selected catalysts

Another main difference between the three selected catalysts are their electronic properties. The M1 phase of MoVTeNb oxide shows the electronic properties of a n-type semiconductor in which the concentration of electrons is higher than the hole concentration. In n-type semiconductors, this excess of electrons forms a donor lever (E_D) just below the conduction band edge (E_C) and as a consequence the Fermi level (E_F) is shifted towards the conduction band edge.

Heine *et al.* proposed that under catalytic conditions the (dynamic) active monolayer of M1 with its V^{4+}/V^{5+} redox couple, works like a chemical diode conducting electrons from the hydrocarbon to the bulk, preferentially and separating the free charge carriers of the bulk from the active sites.[49] Reason for this is an upward band bending of the electron bands near the surface causing a depletion of electrons in the near-surface region and a reduced electron transfer from the bulk to the active monolayer. This prevents the simultaneous activation of oxygen and caused a low concentration of electrophilic oxygen species.

In case of vanadia supported on insulating mesoporous silica SBA-15, no electrons can be injected from vanadia into the bulk or/and extracted from the bulk into vanadia due to energetic lower located acceptor (LUMO) or/and higher located donor (HOMO) levels of vanadia compared to the conduction and valence band of silica. Consequence of it is that only local acceptor and donor levels of monomeric or oligomeric vanadia species at the surface will mediate the electron transfer.

Carbon materials, like CNTs, are typical semimetals[65], which have no band gap. Electrons can move from the valence band into the conduction band without any input of energy, causing an easy exchange of charge carriers. Figure 1-9 shows a simplified comparative scheme of the electronic properties of the selected catalysts.

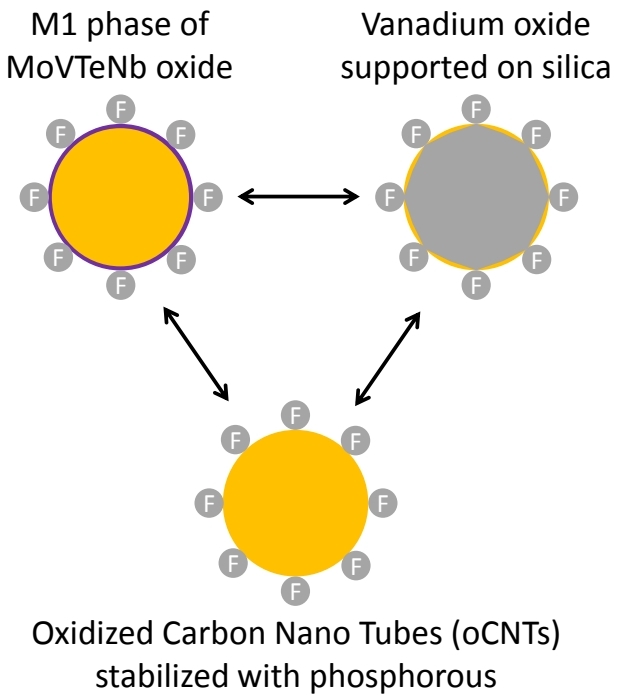

Figure 1-9 Simplified illustration of the selected catalysts with their different electronic properties (yellow = charge carriers; purple = chemical diode; F = functional group).

1.4.6 Comparison of the selected catalysts

All three catalysts are well studied under different reaction conditions in the literature. The n-type semiconducting MoVTeNb-oxide with M1 structure is a potential catalyst for the oxidative dehydrogenation of ethane or propane and the partial oxidation of propane to acrylic acid. A dynamic active monolayer is formed under reaction conditions over M1, which differs from the bulk. Vanadium oxide supported on insulating mesoporous silica SBA-15 is a catalyst with high activity and selectivity for the oxidative dehydrogenation of ethane and propane and only small amounts of oxygenates are observed. Oxidized carbon nanotubes stabilized with phosphorous oxides that have the electronic properties of a semimetal shows high selectivity with moderate activity in the ODH of different substrates. Reported reaction networks for ethane and propane oxidation for the three catalysts show the typical products of oxidative dehydrogenation networks (olefin and carbon oxides). Some of the networks also contain oxygenates, which were observed. All three materials have similar terminal oxo groups at the surface, namely terminal hydroxyl groups, bridging oxygen and terminal oxygen. The vanadium containing catalysts contain additionally surface bridging oxygen and in the case of MoVTeNb-oxide also bulk oxygen. The role of the

different oxygen types in the catalytic cycle is still unclear. Also the influence of the different electronic properties of the three catalysts is not known at the moment.
A direct comparison of the catalytic performance of the three catalysts for ethane and propane oxidation is not possible, due to different applied reaction conditions in the literature so far.

1.5 Motivation and approach of the work

Oxidative dehydrogenation of ethane and propane are an alternative route to ethylene and propylene, which has not the drawbacks of actual endothermic production processes. Difficult control of product selectivity is the main reason why the ODH reaction is not establish as an industrial application. Activation of ethane or propane at the catalysts surface via C-H bond breaking is assumed to be a rate determining step in the overall reaction network. The activated hydrocarbon can be transformed into the olefin or undesired products. Formed ethylene or propylene can be further oxidized to valuable products, like acetaldehyde or acrylic acid, or to the undesired carbon oxides CO and CO_2. Interaction of the hydrocarbons with the catalyst surface is still not clear until now. Several catalysts are reported for the ODH and can be classified in three groups: bulk metal oxides, supported metal oxides, and metal free catalysts. The fact that all published catalysts were investigated under different applied reaction temperatures and feed compositions, prevent a direct comparison of the materials with respect to the reaction network and the catalyst properties.
MoVTeNb oxide with M1 phase, vanadia supported on mesoporous silica SBA-15 and oxidized CNTs impregnated with P_2O_5 are well characterized examples for these catalyst types, which differ in the amount of oxygen species and their electronic properties and are chosen to perform a comparative study. The objective of the study is to find out similarities and differences in the reaction network of ethane and propane oxidation over the three selected model catalysts and if the catalyst performance only depends on active structure elements at the surface or additionally also on the electronic properties of the catalyst. To achieve this, the reaction networks are investigated by catalyst performance measurements, adsorption experiments, temperature programmed reaction measurements and isotope studies.

The outline of the work is given in the following.

Chapter 2 describes the used reactor setups for the study.

Chapter 3 deals with the catalytic performance of MoVTeNb oxide with M1 phase, vanadia supported on mesoporous silica SBA-15 and oxidized CNTs impregnated with P_2O_5 in the oxidative dehydrogenation of ethane and propane under similar reaction conditions and the adsorption of alkanes and alkenes on the used catalyst.

Chapter 4 shows the results of reaction network analysis for propane oxidation on the vanadia based catalysts. Temperature programmed reaction experiments and isotope studies are used for this.

In Chapter 5, all obtained results are summarized and discussed.

1.6 References

[1] R. Grabowski, *Catalysis Reviews* **2006**, *48*, 199–268.

[2] B. Frank, M. Morassutto, R. Schomäcker, R. Schlögl, D. S. Su, *ChemCatChem* **2010**, *2*, 644–648.

[3] E. Heracleous, M. Machli, A. A. Lemonidou, I. A. Vasalos, *Journal of Molecular Catalysis A: Chemical* **2005**, *232*, 29–39.

[4] W. M. Haynes, *Handbook of Chemistry and Physics*, CRC press, 95th Edition 2014–2015.

[5] C. Batiot, B. K. Hodnett, *Applied Catalysis A: General* **1996**, *137*, 179–191.

[6] S. T. Oyama, *The Journal of Physical Chemistry* **1990**, *94*, 5029–5033.

[7] M. M. Bettahar, G. Costentin, L. Savary, J. C. Lavalley, *Applied Catalysis A: General* **1996**, *145*, 1–48.

[8] D. L. Stern, R. K. Grasselli, *Journal of Catalysis* **1997**, *167*, 560–569.

[9] M. Lin, T. B. Desai, F. W. Kaiser, P. D. Klugherz, *Catalysis Today* **2000**, *61*, 223–229.

[10] K. Chen, A. T. Bell, E. Iglesia, *The Journal of Physical Chemistry B* **2000**, *104*, 1292–1299.

[11] F. Cavani, N. Ballarini, A. Cericola, *Catalysis Today* **2007**, *127*, 113.

[12] H. K. G. Ertl, F. Schüth, J. Weitkamp, *Handbook of Heterogeneous Catalysis, Vol. 7*, WILEY-VCH, **2007**.

[13] P. Botella, J. M. López Nieto, B. Solsona, A. Mifsud, F. Márquez *Journal of Catalysis* **2002**, *209*, 445–455.

[14] R. K. Grasselli, J. D. Burrington, D. J. Buttrey, P. DeSanto Jr., C. G. Lugmair, A. F. Volpe Jr., T. Weingand, *Topics in Catalysis* **2003**, *23*, 5–22.

[15] W. Ueda, D. Vitry, T. Katou, *Catalysis Today* **2004**, *96*, 235–240.

[16] A. C. Sanfiz, T. W. Hansen, D. Teschner, P. Schnörch, F. Girgsdies, A. Trunschke, R. Schlögl, M. H. Looi, S. B. A. Hamid, *Journal of Physical Chemistry C* **2010**, *114*, 1912–1921.

[17] P. Botella, E. García-González, A. Dejoz, J. M. López Nieto, M. I. Vázquez, J. González-Calbet, *Journal of Catalysis* **2004**, *225*, 428-438.

[18] T. Katou, D. Vitry, W. Ueda, *Catalysis Today* **2004**, *91–92*, 237–240.

[19] L. Yuan, V. V. Guliants, M. A. Bañares, S. J. Khatib, *Topics in Catalysis* **2008**, *49*, 268–280.

[20] A. Dinse, S. Khennache, B. Frank, C. Hess, R. Herbert, S. Wrabetz, R. Schlögl, R. Schomäcker, *Journal of Molecular Catalysis A: Chemical* **2009**, *307*, 43–50.

[21] P. Grüne, T. Wolfram, K. Pelzer, R. Schlögl, A. Trunschke, *Catalysis Today* **2010**, *157*, 137–142.

[22] J. Zhang, X. Liu, R. Blume, A. Zhang, R. Schlögl, D. S. Su, *Science* **2008**, *322*, 73–77.

[23] B. Frank, J. Zhang, R. Blume, R. Schlögl, D. S. Su, *Angewandte Chemie International Edition* **2009**, *48*, 6913–6917.

[24] M. F. R. Pereira, J. J. M. Orfão, J. L. Figueiredo, *Applied Catalysis A: General* **2000**, *196*, 43–45.

[25] J. Zhang, X. Wang, Q. Su, L. Zhi, A. Thomas, X. Feng, D. S. Su, R. Schlögl, K. Müllen, *Journal of the American Chemical Society* **2009**, *131*, 11296–11297.

[26] J. A. Maciá-Agulló, D. Cazorla-Amorós, A. Linares-Solano, U. Wild, D. S. Su, R. Schlögl, *Catalysis Today* **2005**, *102–103*, 248–253.

[27] J. Zhang, D. S. Su, A. Zhang, D. Wang, R. Schlögl, C. Hébert, *Angewandte Chemie International Edition* **2007**, *46*, 7319–7323.

[28] Y.–R. Luo, *CRC Handbook of Chemistry and Physics*, CRC Press, **2011**, 9–65.

[29] H. H. Kung, *Advances in Catalysis* **1994**, *40*, 1–38.

[30] X. Rozanska, R. Fortrie, J. Sauer, *The Journal of Physical Chemistry C* **2007**, *111*, 6041–6050.

[31] G. Fu, X. Xu, X. Lu, H. Wan, *The Journal of Physical Chemistry B* **2005**, *109*, 6416–6421.

[32] M. Gómez-Gallego and M. A. Sierra, *Chemical Reviews* **2011**, *111*, 4857–4963.

[33] J. Happel, *Isotopic Assessment of Heterogeneous Catalysis*, Academic Press, **1986**.

[34] K. B. Wiberg, *Chemical Reviews* **1955**, *55*, 713–743.

[35] K. Chen, E. Iglesia, A. T. Bell, *The Journal of Physical Chemistry B* **2001**, *105*, 646–653.

[36] X. Rozanska, R. Fortrie, J. Sauer, *Journal of the American Chemical Society* **2014**, *136*, 7751–7761.

[37] A. Govindasamy, K. Muthukumar, J. Yu, Y. Xu,V. V. Guliants, *The Journal of Physical Chemistry C* **2010**, *114*, 4544–4549.

[38] Inorganic Crystal Structure Database, Fachinformationszentrum (FIZ) Karlsruhe, Germany.

[39] M. Lundberg, M. Sundberg, *Ultramicroscopy* **1993**, *52*, 429–435.

[40] K. Oshihara, T. Hisano, W. Ueda, *Topics in Catalysis* **2001**, *15*, 153–160.

[41] R. K. Grasselli, *Catalysis Today* **2005**, *99*, 23–31.

[42] R. K. Grasselli, D. J. Buttrey, J. D. Burrington, A. Andersson, J. Holmberg, W. Ueda, J. Kubo, C. G. Lugmair, A. F. Volpe Jr, *Topics in Catalysis* **2006**, *38*, 7–16.

[43] A. Celaya Sanfiz, T. W. Hansen, A. Sakthivel, A. Trunschke, R. Schlögl, A. Knoester, H. H. Brongersma, M. H. Looi, S. B. A. Hamid, *Journal of Catalysis* **2008**, *258*, 35–43.

[44] V. V. Guliants, R. Bhandari, H. H. Brongersma, A. Knoester, A. M. Gaffney, S. Han, *The Journal of Physical Chemistry B* **2005**, *109*, 10234–10242.

[45] N. R. Shiju, X. Liang, A. W. Weimer, C. Liang, S. Dai, V. V. Guliants, *Journal of the American Chemical Society* **2008**, *130*, 5850–5851.

[46] R. Naumann d'Alnoncourt, L.-I. Csepei, M. Hävecker, F. Girgsdies, M. E. Schuster, R. Schlögl, A. Trunschke, *Journal of Catalysis* **2014**, *311*, 369–385.

[47] M. Hävecker, S. Wrabetz, J. Kröhnert, L.-I. Csepei, R. Naumann d'Alnoncourt, Y. V. Kolen'ko, F. Girgsdies, R. Schlögl, A. Trunschke, *Journal of Catalysis* **2012**, *285*, 48–60.

[48] R. Schlögl, *Topics in Catalysis* **2011**, *54*, 627–638.

[49] C. Heine, M. Hävecker, M. Sanchez-Sanchez, A. Trunschke, R. Schlögl, M. Eichelbaum, *The Journal of Physical Chemistry C* **2013**, *117*, 26988–26997.

[50] X. Li and E. Iglesia, *Chemistry A European Journal* **2007**, *13*, 9324–9330.

[51] V. I. Sobolev, K. Y. Koltunov, *ChemCatChem* **2011**, *3*, 1143–1145.

[52] D. Zhao, J. Feng, Q. Huo, N. Melosh, G. H. Fredrickson, B. F. Chmelka, G. D. Stucky, *Science* **1998**, *279*, 548–552.

[53] D. Zhao, Q. Huo, J. Feng, B. F. Chmelka, G. D. Stucky, *Journal of the American Chemical Society* **1998**, *120*, 6024–6036.

[54] H. Tian, E. I. Ross, I. E. Wachs, *The Journal of Physical Chemistry B* **2006**, *110*, 9593 – 9600

[55] A. Khodakov, B. Olthof, A. T. Bell, E. Iglesia, *Journal of Catalysis* **1999**, *181*, 205–216.

[56] G. Martra, F. Arena, S. Coluccia, F. Frusteri, A. Parmaliana, *Catalysis Today* **2000**, *63*, 197–207.

[57] K. Chen, E. Iglesia, A. T. Bell, *Journal of Catalysis* **2000**, *192*, 197–203.

[58] K. Chen, A. Khodakov, J. Yang, A. T. Bell, E. Iglesia, *Journal of Catalysis* **1999**, *186*, 325–333.

[59] S. Iijima, *Nature* **1991**, *354*, 56–58.

[60] P. J. F. Harris, *Carbon Nanotube Science - Synthesis, Properties, and Applications*, Cambridge University Press, Cambridge, **2009**.

[61] M. F. L. De Volder, S. H. Tawfick, R. H. Baughman, A. J. Hart, *Science* **2013**, *339*, 535–539.

[62] G. Mestl, N. I. Maksimova, N. Keller, V. V. Roddatis, R. Schlögl, *Angewandte Chemie International Edition* **2001**, *40*, 2066–2068.

[63] J. L. Figueiredo, M. F. R. Pereira, M. M. A. Freitas, J. J. M. Órfão, *Carbon* **1999**, *37*, 1379–1389.

[64] D. S. Su , J. Zhang, B. Frank, A. Thomas, X. Wang, J. Paraknowitsch, R. Schlögl, *ChemSusChem* **2010**, *3*, 169–180.

[65] C. Jacoboni, *Theory of Electron Transport in Semiconductors*, Springer Series in Solid-State Sciences 165, **2010**.

Chapter 2 Reactor setups

Appropriate lab-scale reactors are a prerequisite for the development of catalysts and the investigation of reaction mechanisms.[1] Most common reactor setups in use are fixed bed reactors. A parallel reactor setup for kinetic studies and a single tube reactor for temperature programmed, isotope or pulse experiments dedicated to the investigation of individual parts of the reaction mechanism are used to study the intrinsic kinetics of ethane and propane oxidation over the three model catalysts under identical reaction conditions. This investigation is expected to reveal similarities and differences in the reaction mechanisms and networks, respectively, of the three catalysts.

2.1 Parallel reactor setup for formal kinetic measurements

The kinetic measurements were carried out in a commercial parallel reactor setup for partial oxidation "Grimsel 2" (Integrated Lab Solutions, Berlin, Germany). Figure 2-1 shows the flow chart of the parallel reactor setup with the 8 fixed-bed reactors, located in two reactor blocks.

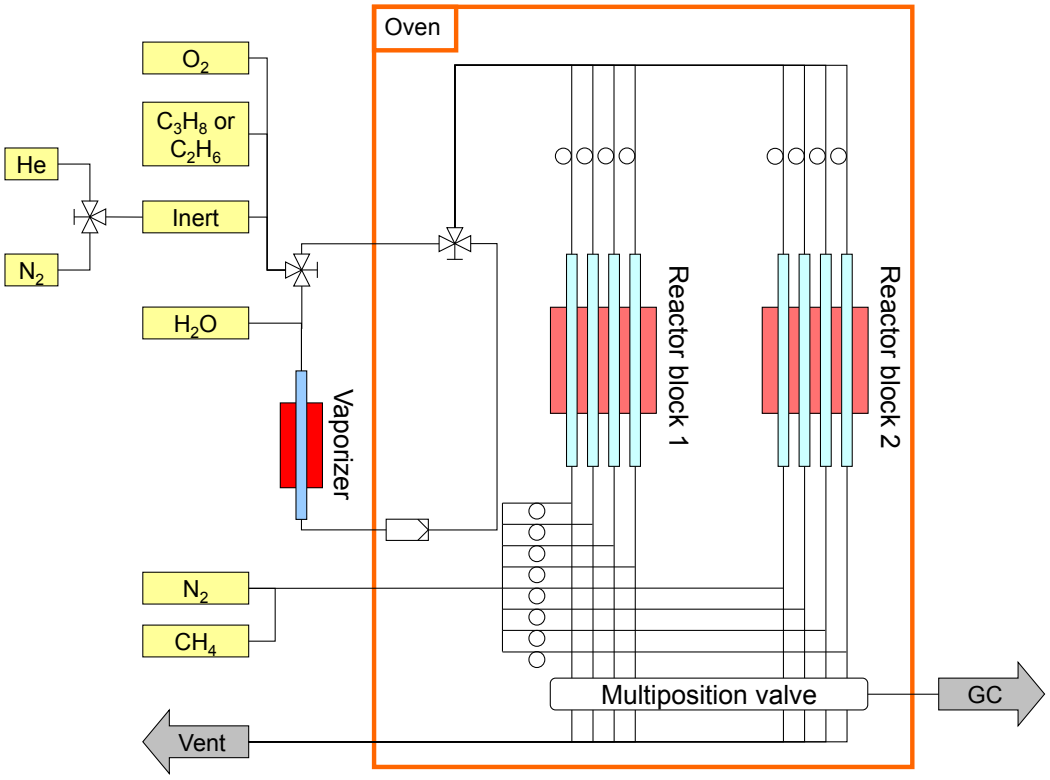

Figure 2-1 Flow chart of parallel reactor setup "Grimsel 2"

The system can be subdivided into three parts: **gas mixing**, **reactors**, and **product analysis**. Feed composition and temperature are the same in all reactors. A variation of contact time can be achieved by using different masses of catalysts. Mass flow controllers for gases and H_2O provide stable flow rates, which are necessary for kinetic measurements. Two 3-way valves are used to switch between dry and wet feed. The wet feed is realized by passing the reactant mixture through a vaporizer, which adds steam to the feed. Eight capillaries are used to evenly distribute the feed gas to the individual reactors. The product gas of each reactor is evenly diluted with a mixture of nitrogen and methane. Methane is used to calculate the real dilution factor of each individual reactor, respectively. A multiposition valve is used to select the gas stream of each reactor in a predetermined sequence. The process control system of the setup is used to run the experiments fully automated.

2.1.1 Gas mixing

A set of mass flow controllers (Bronkhorst) is used to dose the gases and water into the reactor. Propane and ethane respectively as well as oxygen are used as reactants. Helium or nitrogen are used as inert gases in the mixture. H_2O is introduced via a vaporizer to the gas stream. The final gas stream is evenly distributed over 8 capillaries to the reactors. Figure 2-2 shows the flow distribution of the 8 reactors for a flow of 160 ml min^{-1} nitrogen. The relative standard deviation for each reactor is less or equal 0.2 %.

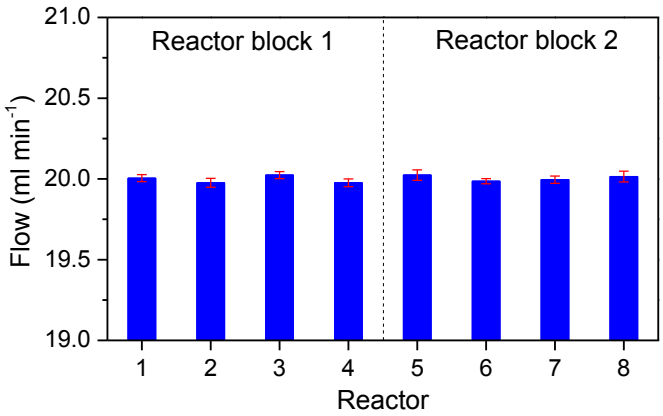

Figure 2-2 Result of flow distribution test.

2.1.2 Reactors

Quartz tubes (Figure 2-3) with an outer diameter of 10 mm, inner diameter of 6 mm, length of 370 mm, and a tapering at 135 mm are used as reactors. All reactors are connected by CAJON Ultra-Torr connectors and sealed with viton o-rings on both sides.

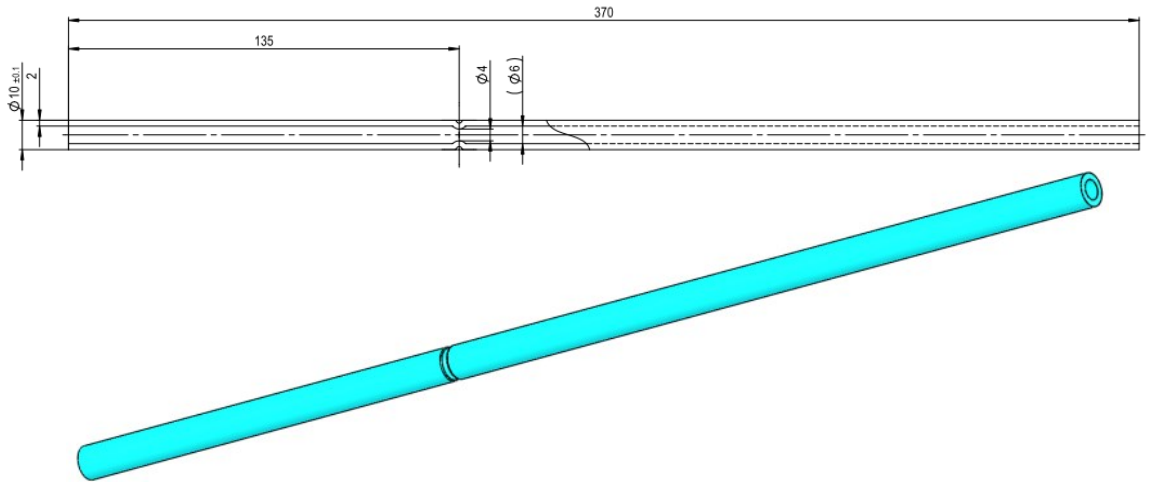

Figure 2-3 Technical drawing of Grimsel 2 quartz reactor.

Two heating blocks are used as reactor furnaces. The temperature in each reactor is monitored by type K thermocouples inside the quartz tube reactors. The isothermal zone of both blocks were determined by measuring the temperature inside a SiO_2 bed (particle size: 250 to 355 µm) at 500 °C as shown in Figure 2-4. The length of the isothermal zone for both ovens is 8 cm and is located in the center of the reactor ovens.

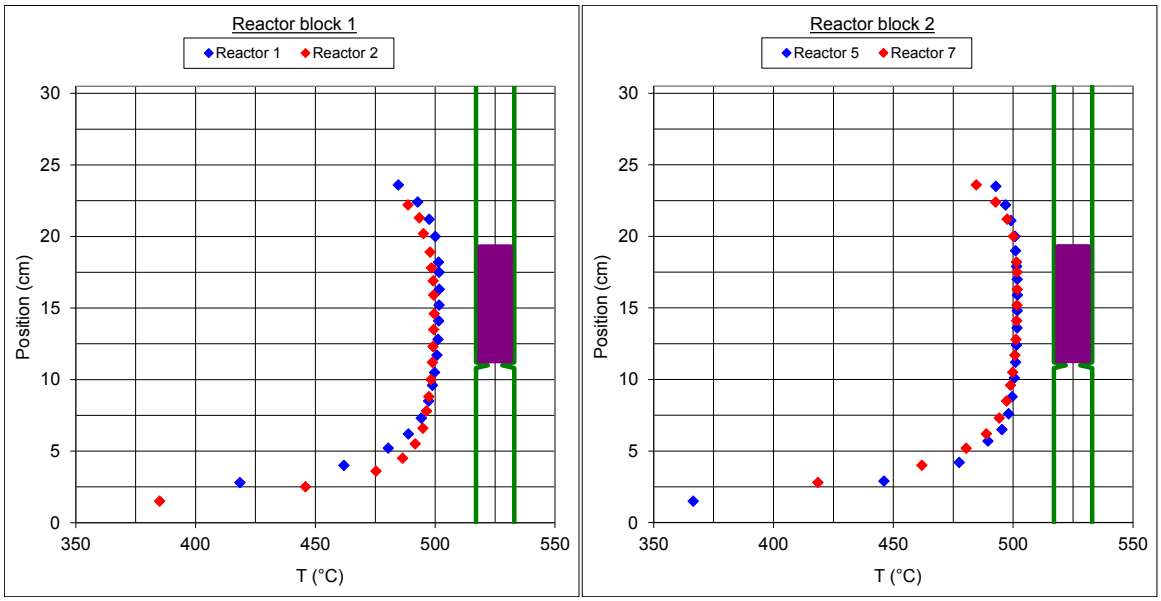

Figure 2-4 Temperature profiles of reactor block 1 and 2.

2.1.3 Gas analysis

The product gas of each individual reactor is selected by a multi position valve from Valco Vici and analysed with a gas chromatograph (Agilent Technologies 7890), equipped with flame ionization detector (FID) and thermal conductivity detector (TCD). A system of Plot-Q and Plot-molsieve columns connected to the TCD separates the permanent gases CO, CO_2, N_2, O_2, and CH_4. A system of FFAP and Plot-Q columns connected to the FID allowed the separation of C_1-C_4 hydrocarbons and oxygenates.

2.1.4 Comparability of the 8 reactors

To clarify, if all 8 reactors are comparable meaning that they show the same performance under the same reaction conditions for the same catalyst, all reactors were filled with a mixture of 0.5 g MoVTeNb oxide with M1 phase (FHI sample ID 10068, particle size 250 to 355 µm) and 2.5 g SiC. Figure 2-5 shows the performance of MoVTeNb #10068 in propane oxidation for the individual reactors with no significant difference regarding carbon balance, propane conversion, and product selectivity, meaning the same reactivity for all reactors.

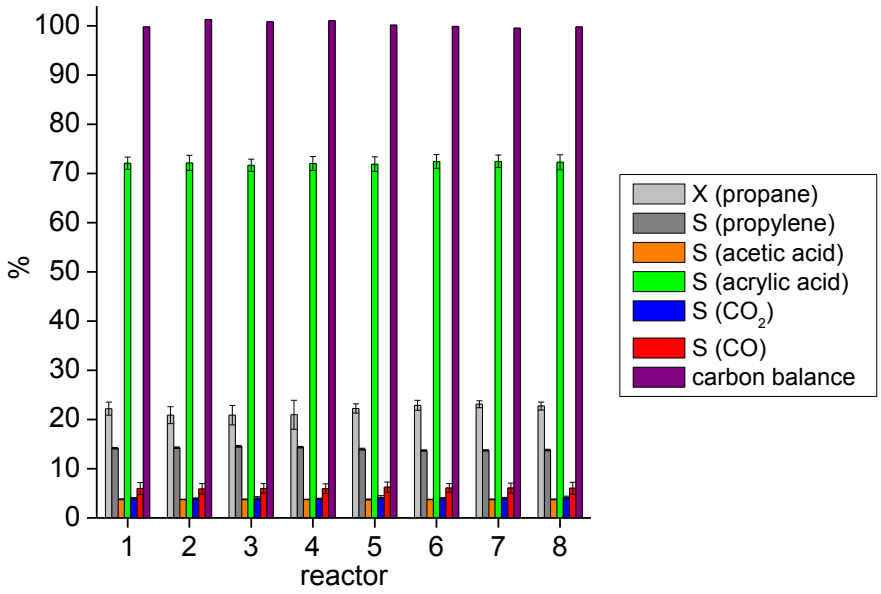

Figure 2-5 Grimsel 2 performance test with MoVTeNb oxide (FHI sample ID 10068) in propane oxidation at 375 °C, W/F per reactor = 2 g s ml^{-1}, and a feed of $C_3H_8/O_2/H_2O/N_2$= 3/6/40/51.

In a second test, the setup was tested in the ODP with the 6V/13Ti/SBA-15 catalyst (FHI internal sample number 10182; 6 wt% V_2O_5 and 13 wt% TiO_2 on SBA-15) to ensure the quality for kinetic measurements. Variation of contact time (based on different sample weight at constant flow with same bed high over all 8 reactors, achieved by silicon carbide dilution) and temperature was performed to determine the performance of the catalyst and the apparent activation energy of propane consumption. Figure 2-6 shows the performance of the 6V/13Ti/SBA-15 catalyst. A high selectivity to propylene is only observed at low conversion. Increasing conversion leads to an increase of CO and CO_2 selectivity with simultaneous decrease of propylene selectivity.

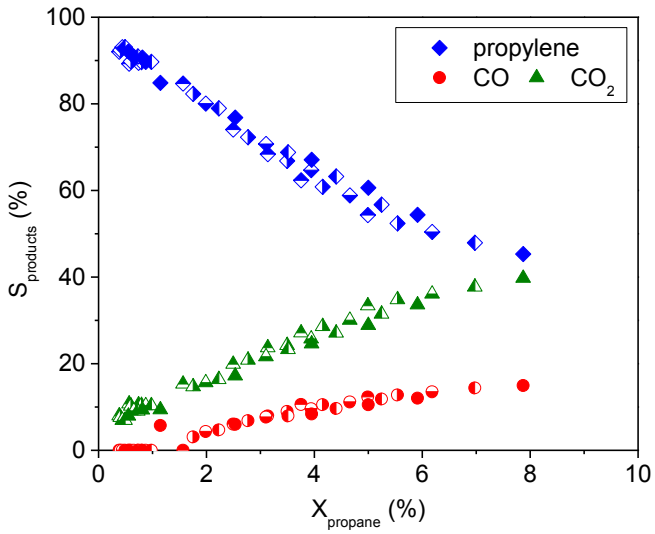

Figure 2-6 Propane conversion vs. product selectivity in ODP over 6V/13Ti/SBA-15 (FHI sample ID 10182) at T = 300 °C (half open down symbol), 305 °C (half open left symbol), 310 °C (half open top symbol), 315 °C (half open right symbol), and 320 °C (full symbol), W/F = 0.0263 to 0.3015 g s ml^{-1}, and Feed $C_3H_8/O_2/N_2$ = 10/5/85.

Averaged apparent activation energy of 63 kJ mol^{-1} with a standard deviation of ± 2 kJ mol^{-1} was obtained for all 8 reactors and shows the equivalence of all 8 reactors.

The results of both tests show that the Grimsel 2 setup can be used for kinetic studies.

2.2 Single tube reactor for pulse experiments

Microkinetic investigations of the ODP reaction are carried out in a self-constructed reactor setup, which can be operated in different modes for different issues: pulse experiments, temperature programmed reaction (TPR), catalysts performance tests, and steady state isotopic transient kinetic analysis (SSITKA). The flow chart of the setup is shown in Figure 2-7.

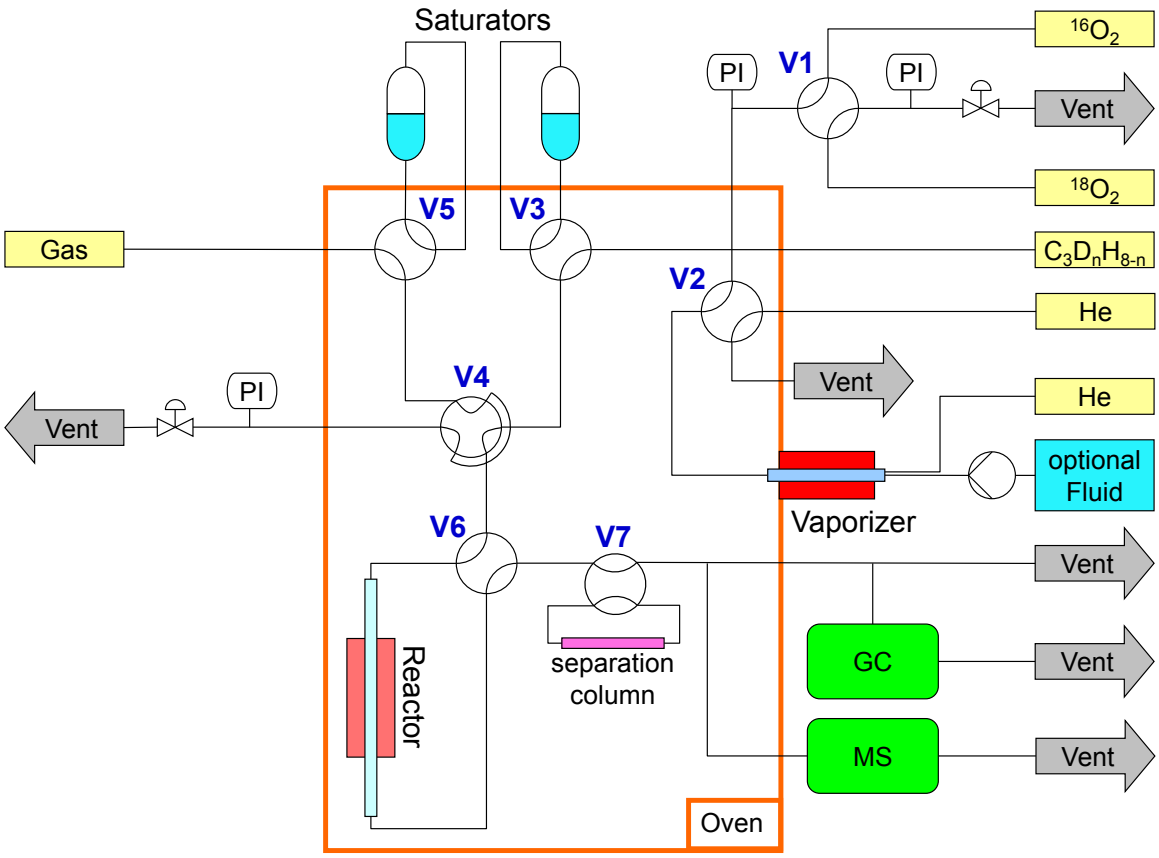

Figure 2-7 Flowchart of single tube reactor for pulse experiments.

The setup can be subdivided into 4 parts: **gas mixing**, **reactor**, **separation section for pulse experiments**, and **gas analysis**. Flow rate, feed composition, temperature, and composition of the catalyst bed can be independently adjusted. Mass flow controllers for gases, a vaporizer for liquids, and two saturators provide stable flow rates. Valve **V2** after the vaporizer is used to switch between dry and saturated feed. Valve **V1** can be used to switch between two isotopes of a certain molecule during steady state of the reaction. Two saturators can be turned on- and offline via valves **V3** and **V5**. Pulses of gases or gas mixtures can be sent to the reactor with valve **V4**, which is equipped with a 1 ml sample loop. Chromatographic separation of the gas pulses into individual product and reactant components is achieved by switching the separation column online via valve **V7**. The analysis of products is done with a gas chromatograph and a mass spectrometer. Various methods on both instruments are available for different analytical tasks.

2.2.1 Gas mixing of single tube reactor setup

The gas mixing section can be subdivided into a part for gaseous and for liquid compounds. Gases are fed via mass flow controllers (Bronkhorst) and liquids are introduced in the feed by use of a vaporizer or two saturators. Propane and oxygen are used as reactants and helium as an inert gas in the feed. The stability of the propane mass flow controller was checked at a flow rate of 20 ml min^{-1} with a mixture of 10 vol-% propane in helium versus pure helium. Figure 2-8 shows the response and stability of the propane signal (m/z 44 normalized to m/z 4 of helium) measured with a mass spectrometer. Helium is used as standard to filter out pressure fluctuations inside the mass spectrometer. The step at 2750 s is the switch from pure helium to the propane mixture. The test revealed no fluctuation of the propane mass flow controller over a time of about 2000 s.

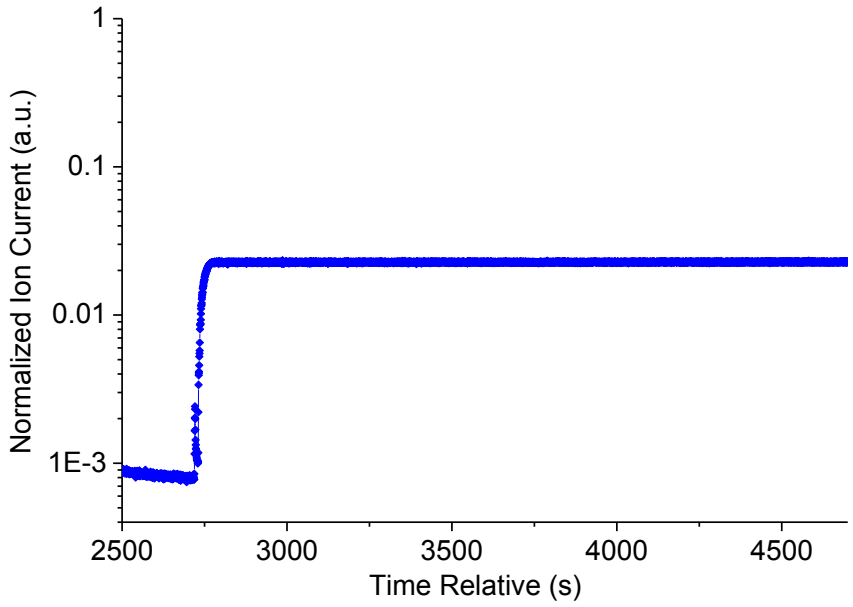

Figure 2-8 Time on stream stability of propane mass flow controller (m/z 44 normalized to m/z 4 of helium).

Liquids that are used in this work are different isotopes of water, which were introduced to the feed via the vaporizer. The check of flow stability of the vaporizer was performed at a flow rate of 20 ml/min with a mixture of 40 vol-% steam in helium versus helium. Figure 2-9 shows the time on stream behaviour of water (m/z 18 normalized to m/z 4 of

helium). The obtained stable signal of water after switch from dry to wet feed at 550 s shows the uniform vaporization of water.

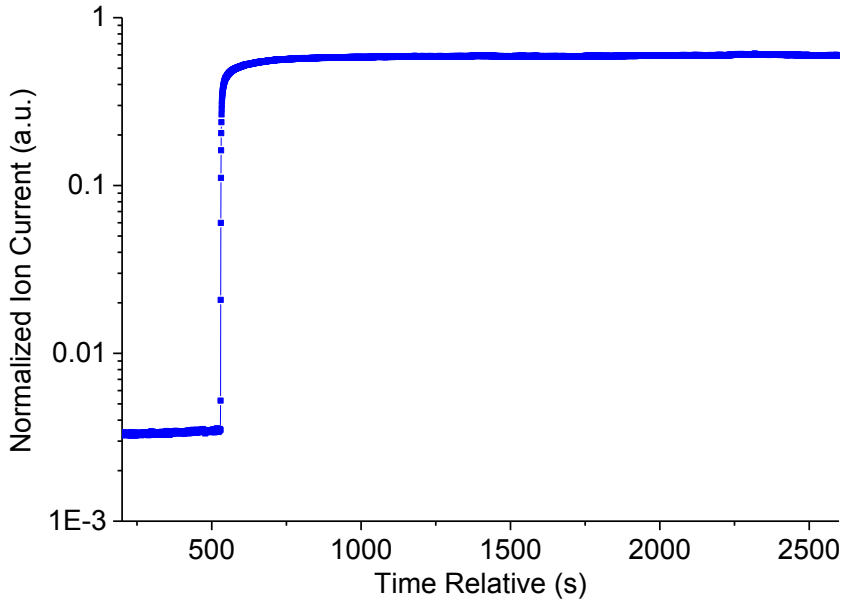

Figure 2-9 Time on stream stability of steam (m/z 18 normalized to m/z 4 of helium).

2.2.2 Reactor of single tube reactor setup

The reactor (Figure 2-10) consists of a glass lined tubing (GLT™ from SGE Analytical Science) with the dimension of 1/4" outer diameter, 4 mm internal diameter and 300 mm length. Both reactor ends were welded to VCR connectors. A surrounding copper block (19 mm outer diameter and 150 mm length), covered with a steel tubing (20 mm outer diameter and 170 length) and Thermon heat transfer compound (cement), improves the isothermal zone of the reactor oven.

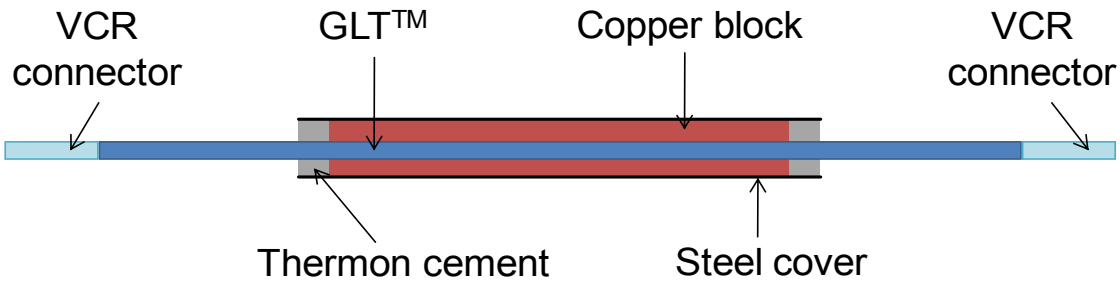

Figure 2-10 Technical drawing of GLT reactor.

The temperature inside the reactor is monitored by a type K thermocouple. A commercial furnace from HTM Reetz (LK 900-35-200-1) is used as reactor oven. The isothermal zone was determined by measuring the temperature inside a SiO_2 bed (particle size: 250 to 355 µm) at 400 °C with 10 ml min^{-1} helium flow and is shown in Figure 2-11. The length of the isothermal zone is 13 cm and it is located in the center of the reactor.

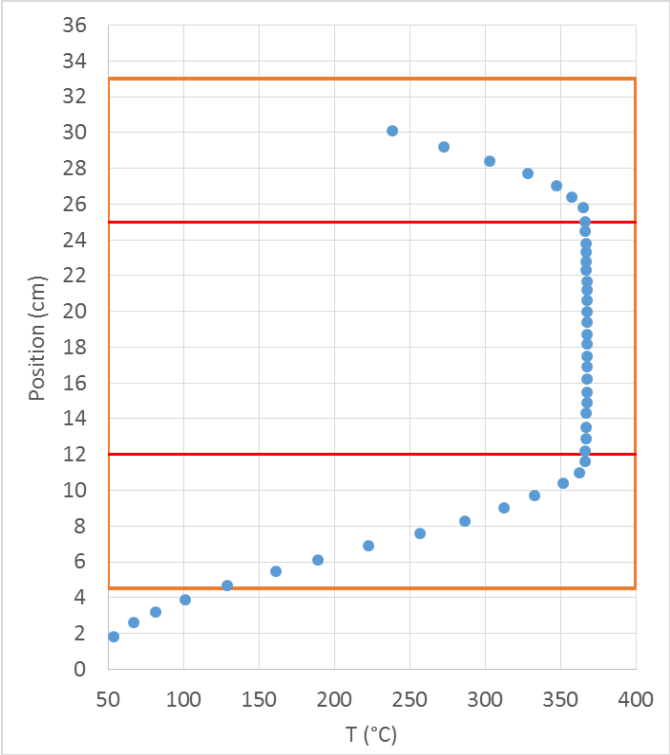

Figure 2-11 Temperature profile of GLT reactor.

2.2.3 Separation section for pulse experiments

The core part of the separation section for pulse experiments is a self-packed column for the separation of reactant and product mixtures into individual compounds that allows unambiguous assignment by mass spectrometry. The column can be switched online or offline via valve **V7** (Figure 2-7). Figure 2-12 illustrates the functional principle, using the example of an installed Porapak Q column for the separation of O_2, CO, and CO_2 from C_3 hydrocarbons. The gas pulse leaving the reactor, which contains reactants and products, runs through the Porapak Q column separating O_2, CO, and CO_2 from C_3 hydrocarbons.

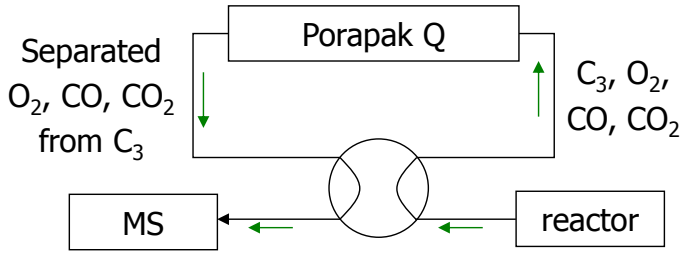

Figure 2-12 Functional principle of the separation section for a Porapak Q column.

Figure 2-13 shows a photograph of the separation section with installed Porapak Q column, valve **V7** and the connection point of the mass spectrometer. The valve position in the photograph indicates that the Porapak Q column is switched online. Within this work, two self-packed columns were used namely Porapak Q and Carbopack. They are described in the following.

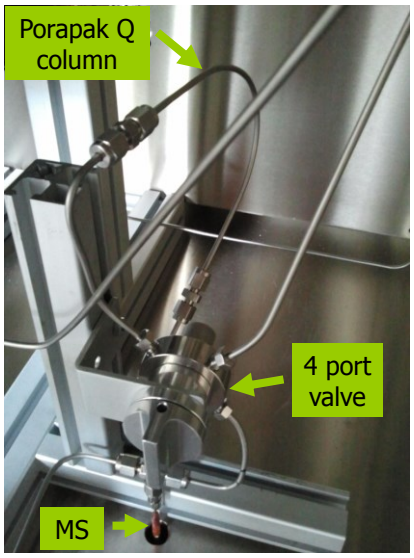

Figure 2-13 Photograph of separation section with installed Porapak Q column.

2.2.3.1 Porapak Q separation column for C_3 hydrocarbons, CO_2, and CO

The self-packed column consists of a 20 cm long 1/8" stainless steel tube with 2 mm internal diameter filled with Porapak Q material from Supelco providing a particle size of 125 to 150 µm. The separation of C_3 hydrocarbons, CO, and CO_2 was checked with two gas mixtures under equal conditions. A sketch of the experiment is shown in Figure 2-14. A defined volume of 1 ml gas mixture is injected into the helium flow (10 ml min^{-1}) by

valve **V4** at 50 °C column temperature, and runs through the Porapak Q column for separation.

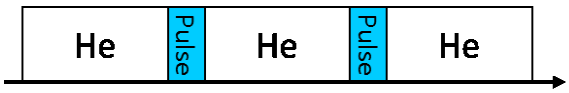

Figure 2-14 Sketch of the pulse experiment.

Both gas mixtures consist of 10 ml min^{-1} test gas combined with 0.5 ml min^{-1} neon, which is used as pulse marker because it will not be retarded. The two test gases are mixtures of 1 vol-% C_3 hydrocarbons (propane or propylene) in nitrogen and 1 vol-% carbon oxides (CO or CO_2) in helium. Figure 2-15 and Figure 2-16 show the resulting chromatograms of both gas mixtures, measured by mass spectrometry. The propane propylene chromatogram (Figure 2-15) has a peak at 790 to 800 s in the m/z 29 trace that comes from the $^{14}N^{15}N$ molecule of the dilution gas.

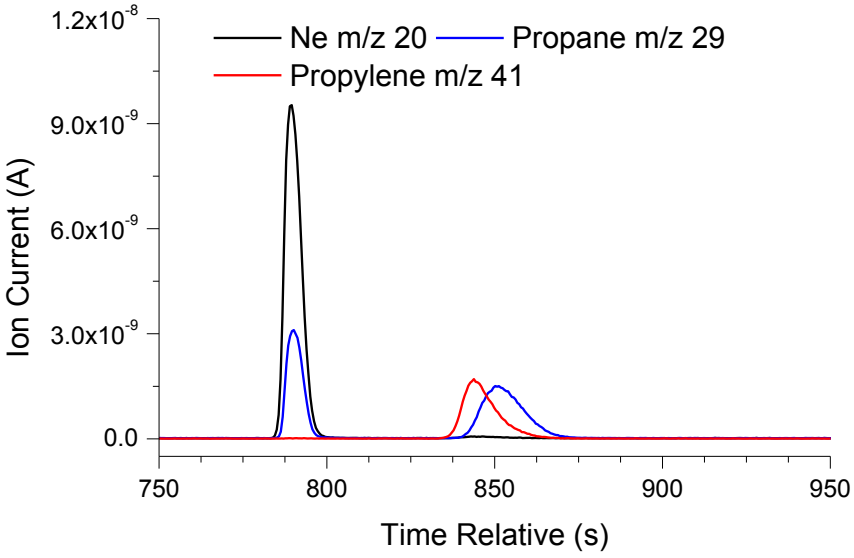

Figure 2-15 Resulting chromatogram of gas mixture 1 composed of 1% C_3H_8, 1% C_3H_6, and 5% Ne in N_2.

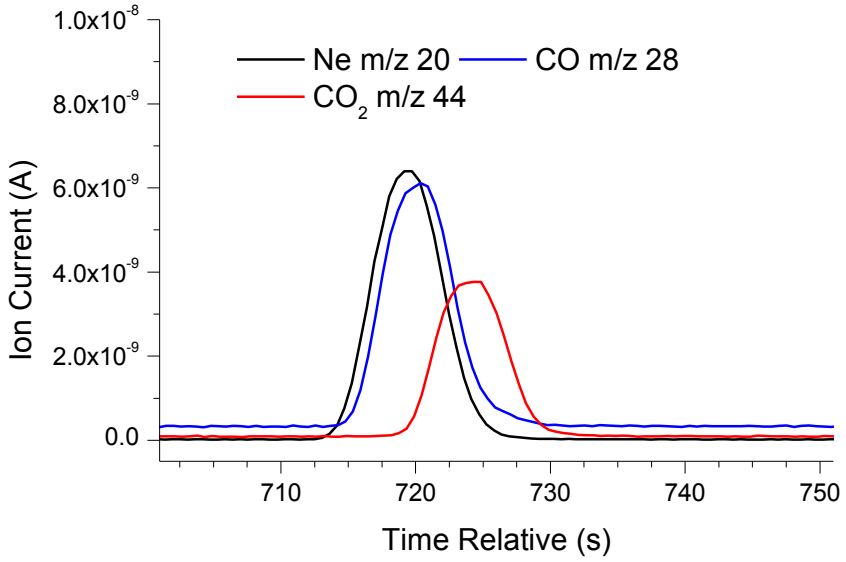

Figure 2-16 Resulting chromatogram of gas mixture 2 composed of 1% CO, 1% CO_2, and 5% Ne in He.

Retention times relative to neon are determined from both chromatograms and are summarized in Table 2-1. The obtained values show that carbon oxides are separated from C_3 hydrocarbons by use of the Porapak Q column.

Table 2-1 Retention times relative to neon of C_3-hydrocarbons and carbon oxides for a self-packed Porapak Q column at 10 ml/min Helium and 50 °C column temperature.

Compound	Retention time (s)
CO	2
CO_2	6
Propylene	50
Propane	60

2.2.3.2 Carbopack separation column for acetic and acrylic acid

The self-packed Carbopack column consists of a 20 cm long 1/8" stainless steel tube with 2 mm internal diameter filled with Carbopack B DA material from Supelco that has a particle size of 125 to 177 µm. Separation of acetic and acrylic acid was checked with a reaction mixture containing the products (propylene, CO, CO_2, acetic acid, and acrylic

acid) and reactants (propane and oxygen). The experiment was performed in a way that 1 ml of reactant mixture (20 vol-% propane, 5 vol-% oxygen, and helium in balance) was injected into the helium flow (see Figure 2-14) via valve **V4** (Figure 2-7). The reactant mixture pulse runs through the reactor that is filled with a M1 catalyst set to 400 °C. The reactants are partially converted into products by the catalyst. The formed reaction mixture runs then through the Carbopack column and the organic acids are separated from all other compounds at a column temperature of 100 °C. Identification of the acids is based on the molecular ion (acetic acid m/z 60 and acrylic acid m/z 72) and typical fragments (acetic acid: CO_2H^+ m/z 45 and acrylic acid: CH_2CHCO^+ m/z 55). Figure 2-17 shows the resulting chromatogram for propane, acetic acid, and acrylic acid, measured with the mass spectrometer.

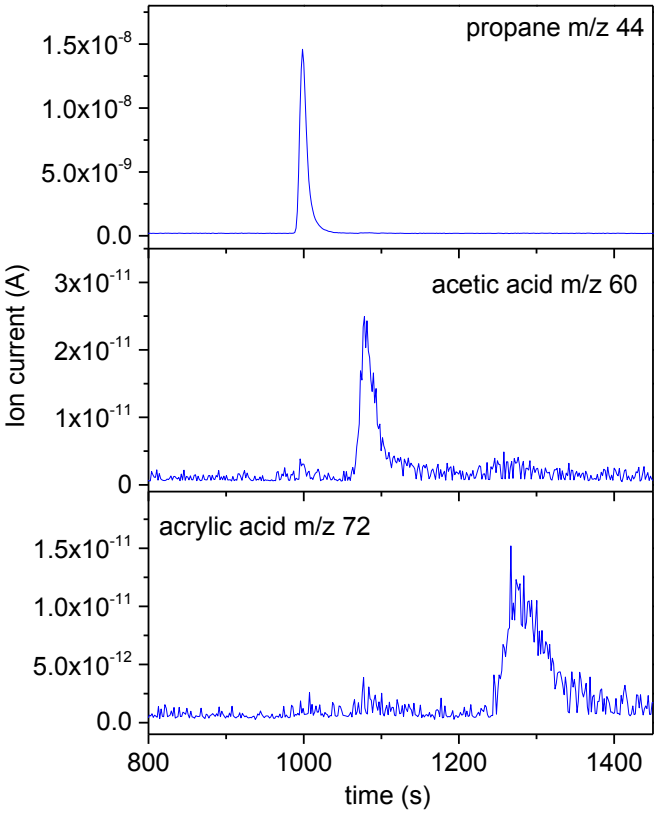

Figure 2-17 Resulting chromatogram of reaction mixture (including reactant propane and products acetic and acrylic acid).

Retention times relative to propane are 75 s for acetic acid and 275 s for acrylic acid and reveal the suitability of the Carbopack column for the separation and acetic and acrylic acid from hydrocarbons.

2.2.4 Gas analysis of single tube reactor setup

A gas chromatograph (Agilent Technologies 7890) equipped with FID and TCD as well as a mass spectrometer (Pfeiffer Vacuum QMA 400) were used for the analysis of products and reactants. For the GC, the same configuration was chosen as described under 2.1.3. The mass spectrometer is equipped with a cross-beam ion source, a faraday cup, and a secondary electron multiplier (SEM). Use of the SEM instead of the faraday cup is the preferred mode of operation during catalytic measurements, due to the lower detection limit of the SEM.

2.2.5 SSITKA mode

Happel,[2] Bennett,[3] and Biloen[4] developed the steady state isotopic transient kinetic analysis (SSITKA) for studying surface reactions. The technique involves the use of two different isotopes of the same reactant and detection of the labeled product species. Features like surface coverage, surface residence time, site heterogeneity, activity distributions, concentration of adsorbed reaction intermediates, and identification of possible mechanisms can be derived from the measurements.[5] The SSITKA mode is realized by the 4-way valve **V1**, which can switch between two different gas lines. The QMA 400 mass spectrometer is used for measuring the transient changes in the isotopic composition due to its high time resolution, mass resolution, and sensitivity. One basic requirement for SSITKA measurements is that both gas lines have equal flow rates and pressures, respectively. Is this not ensured, a disturbance of the steady state occurs in form of typical changes during the isotopic exchange. The SSITKA mode was checked at a total flow rate of 15 ml/min with 1.5 ml/min oxygen versus 1.5 ml/min argon balanced with helium. Figure S 2-1 and Figure S 2-2 are examples where the basic requirements are unfulfilled.

Disaccording flow rates and pressures in Figure S 2-1 are indicated by a plateau change and small peaks in the ion trace just before the decrease of the compound as part of the

exchange. Alignment to equal flow rates for the two mixtures is shown in Figure S 2-2, where only peaks are observed as a result of not matched pressures.

Undisturbed ion traces in Figure 2-18 are the result of adjusted flow rates and pressures for both gases. The test reveals that the basic requirements are fulfilled and the setup can be used for SSITKA measurements.

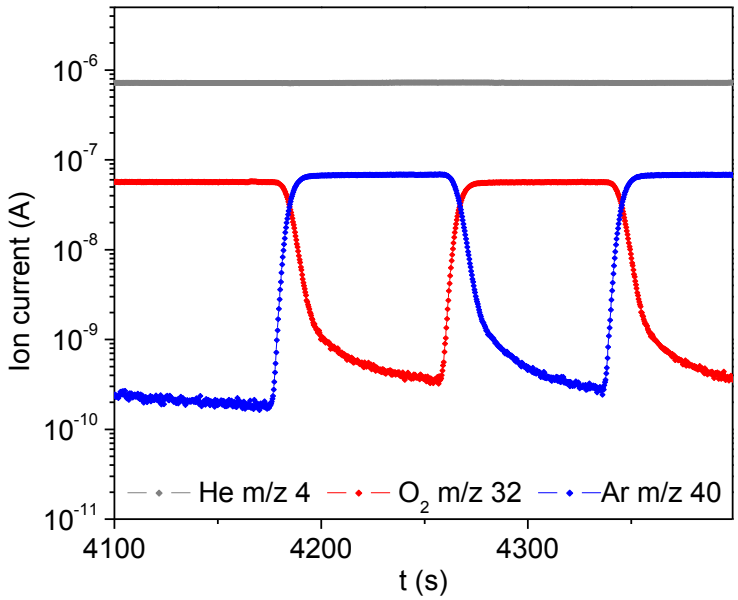

Figure 2-18 Switch between oxygen and argon with aligned flow rates and pressures.

2.3 Mass transport limitations

Catalytic results, which are limited by internal or external mass transport, cannot be used to obtain intrinsic properties of a catalyst. Avoiding these mass transport limitations is necessary to ensure that intrinsic properties can be obtained. The right choice of catalyst particle size relative to the reactor inner diameter is very important for this. A good ratio of particle sizes to inner diameter is 1:10, but must be checked for every experimental parameter set. Checking for mass transport limitations can be done experimentally or by calculating the Mears (pore diffusion) and Weisz-Prater (film diffusion) modulus.[6]

There are two typical experiments to check for mass transport limitations. Variation of the particle size at constant catalyst mass and measuring the reaction rate is used to check for internal mass transport limitations. If the catalyst particle would be too large, the reaction rate becomes limited in pore diffusion and would be smaller than the real rate.

Variation of catalyst mass and keeping the contact time constant by adjusting the total flow is used to check for external mass transport limitations. Measured reaction rates from this variation must be equal, or they are limited by film diffusion.
Another way to check for mass transport limitations is the calculation of the Mears and Weisz-Prater modulus by Equation 2-1 and Equation 2-2.

$$\frac{R_o(r_{eff})_S}{D_i c_i^{ein}} < \frac{0.05}{n}$$

Equation 2-1 Formula for calculation of the Mears modulus where c_i^{ein} is the concentration of component i in the initial feed (mol m^{-3}), D_i is the molecular diffusion coefficient of component i (m^2 s^{-1}), R_o is the internal pipe radius (m), and $(r_{eff})_S$ is the effective reaction rate based on the surface of the catalyst (mol m^2 s^{-1}).

$$\frac{\delta_K^2(r_{eff})_V}{D_e c_i^{ein}} < \begin{cases} 0.7; n = 0 \\ 0.07; n = 1 \\ 0.03; n = 3 \end{cases}$$

Equation 2-2 Formula for calculation of the Weisz-Prater modulus where c_i^{ein} is the concentration of component i in the initial feed (mol m^{-3}), D_e is the effective diffusion coefficient (m^2 s^{-1}), δ_K is the thickness of the catalyst layer (m), and $(r_{eff})_V$ is the effective reaction rate based on the volume of the catalyst (mol m^{-3} s^{-1}).

The Mears modulus can be used to estimate from measured effective reaction rates, whether a limitation by external mass transport exist or not and requires that the effective reaction rate differs not more than 5 % from the one without limitation. For Mears modulus smaller than 0.05/n it can be assumed that no internal mass transport limitation exist.
The Weisz-Prater modulus can be used to calculate from measured effective reaction rates, if an irreversible reaction of the order n is or is not limited by internal mass transportation. Weisz-Prater modulus below 0.07 for a reaction with order 1 indicates no external mass transport limitations.

2.4 Supporting Information

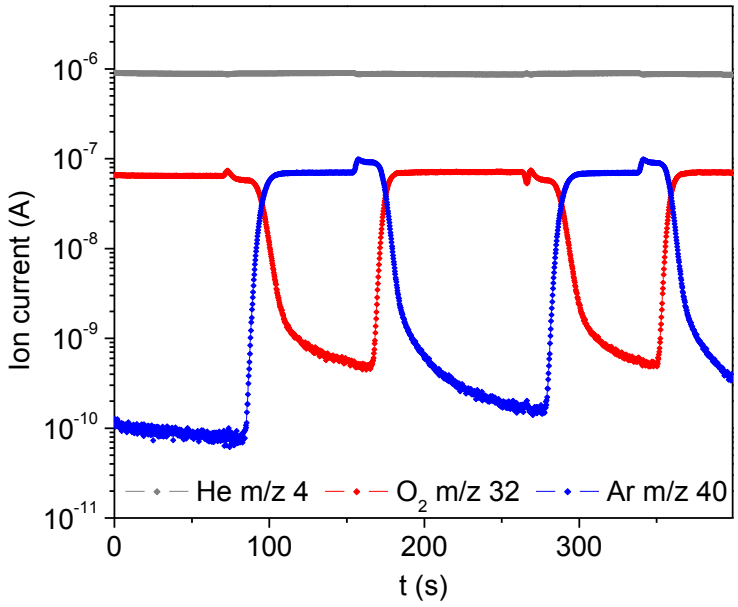

Figure S 2-1 Switch between oxygen and argon with disaccording flow rates and pressures.

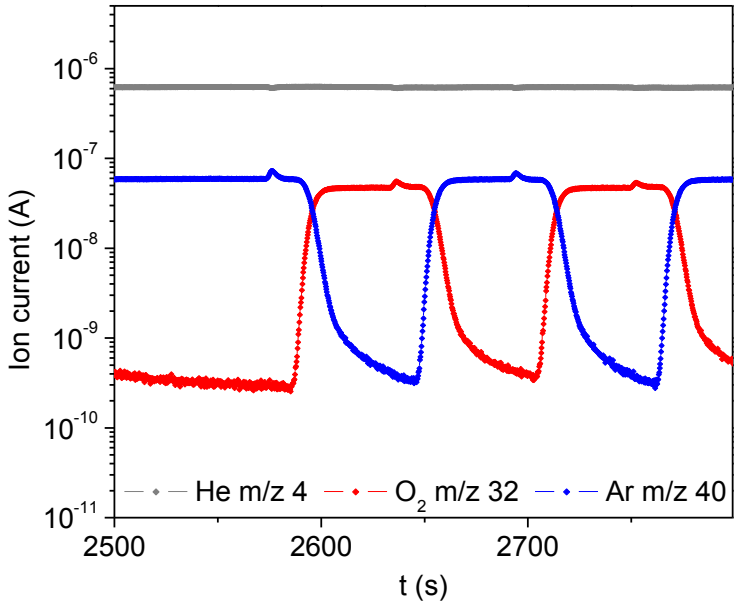

Figure S 2-2 Switch between oxygen and argon with harmonized flow rates and disaccording pressures.

2.5 References

[1] J. Pérez-Ramírez, R. J. Berger, G. Mul, F. Kapteijn, J. A. Moulijn, *Catalysis Today* **2000**, *60*, 93–109.

[2] J. Happel, *Chemical Engineering Science* **1978**, *33*, 1567.

[3] C. O. Bennett, *ACS Symposium Series*, American Chemical Society, Washington, DC, **1982**, *178*, 1.

[4] P. Biloen, *Journal of Molecular Catalysis* **1983**, *21*, 17–24.

[5] V. Frøseth, S. Storsæter, Ø. Borg, E. A. Blekkan, M. Rønning, A. Holmen, *Applied Catalysis A: General* **2005**, *289*, 10–15.

[6] E. Klemm, *Technische Chemie – Einführung in die Chemische Reaktionstechnik*, 5. Auflage, Springer-Verlag, **2005**.

Chapter 3 Functional Analysis of Catalysts for lower Alkane Oxidation[§]

Abstract

The catalytic performance of (i) crystalline MoVTeNb oxide that exhibits the electronic properties of a n-type semiconductor, (ii) sub-monolayer vanadium oxide supported on meso-structured silica (SBA-15) as an insulating support, and (iii) surface-functionalized carbon nanotubes that contain neither a redox active metal nor bulk oxygen, but only surface oxygen species have been compared in the oxidative dehydrogenation of ethane and propane under equal reaction conditions. The catalytic results indicate similarities in the reaction network over all three catalysts within the range of the studied reaction conditions implying that differences in selectivity are a consequence of differences in the rate constants. Higher activity and selectivity to acrylic acid over MoVTeNb oxide as compared to the other two catalysts are attributed to the higher density of potential alkane adsorption sites on M1 and the specific electronic structure of the semiconducting bulk catalyst. Microcalorimetry has been used to determine and quantify different adsorption sites revealing a low $V_{surface}/C_3H_{8ads}$ ratio of 4 on M1 and a much higher ratio of 150 on silica-supported vanadium oxide. On the latter catalyst less than one per cent of the vanadium atoms adsorb propane. Barriers of propane activation increase in the order P/oCNT (139 kJ mol^{-1}) ≤ M1 (143 kJ mol^{-1}) < 6V/SBA-15 (162 kJ mol^{-1}), which is in agreement with trends predicted by theory.

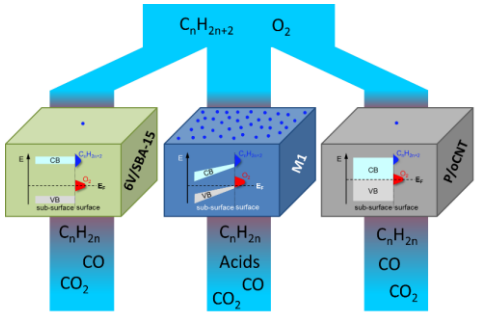

[§]Reproduced from the publication

P. Kube, B. Frank, S. Wrabetz, J. Kröhnert, M. Hävecker, J. Velasco-Vélez, J. Noack, R. Schlögl, A. Trunschke „Functional Analysis of Catalysts for Lower Alkane Oxidation" *ChemCatChem* **2017**, *9*, 573-585, https://doi.org/10.1002/cctc.201601194, with permission from John Wiley and Sons.

Acknowledgement

We thank Dr. M. Sanchez-Sanchez and Dr. T. Wolfram for the synthesis of the catalysts, Dr. F. Girgsdies and E. Kitzelmann for XRD experiments, M. Hashagen and G. Lorenz for BET measurements, G. Weinberg for SEM measurements, Dr. O. Timpe for chemical analysis, and Dr. C. Heine and Dr. R. Naumann d'Alnoncourt for the experimental assistance.

3.1 Introduction

Oxidative dehydrogenation (ODH) is an interesting alternative to current endothermic processes, like steam cracking, fluid catalytic cracking (FCC), or catalytic dehydrogenation (DH), for the manufacture of olefins from light alkanes.[1]However, avoiding total combustion of the alkane to carbon oxides remains the major challenge that impedes application.[2] Vanadium oxide has been regarded as promising catalyst component either in bulk mixed oxides or in the form of highly dispersed monolayers at the surface of supports.[3]

Complex mixed MoV-based oxides composed of the bronze-like structure M1 (ICSD no. 55097)[4] have been reported to show high activity in the oxidation of propaneand ethane.[5] Depending on feed composition and reaction conditions the catalyst primarily produces either olefins or oxygenates.5[b] Under reaction conditions the surface of M1 is enriched in Te^{4+} and V^{5+} forming a thin self-supported active layer.[5b,6]

In contrast, vanadium oxide monolayer catalysts are active in oxidative dehydrogenation, but valuable oxygenates are formed at most in traces irrespective of the reaction conditions. Supported vanadium oxide species V_xO_y exist in different degree of oligomerization including monomeric species without V-O-V bonds and oligomers with different chain length.[3e] The effect of cluster size on reactivity is still unclear.[3g,7]

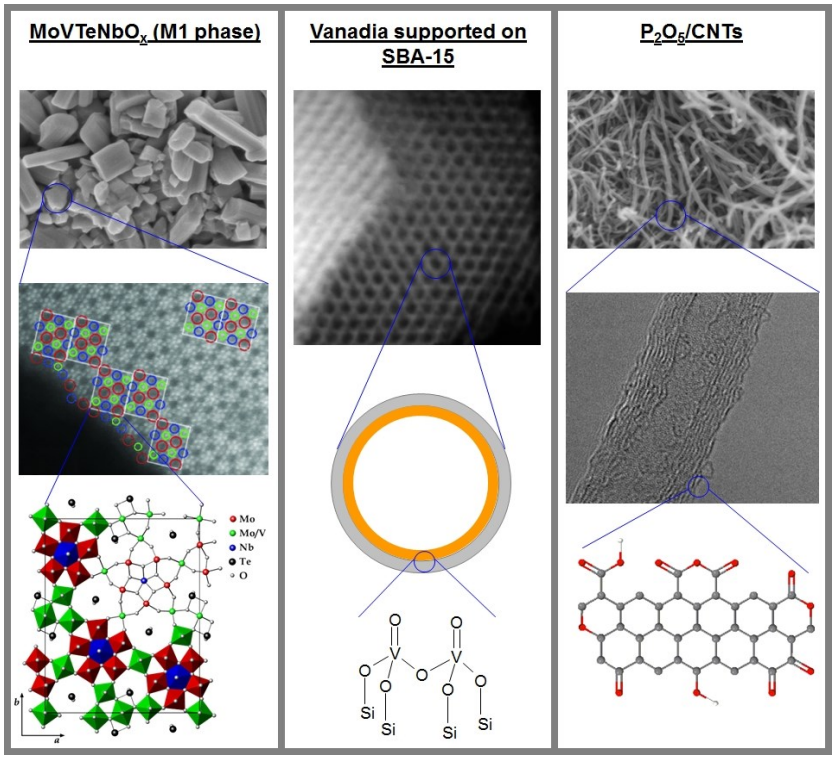

Scheme 3-1 Simplified illustration of potential surface features of vanadium-containing bulk and monolayer catalysts on the one hand and metal-free nanostructured carbon catalysts on the other hand.

Another class of catalysts is based on elemental carbon, like carbon nanotubes (CNT).[8] Edges and defects at the carbon surface are decorated with a variety of oxygen-containing functional groups, which are structurally similar to the functional groups on vanadia catalysts (e.g., V-OH/C-OH, V=O/C=O, V-O-V/C-O-C).[8b] These oxygen functionalities, in particular the redox couple of quinone and hydroquinone species, are regarded as active sites in the ODH reaction.[8b] A simplified illustration of potential surface features of the three catalyst types is presented in Scheme 3-1.

Catalytic properties of these catalysts in oxidation of ethane and propane are not directly comparable due to very different reaction temperatures, contact times, and feed compositions applied so far (Table 3-1). In our work we compare bulk MoVTeNb M1 oxide with vanadium oxide supported on mesoporous silica SBA-15 and vanadium-free carbon nanotube catalysts stabilized by phosphorous oxide (referred to as M1, 6V/SBA-15, and P/oCNT, respectively) in the oxidative dehydrogenation of propane and ethane in the same temperature and feed range. The objective is to identify differences and similarities in reaction network and apparent rate parameters in order to ascertain if

vanadium oxide supported on an apparently inert support, such as silica, and V-free carbon catalysts may serve as models for V-containing bulk catalysts in oxidative dehydrogenation reactions of alkanes.

Table 3-1 Reaction conditions and catalytic properties reported in the literature for the three types of catalysts in oxidative dehydrogenation of ethane and propane.

	T [°C]	Feed [alkane/O_2/inert]	τ [g s ml^{-1}]	r_{alkane} [mmol g^{-1} h^{-1}]	S_{alkene} [%]	$S_{oxygenates}$ [%]	Ref.
Oxidative dehydrogenation of ethane							
M1							
$MoVTeNbO_x$[a]	380	30/20/50	1.8	14.2	~90	~10	9
VO_x/SiO_2							
6.7 wt% V/Aerosil	480	7.3/0.93/91.77	0.12	0.39	~100		10
7.1 wt% V/MCM-41	600	4/8/88	0.51	45.3	60.2	39.8	11
P/oCNT							
	400	20/10/70	0.33	0.24	~66.4	~33.6	12
Oxidative dehydrogenation of propane							
M1							
$MoVTeNbO_x$	380	8/10/37/45[b]	1.5	107	8.7	91.3	3i
$MoVTeNbO_x$	380	3/6/91	0.06	1.7	89	11	13
VO_x/SiO_2							
4.5 wt% V/SBA-15	600	1/1/4	2.15[c]	75[d]	52	48	14
2.7 wt% V/SBA-15	500	16.9/16.9/67.5	0.125	21.6	~50	~50	15
2.8 wt% V/MCM-41	500	30/20/50	0.04	412	42.3	41.4	16
7.1 wt% V/MCM-41	550	4/8/88	0.8	33	45.5	54.5	11
0.5 wt% V/MCM-48	550	4/8/88	11.2	1.13	65.3	34.7	17
0.5 wt% V/Aerosil	550	4/8/88	9.6	1.73	60.2	39.8	17
P/oCNT							
	400	1/1/4	3	0.32	55	45	18

[a] as synthesized catalyst without high-temperature treatment; [b] alkane/O_2/inert/H_2O; [c] τ in[s]; [d] r_{alkane} [mmol ml^{-1}_{cat} h^{-1}]

3.2 Results

3.2.1 Structure and chemical properties of the catalysts

High crystallinity and phase-purity of the studied bulk MoVTeNb M1 oxide catalyst (M1 structure: ICSD No. 55097) have been confirmed by electron microscopy (Figure S 3-1)

and X-ray diffraction (Figure S 3-2). Structural parameters of the applied M1 catalyst are summarized in the Experimental Section. The material is composed of dense, rod-like particles (Figure S 3-1) yielding a polycrystalline, macroporous solid that is characterized by a comparatively low specific surface area (Table 3-2, Table S 3-1, Figure S 3-3). The macropores are formed by voids enclosed within aggregates and agglomerates of the primary catalyst particles. The total vanadium content of M1 is only slightly higher compared to 6V/SBA-15 (Table 3-2).The M1 surface concentration of V corresponds to 1.7 V atoms nm^{-2} (Table 3-2), calculated based on XPS measurements (Figure S 3-4).

6V/SBA-15 features a sub-monolayer of two-dimensional vanadium oxide species on the surface of mesoporous silica SBA-15 as support. The regular pore structure of SBA-15 is essentially maintained after deposition of vanadia (Figure S 3-3), but the support (Table S 3-1) loses roughly half of its specific surface area (Table 3-2, Table S 3-1), which is mainly due to blockage of micropores by vanadium oxide species (Table S 3-1). Ninety percent of the micropores are not accessible anymore for nitrogen adsorption after V deposition. Therefore, it is uncertain whether all the supported vanadium oxide species are accessible by molecules reacting from the gas phase. Therefore, the surface density of 1.9 V atoms nm^{-2} (Table 3-2) calculated based on the V content is rather an apparent value even though Raman spectroscopy (Figure S 3-5) confirms high vanadium oxide dispersion under reaction conditions.

The nanostructured carbon catalyst is a composite of agglomerates of closely packed multi-wall carbon nanotubes (MWCNTs) (Figure S 3-6). The catalyst possesses a comparatively small quantity of meso- and micropores (Figure S 3-3, Table S 3-1). This indicates that stabilization of the CNTs with phosphoric acid leads to loss of microporosity. The Raman spectrum of P/oCNTs (Figure S 3-7) shows bands at 1330, 1590 and 1610 cm^{-1}, denoted by D1, G, and D2 bands, respectively, in the literature,[19] indicating defective/amorphous (D1, D2) as well as crystalline/graphitic (G) carbon domains. In addition to carbon, the catalyst contains 4.9 wt% oxygen (including oxygen of phosphate) and 1.2 wt% phosphorus, which was introduced via impregnation using ammonium hydrogen phosphate in order to increase the thermal stability and resistance against oxidation.[20] The density of surface oxygen less the amount associated with phosphorous is 2.8 O atoms nm^{-2}, calculated based on XPS measurements (Figure S 3-8).

Table 3-2 Specific surface areas of the catalysts, concentrations of the presumed active catalyst component VO_x or O, respectively, reaction rates and kinetic parameters in the oxidative dehydrogenation of propane and ethane.

		M1	6V/SBA-15	P/oCNT
S_{BET} ($m^2\ g^{-1}$)		10.6	355	229
Total content of V (M1 and 6V/SBA-15) and O (P/oCNT)[a] (wt%)		7.2	5.6	2.5
Number of surface V (M1 and 6V/SBA-15) and O (P/oCNT) atoms[b] (atoms g^{-1})		$1.8 \cdot 10^{19}$	$6.7 \cdot 10^{20}$	$6.4 \cdot 10^{20}$
Surface concentration of V (M1 and 6V/SBA-15) and O (P/oCNT)[b] atoms (μmol g^{-1})		30	1113	1063
Surface density of V (M1 and 6V/SBA-15) and O (P/oCNT) atoms[b] (atoms nm^{-2})		1.7	1.9	2.8
Density of adsorbed propane (at constant heat of adsorption) (nm^{-2})[c]		0.44 (63 kJ mol^{-1})	0.0014 (52 kJ mol^{-1})	0.013 (36 kJ mol^{-1})
			0.0114 (44 kJ mol^{-1})	
Differential heat of adsorption of propane (kJ mol^{-1})		63	52-44	36
Differential heat of adsorption of ethane (kJ mol^{-1})		34	14	14
Ethane	$r_{\text{ethane consumption},0}$[d] (mmol $g^{-1}\ h^{-1}$)	5.4±0.2	0.055±0.001	0.030±0.001
	$r_{\text{ethane consumption},0}$[d] ($10^{-22}$ mmol $nm^{-2}\ h^{-1}$)	5094	1.5	1.3
	$r_{\text{ethylene formation},0}$[d] (mmol $g^{-1}\ h^{-1}$)	5.2±0.2	0.043±0.001	0.022±0.001
	$r_{\text{ethylene formation},0}$[d] ($10^{-22}$ mmol $nm^{-2}\ h^{-1}$)	4906	1.2	1.0
	$E_{a,\ \text{ethane consumption},0}$[e] (kJ mol^{-1})	90±2	121±2	110±7
	n[f](O_2)	0.1±0.01	0.2±0.01	0.4±0.02
	n[g](C_2H_6)	0.9±0.01	0.8±0.02	0.6±0.01
Propane	$r_{\text{propane consumption},0}$[h] (mmol $g^{-1}\ h^{-1}$)	5.3±0.2	0.45±0.006	0.21±0.004
	$r_{\text{propane consumption},0}$[h] ($10^{-22}$ mmol $nm^{-2}\ h^{-1}$)	5000	12.7	9.2
	$r_{\text{propylene formation},0}$[h] (mmol $g^{-1}\ h^{-1}$)	5.1±0.04	0.36±0.002	0.19±0.01
	$r_{\text{propylene formation},0}$[h] ($10^{-22}$ mmol $nm^{-2}\ h^{-1}$)	4811	10.1	8.3
	$E_{a,\ \text{propane consumption},0}$[e] (kJ mol^{-1})	80±3	110±2	103±7
	n[f](O_2)	0.1±0.01	0.3±0.01	0.4±0.01
	n[g](C_3H_8)	0.8±0.02	0.8±0.02	0.7±0.01

[a] V in case of M1 and 6V/SBA-15 as determined by XRF, O in case of P/oCNT as determined by EDX (less oxygen associated with phosphate); [b] Surface analysis of M1 and P/oCNT was performed by XPS (less oxygen associated with phosphate) (Figs. S4, S8), 6V/SBA-15 contains highly dispersed vanadium oxide (Figure S 3-5), therefore, it was assumed that all V determined by XRF corresponds to surface V; [c] determined by propane adsorption using microcalorimetry; [d] T = 380 °C, W/F = 0.06 to 0.37 g s ml^{-1} for M1, 1.33 to 2.40 g s ml^{-1} for 6V/SBA-15 and P/oCNT; [e] T = 380 – 420 °C for M1 and 6V/SBA-15 and 360 – 380 °C for P/oCNT, feed of $C_nH_{2n+2}/O_2/N_2$ = 10/5/balance [f] T = 400 °C for M1 and 6V/SBA-15 and 360 °C for P/oCNT, feed of $C_nH_{2n+2}/O_2/N_2$ = 10/3 to 7/balance; [g] T = 400 °C for M1 and 6V/SBA-15 and 360 °C for P/oCNT, feed of $C_nH_{2n+2}/O_2/N_2$ = 6 to 14/5/balance; [h] T = 380°C, W/F = 0.06 to 0.09 g s ml^{-1} for M1, 1.34 to 2.00 g s ml^{-1} for 6V/SBA-15 and P/oCNT.

3.2.2 Oxidative dehydrogenation of ethane and propane

Oxidative dehydrogenation has been performed in the same feed and temperature range over all three catalysts, but at different contact times to compensate differences in the

activity. Low conversion was adjusted to avoid consecutive reactions that prevail at higher conversion. The selectivity towards the alkene in ODH of (a) ethane and (b) propane at temperatures from 360 to 420 °C are compared in Figure 3-1 for all catalysts as a function of alkane conversion.

Pure silica SBA-15 shows measurable conversion in the studied temperature range (Figure 3-1). The increasing olefin selectivity (12 – 16% ethylene, 39 – 41% propylene) with increasing alkane conversion is a hint that gas-phase reactions or surface-initiated gas-phase reactions dominate over pure SBA-15. The opposing trends visible in Figure 3-1 for SBA-15 and 6V/SBA-15 indicate that contributions of the free silica surface to the reactivity of the sub-monolayer catalyst 6V/SBA-15 are negligible.

The three catalysts show significant differences in the selectivity towards ethylene (Figure 3-1a), while the selectivity to propylene seems to follow a similar trend with increasing conversion for all three catalysts (Figure 3-1b).

Despite its low reactivity, ethylene is further oxidized in particular over 6V/SBA-15. The selectivity of all products as a function of conversion measured in the entire range of applied temperatures and contact times is presented in Figure 3-2 to Figure 3-4.

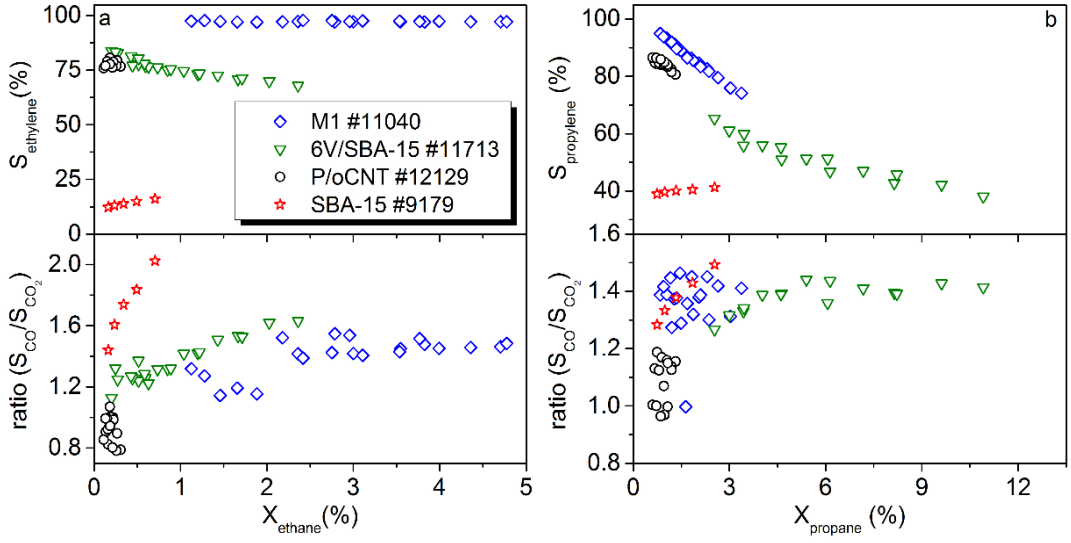

Figure 3-1 Selectivity as a function of alkane conversion in ODH of (a) ethane and (b) propane over the model catalysts at T = 360 – 420°C, W/F = 0.034 – 0.72 g s ml^{-1} (M1) 1.1 – 2.4 g s ml^{-1} (6V/SBA-15 and P/oCNT) and 2.0 g s ml^{-1} (SBA-15) in a feed composed of $C_nH_{2n+2}/O_2/N_2$ = 10/5/85.

MoVTeNb M1 oxide shows an outstanding ethylene selectivity of 95% up to 50% conversion of ethane (Figure 3-2a). Only small amounts of acetic acid are formed. Further products are CO and CO_2, which are not formed in a common path, since the S_{CO}/S_{CO2} ratio is only constant at low conversion (Figure 3-1a), but increases with increasing ethane conversion (Figure 3-2a). Acrylic acid is formed as a stable oxidation product of propylene over M1 (Figure 3-2b), but only traces of acids are observed over 6V/SBA-15 (Figure 3-3a and b).

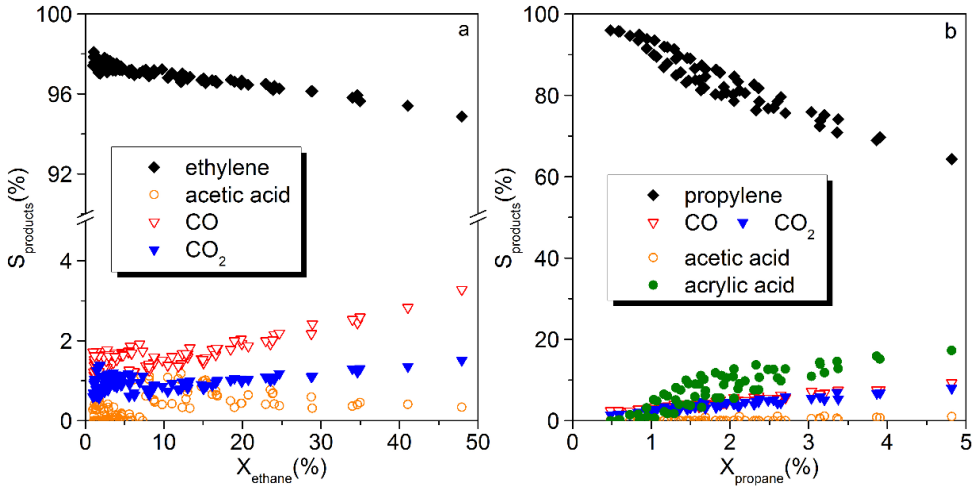

Figure 3-2 Selectivity of reaction products (labelled in the legend) as a function of alkane conversion in the oxidation of ethane (a) and propane (b) over MoVTeNb M1 oxide under the following reaction conditions: T = 350 – 420 °C, Feed $C_nH_{2n+2}/O_2/N_2$ = 10/5/85, W/F = 0.03 – 0.72 g s ml^{-1}.

Since oxygenated products have been detected at all, the low selectivity to oxygenates over 6V/SBA-15 and P/oCNTs could be rather explained by fast post-combustion of oxygen containing intermediates than by the absence of catalytic sites that accomplish oxygen insertion. Indeed, it has been shown that carbon nanotubes can catalyse the oxidation of acrolein to acrylic acid.[21]

Due to the low activity of P/oCNTs and restrictions in the reactor dimensions, the data shown in Figure 3-4a have been measured at extremely low conversions between 0.1 % and 0.3 %. In this range, the selectivity to ethylene is constant at almost 80 %. At such low conversions, minor contributions due to the combustion of the catalyst itself may become noticeable and may contribute to the selectivity to carbon oxides. Using a kinetic

model that describes the combustion of CNTs in oxygen atmosphere,[20] the rate of carbon combustion r_{ox} under the present reaction conditions (but assuming that the feed contains only 5% O_2 in N_2) was calculated resulting in a ratio of hydrocarbon conversion r to r_{ox} of 2. The impact of catalyst degeneration is certainly lower in presence of the hydrocarbon in the feed and is negligible at higher conversion as also demonstrated by the high stability of the P/oCNT catalyst over a term of 13-20 days on stream (Figure S 3-9).

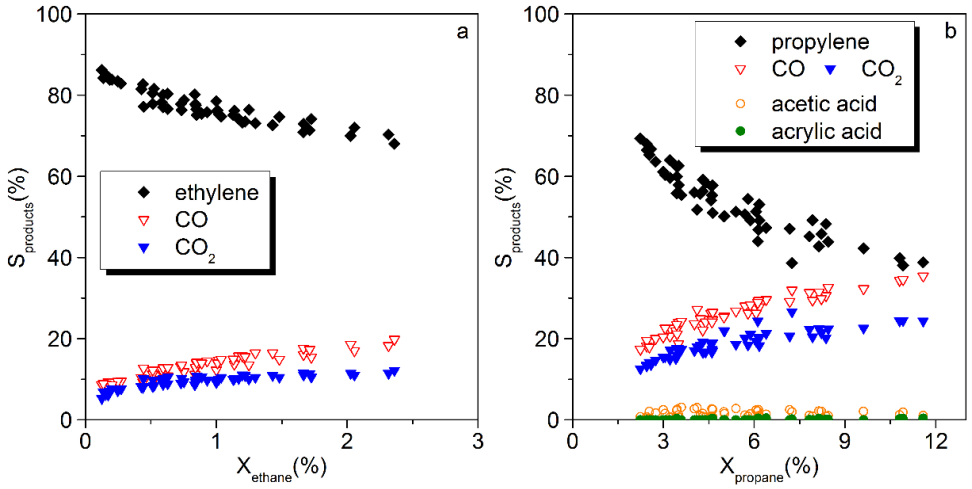

Figure 3-3 Selectivity of reaction products (labelled in the legend) as a function of alkane conversion in the oxidation of ethane (a) and propane (b) over 6V/SBA-15 under the following reaction conditions: T = 350 – 420 °C, Feed $C_nH_{2n+2}/O_2/N_2$ = 10/5/85, W/F = 0.82 – 2.40 g s ml^{-1}.

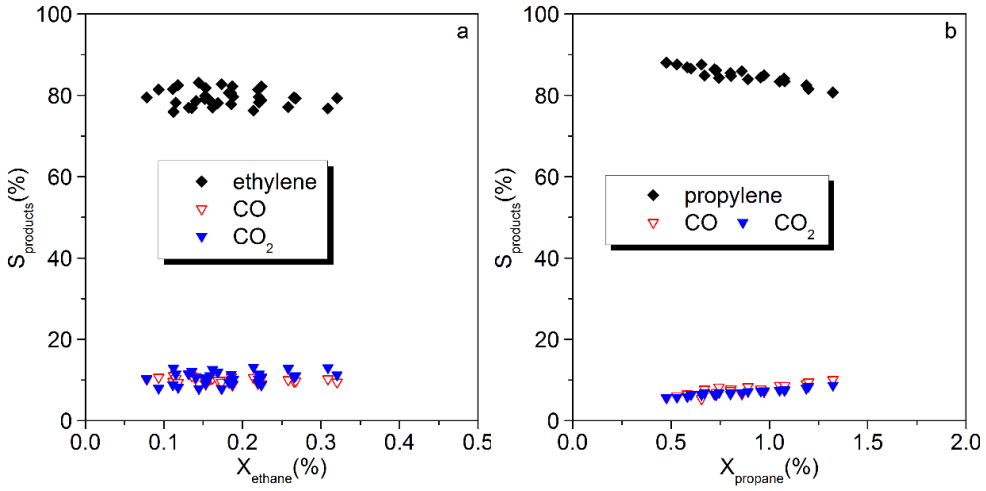

Figure 3-4 Selectivity of reaction products (labelled in the legend) as a function of alkane conversion in the oxidation of ethane (a) and propane (b) over P/oCNT under the following reaction conditions: T = 360 – 480 °C, Feed $C_nH_{2n+2}/O_2/N_2$ = 10/5/85, W/F = 0.67 – 2.00 g s ml^{-1}.

The consumption rate of the alkanes extrapolated to zero conversion (r_0) at 380 °C decreases in the order M1 >> 6V/SBA-15 > P/oCNTs (Table 3-2), irrespective of the nature of the hydrocarbon substrate. The M1 catalyst is by an order of magnitude more active in propane oxidation than sub-monolayer vanadium oxide and the transition metal-free catalyst. In case of oxidative dehydrogenation of ethane this difference comprises even two orders of magnitude. Interestingly, over M1 the rates of propane and ethane consumption, respectively, are practically the same. In contrast, ethane is more difficult to activate compared to propane over 6V/SBA-15 and P/oCNT.

The differences in activity between the three different types of catalysts can be caused by differences in the number and/or nature of active sites. Assuming that vanadium oxide species are the only active sites for C-H activation of alkanes in both, MoVTeNb M1 oxide and 6V/SBA-15 catalysts, the vanadium species located at the surface of MoVTeNb M1 oxide are much more active compared to vanadium oxide supported on SiO_2. This results from a rough estimation of the surface density of vanadium (Table 3-2). The number of surface V atoms present in 1 g M1 catalyst corresponds to approximately $1.8 \cdot 10^{19}$ atoms. The number of V atoms at the surface of 1 g 6V/SBA-15 is significantly higher ($6.7 \cdot 10^{20}$ atoms) and in the same order of magnitude as the surface oxygen atoms in 1g P/oCNT ($6.4 \cdot 10^{20}$ atoms). Contributions of the other elements at the surface of M1 cannot be excluded since, for example, supported molybdenum and niobium oxides are also active in the oxidative dehydrogenation of propane and ethane.[22] But still, due to the low specific surface area of the MoVTeNb M1 oxide, the total number of active sites in the reactor would be smaller compared to 6V/SBA-15 even if a part of the vanadium on SBA-15 should be trapped in micropores. In summary, the apparent difference in the number of active sites suggests a significant higher intrinsic activity of the active sites at the surface of M1.

The stable catalytic performance of all three catalysts at all reaction temperatures (exemplarily shown in Figure S 3-9 for selected reaction temperatures in the ODH of propane and ethane) allowed the analysis of kinetic parameters (Figure S 3-10 to Figure S 3-19, Table 3-2). Apparent activation energies (E_a) for alkane consumption were calculated based on the initial alkane consumption rates by extrapolating to zero conversion (Table 3-2). Mass transport limitations as reason for differences in the

activation energy between the three catalysts can be excluded (Figure S 3-10). The low apparent activation energy measured over M1 is in agreement with its high intrinsic activity (Table 3-2). 6V/SBA-15 shows the strongest temperature dependence, followed by P/oCNT. The apparent activation energy calculated from the alkane consumption rate is higher for ethane compared to propane. Interestingly, the difference with reference to all three catalysts is nearly the same (approximately 10 kJ mol^{-1} (Table 3-2)).

The apparent reaction order with respect to the alkane is slightly different over the three catalysts (Table 3-2) indicating different mechanisms of C-H bond activation in the hydrocarbon molecule over the transition metal free catalyst P/oCNT compared to the V-containing catalysts, which is in line with the results of model calculations applying density-functional theory.[23] The oxidative dehydrogenation of methane, ethane and propane was studied over two-dimensional graphene-like cluster models terminated with oxygen atoms in different configurations. The calculations reveal that the barrier for the abstraction of the first hydrogen atom (59-104 kJ mol^{-1}) by ketone groups located at the zigzag edge of the two-dimensional graphene model is generally lower than the barrier for the abstraction of the second H atom (82-106 kJ mol^{-1}) suggesting that the latter step is rate-limiting.

Oxygen activation seems to be fast over M1 under the applied reaction conditions as reflected in the low reaction order with respect to O_2, but more demanding over the vanadia monolayer catalyst and, in particular, over P/oCNT (Table 3-2). Fast oxygen activation over M1 is in agreement with the experimental observations that molecular O_2 can be activated at low reaction temperature for oxidation reactions in the liquid phase,[24] and with the absence of electrophilic oxygen species as intermediates of oxygen reduction under conditions of propane oxidation.[5b,25]

In summary, the main differences observed in oxidative dehydrogenation over the three different types of catalysts are

(1) an order of magnitude higher intrinsic activity of M1 compared to 6V/SBA-15 and P/oCNT,
(2) acids are formed over M1, but occur only in traces over 6V/SBA-15 and P/oCNT,
(3) facilitated oxygen activation over M1 compared to 6V/SBA-15 and P/oCNT.

The oxidative dehydrogenation of ethane and propane over vanadium oxide-based catalysts has been frequently analyzed in kinetic investigations implementing for example Eley-Rideal,[26] Langmuir-Hinshelwood,[27] and Mars-van Krevelen[22a] formalisms. In the present work, the experimental data of propane oxidation have been fitted applying a simple model-free time-law (Equation 3-1) based on reaction networks presented in Scheme 3-2 assuming irreversibility, first order with respect to the hydrocarbon, and zero order with respect to oxygen.

$$r = k \cdot \left(\frac{p_{C_3H_8}}{p_0} \right)^m \cdot \left(\frac{p_{O_2}}{p_0} \right)^n$$

Equation 3-1 Applied rate equation.

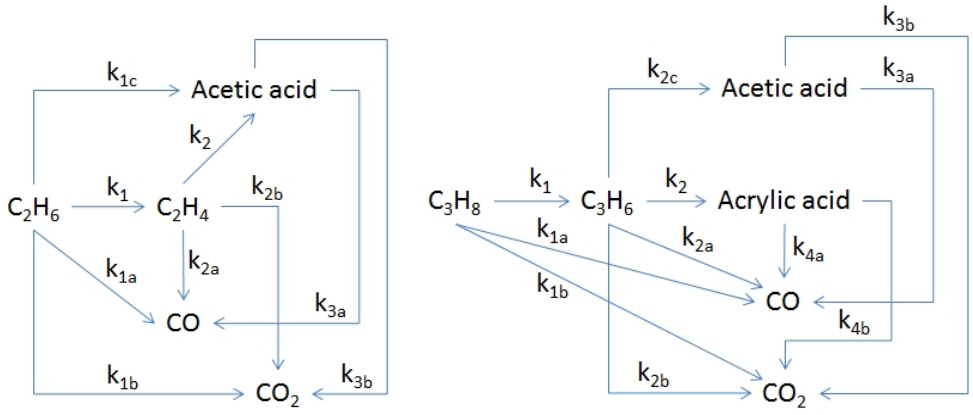

Scheme 3-2 Assumed reaction networks in oxidative dehydrogenation of ethane (left) and propane (right). The system of equations used for the simulation is presented in Scheme S 3-1 for ethane, and Scheme S 3-2 for propane, respectively, in the Supporting Information.

All products detected in the gas phase have been included into the simulation with the aim to identify the most relevant reaction intermediates that may be responsible for the observed selectivity patterns. Simulations were not performed for ethane oxidation due to the lower conversions and, consequently, larger errors. The fitting results are compared with the experimental data in the Supporting Information (Figure S 3-20 to Figure S 3-22). The measured data points can be fitted with the same model for all three catalysts implying that the deviating selectivity patterns are a result of differences in the rate

constants, but the reaction network is basically the same within the range of the studied reaction conditions. The calculated rate constants for all three catalysts are summarized in Table S 3-2. For better comparison of the catalysts, the rate constants were normalized with respect to k_1. A graphical representation of the normalized values is presented in Figure 3-5, the respective numerical values are summarized in Table S 3-3.

M1

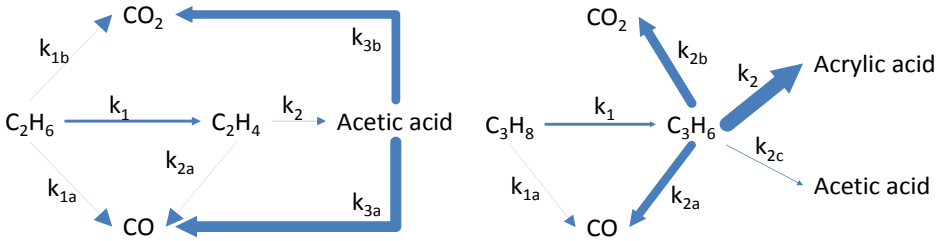

6V/SBA-15

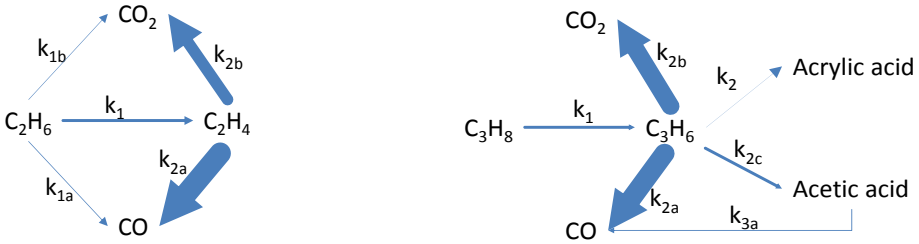

P/oCNT

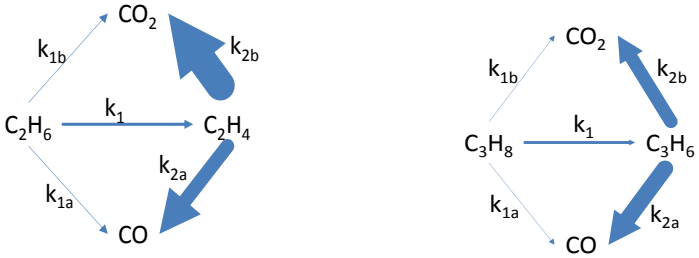

Figure 3-5 Graphical representation of the simulated rate constants in the oxidative dehydrogenation of ethane (left) and propane (right) over the three catalysts MoVTeNb M1 oxide, 6V/SBA-15, and P/oCNT normalized to k_1 based on the models presented in Scheme 3-2.

The normalized rate constants k_{1a}, and k_{1b}, that represent deep oxidation of the alkane without desorption of an intermediate, as well as the rate constants k_{2a}, and k_{2b}, that

correspond to deep oxidation of the desired olefin, are one or more orders of magnitude higher for the sub-monolayer vanadium oxide catalyst and the carbon catalyst compared to M1.

Interestingly, acetic acid formed over M1 under reaction conditions of oxidative dehydrogenation of ethane seems to be much more prone to total oxidation compared to acetic acid formed under conditions of ODH of propane. An increasing conductivity and a decreasing work function of MoVTeNb M1 oxide under operation in alkane oxidation have been measured by changing the organic substrate from ethane to propane to n-butane.[28a] This indicates progressive reduction of M1 under reaction conditions with increasing chain length of the substrate hydrocarbon. In other words, the surface of MoVTeNb M1 oxide is more oxidized in ethane containing feed compared to propane containing feed. These differences are apparently reflected in the product distribution, e.g., via consecutive reactions of the acids formed.

The olefin, especially propylene, is quite selectively converted into acrylic acid by oxygen insertion over M1, while over 6V/SBA-15 and P/oCNT consecutive combustion of propylene contributes significantly to the product distribution. Based on rate constants resulting from our simulation (Scheme 3-2 right, Scheme S 3-2, rate constants summarized exemplarily for one reaction temperature in Table S 3-2), apparent activation energies of the most significant reaction steps in oxidative dehydrogenation of propane (Figure 3-5) have been calculated (Table 3-3). Reaction steps that exhibit rate constants in the dimension of 10^{-2} or smaller (Table S 3-2) have not been taken into account.

Table 3-3 Calculated apparent activation energies of the most significant reaction steps (Figure 3-5) in oxidative dehydrogenation of propane over MoVTeNb M1 oxide, and 6V/SBA-15 (T = 380 – 420 °C) and over P/oCNT (T = 360 – 380 °C).

	M1 (kJ mol^{-1})	6V/SBA-15 (kJ mol^{-1})	P/oCNT (kJ mol^{-1})
$E_{a,k1}$	86	110	100
$E_{a,k2}$	65	-	-
$E_{a,k2a}$	90	59	50
$E_{a,k2b}$	70	58	47

The calculated E_a values of the first step, which is the oxidative dehydrogenation of propane to propylene ($E_{a,k1}$), are in good accordance with the apparent activation energies calculated based on the experimentally determined initial propane consumption rates $r_{\text{propane consumption},0}$ (Table 3-2). The agreement indicates that our simplified model describes the reaction network satisfactorily at least with respect to the first reaction step. Calculated activation energies of the consecutive unselective pathways of propylene to CO_2 and CO, $E_{a,k2a}$ and $E_{a,k2b}$, respectively, are about 50 kJ mol^{-1} lower than $E_{a,k1}$ as far as the catalysts 6V/SBA-15 and P/oCNT are concerned. Such a difference has also been found by Chen *et al.* in their study of zirconia-supported vanadia catalysts in oxidative dehydrogenation of propane.[22a] In contrast, deep oxidation pathways of propylene to carbon oxides have higher (CO formation) or only slightly lower (CO_2 formation) apparent activation energies relative to $E_{a,k1}$ over M1. As regards M1, the calculated activation energy of the route from propylene to acrylic acid ($E_{a,k2}$) is lower than the E_a of the deep oxidation pathways to CO and CO_2. This implies that the energy of the highest transition state in the course of the acrylic acid formation route k_2 might be less than the energy of the highest transition states in deep oxidation routes of propylene over M1. Generally, E_a calculated for all consecutive reactions of propylene are lower than E_a for formation of propylene in the first reaction step, except reaction of propylene to CO over M1. The varying difference between E_a of propane and propylene consumption reactions observed for the three catalysts reflects the differences in their selectivity patterns.

3.2.3 Adsorption of alkanes and alkenes

Differential heats of adsorption of the reactants ethane and propane and the reaction products ethylene and propylene measured by microcalorimetry at 40 °C on all catalysts pretreated in the calorimeter cell in the reaction feed under steady-state conditions are shown in Figure 3-6.

Few sites (0.3 μmol g^{-1}) at the surface of M1 pretreated in the ODH feed adsorb propane strongly, which is reflected in high heats of adsorption of 79 kJ mol^{-1} (Figure 3-6a, dark blue line). These sites may be attributed to tellurium oxide surface species.[6] Other sites (7.7 μmol g^{-1}) show slightly weaker interaction with propane (63 kJ mol^{-1}) and are more characteristic for adsorption at vanadium oxide.[6] With increasing coverage the heat of

adsorption decreases strictly and approaches a value of 20 kJ mol^{-1}, which is close to the heat of propane condensation. Apparently, the surface of M1 exposed to ODH conditions (dry and rich in alkane) differs drastically from the surface of M1 that has been exposed to a more lean feed that contains 40 % steam as usually applied when acrylic acid is the target product in propane oxidation. Here, propane is adsorbed with constant heat of adsorption of 40 kJ mol^{-1} until the monolayer is reached.[6] The time constants of the heat signals measured in the present experiment at low coverage are slightly increased indicating C-H activation of propane already at room temperature. The product of this interaction is not strongly adsorbed at the high-energy sites, since re-adsorption after evacuation at 40 °C (light blue line in Figure 3-6b) can be considered as reversible within the measurement accuracy.

Adsorption of propylene on M1 after two propane adsorption experiments shows lower heats of adsorption compared to propane, and reduced adsorption capacity. Moreover, propylene adsorption is partially irreversible. FTIR spectroscopy after 20 hours interaction of propylene with M1 performed to simulate the microcalorimetry experiment (Figure 3-7, blue spectrum) confirms that adsorbed oxygenates are formed already at room temperature. All bands visible in Figure 3-7 are due to adsorbed and gas-phase species, since the spectrum of the pretreated catalyst has been used as reference. The intense bands between 1900-1800, 1700-1600, and 1500-1300 cm^{-1} originate from gas-phase propylene. The peaks due to adsorbed species are marked in Figure 3-7. The band at 1556 cm^{-1} is attributed to the asymmetric COO stretching vibration of adsorbed carboxylate groups, while the peaks below 1300 cm^{-1} originate from various surface alcoholate species.[29] Due to the strong interaction of propylene with M1, irreversible adsorbed intermediates of selective oxidation products are already formed at 40 °C providing an explanation for partial irreversible adsorption.

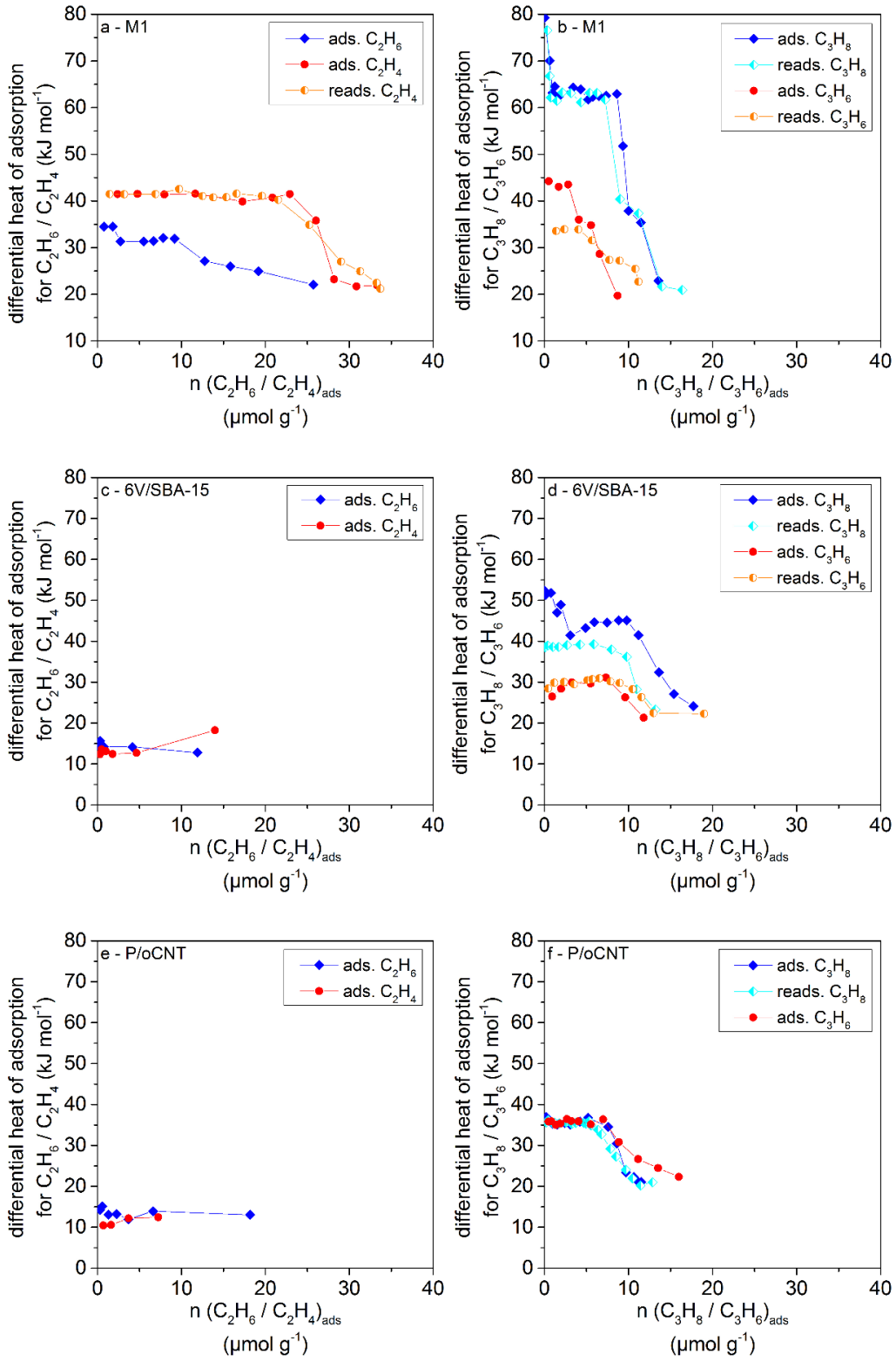

Figure 3-6 Differential heats of adsorption of the reactants ethane and propane and the products ethylene and propylene (as indicated in the legends) adsorbed at the catalysts M1 (a, b), 6V/SBA-15 (c, d) and P/oCNT (e, f) pretreated under steady-state conditions in the oxidation of propane and ethane, respectively.

Ethane shows a weaker interaction with the surface of M1 compared to propane (Figure 3-6a, blue line), reflected in a heat of adsorption of 34 kJ mol^{-1} (1.8 µmol g^{-1}). With increasing coverage, weaker sites are occupied (30-20 kJ mol^{-1}). Ethane adsorption is completely reversible. Subsequent ethylene adsorption reveals that ethylene interacts stronger with M1 than ethane (Figure 3-6a, red line) (41 kJ mol^{-1}), but still, the adsorption is reversible (Figure 3-6a, orange line). Due to the smaller size, adsorption capacity of C_2 hydrocarbons on M1 is higher compared to C_3 hydrocarbons.

At 6V/SBA-15 (Figure 3-6d, dark blue line), a few sites (0.8 µmol g^{-1}) are characterized by a heat of propane adsorption of 52 kJ mol^{-1}, which exhibit strong interaction with propane. At higher coverage from 0.8 to 10 µmol g^{-1} the heat of adsorption decreases to 44 kJ mol^{-1} on average. Adsorption of propane on 6V/SBA-15 changes the nature of the adsorption sites and also slightly the amount since readsorption of propane after evacuation at 40 °C follows a different curve compared to the first adsorption experiment (Figure 3-6d, light blue line) showing a plateau at 39 kJ mol^{-1} (8 µmol g^{-1}) and an overall reduced adsorption capacity. Interestingly, the amount of propane adsorbed at 6V/SBA-15 with a heat higher than the heat of condensation is similar compared to M1 although the number of surface vanadium atoms on 6V/SBA-15 is much higher (Table 3-2).

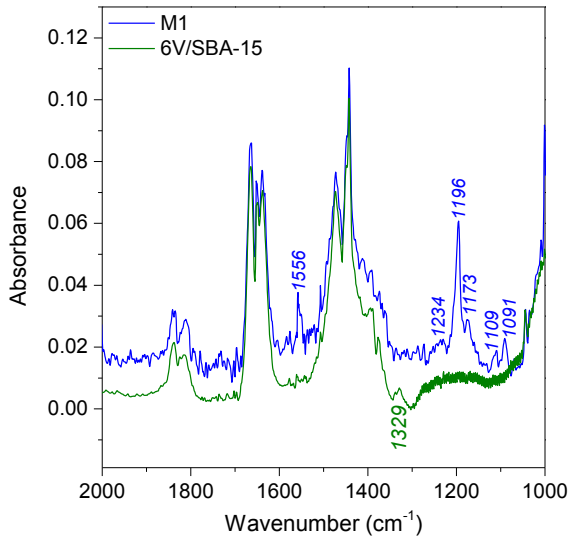

Figure 3-7 FTIR spectra of adsorbed species at the surface of M1 and 6V/SBA-15 after adsorption of propylene at 40 °C for 20 hours in presence of 10 mbar propylene (equilibrium pressure). The peaks labelled with band positions arise for adsorbed species.

Propylene gives low heats of 30 kJ mol^{-1} at coverage of 10 µmol g^{-1}. The formation of carboxylate species at the surface of 6V/SBA-15 can be excluded due to the absence of bands in the window between 1600 and 1500 cm^{-1} in the infrared spectrum of propylene adsorbed on 6V/SBA-15 (Figure 3-7). This suggests that the intermediate product propylene interacts differently with 6V/SBA-15 and M1, respectively. Unfortunately, the region below 1300 cm^{-1} is not accessible due to complete absorption of the infrared light by the silica support (Figure 3-7) and possibly adsorbed alkoxide species cannot be probed.

Adsorption measurements of ethane and ethylene on 6V/SBA-15 yield a low heat of 14 kJ mol^{-1}, which is equal to the heat of condensation of the molecules (Figure 3-6c). There is no specific interaction with the vanadium oxide species at the surface.

Propane adsorption on P/oCNT is reversible with a heat of 36 kJ mol^{-1} and a coverage of 5 µmol g^{-1} (Figure 3-6f), which corresponds to the interaction with surface functional groups.[30] The amount of adsorbed propane is comparable with the other two catalysts. Propylene adsorption on P/oCNT is reversible exhibiting coverages of 7 µmol g^{-1} and an adsorption heat of 36 kJ mol^{-1}. Adsorption measurements of ethane and ethylene on P/oCNT yield a low heat of 14 kJ mol^{-1} that corresponds to the heat of condensation (Figure 3-6e). There is no specific interaction with the oxygen containing functional groups at the surface.

In summary, all hydrocarbon molecules are stronger adsorbed and reach a much higher surface concentration on M1 (Table 3-2) as compared to 6V/SBA-15 and P/oCNT. Interestingly, the mean ratio of surface vanadium atoms relative to adsorbed propane molecules $V_{surface}/C_3H_{8ads}$ (Table 3-2) corresponds to approximately 4 in case of M1 and 150 in case of 6V/SBA-15 revealing that only a part of the vanadium oxide species in 6V/SBA-15 (approximately 1%) adsorb propane. In this respect it is notable that tetramers of vanadium oxide species have been postulated to be the required ensemble size for oxidative dehydrogenation of propane.[2] The heat of adsorption increases with the chain length of the hydrocarbon molecule on all catalysts. Propylene reacts slowly with the surface of M1 already at room temperature under formation of carboxylates. Carboxylates are not formed on the other two catalysts.

3.3 Concluding Discussion

The present study highlights three model catalysts with substantial structural diversity, which all are capable to catalyse the oxidative dehydrogenation of ethane and propane. The two V-containing catalysts represent sub-monolayer catalysts. On the one hand vanadium oxide species are supported on silica as an insulating support (6V/SBA-15). On the other hand a monolayer enriched in V^{5+} and Te^{4+} is self-supported on a crystalline multi-metal mixed oxide (MoVTeNb M1 oxide) that exhibits the electronic properties of a n-type semiconductor.[28] The third type of catalyst is composed of surface-functionalized carbon nanotubes (P/oCNT) that contain neither vanadium oxide nor bulk oxygen, but only surface oxygen species of which quinone-hydroquinone groups are assumed to be the active redox couple.

The catalytic performance of the three catalysts has been compared under identical reaction conditions in terms of temperature and feed composition. The results reveal general similarities such as the alkenes being the main reaction products and CO is preferentially formed compared to CO_2 as product of deeper oxidation. However, the overall by-product spectrum and the macrokinetic parameters show the following remarkable differences:

1. The rate of alkene formation is 1-2 orders of magnitude higher over M1 compared to 6V/SBA-15 and P/oCNT.
2. Interestingly, the rate of olefin formation over M1 is approximately the same in oxidative dehydrogenation of ethane and propane. On the other two catalysts, bigger differences in the reactivity of the two alkane molecules are observed.
3. The three catalysts show different selectivity to the olefin at similar conversion. The spectrum of by-products differs as well.

3.3.1 Differences in activity

We propose that the different density of alkane adsorption sites (Table 3-2) is responsible for differences in the activity of M1, 6V/SBA-15 and P/oCNT. Despite the fact that more potential V or oxygen adsorption sites per g catalyst are available at the surface of 6V/SBA-15 and P/oCNT, respectively, (Table 3-2), M1 adsorbs more alkane molecules per nm^2 surface (Table 3-2, density of propane adsorption sites) and overall a similar

amount per g catalyst (Figure 3-6). In addition, M1 shows a higher intrinsic activity, which could be attributed to a cluster size effect (size of V_xO_y oligomers) based on the low overall V_{surf}/propane ratio of 4. It has been shown by DFT calculations that the barrier for abstraction of the first hydrogen atom under formation of a propyl radical decreases with increasing cluster size.[31] Values of 160, 148, 139 and 132 kJ mol^{-1} have been calculated for monomers, dimers, tetramers and octamers, respectively. With the assumption that all intermediates occur in pseudo-steady-state, and adsorption as well as regeneration steps are in quasi-equilibrium,[22a] the overall barrier for propylene formation can be estimated based on measured adsorption enthalpies (Figure 3-6, Table 3-2) and apparent activation energies in propane oxidation (Table 3-2). The estimation is based on the assumption that the heat of adsorption is nearly independent of the temperature.[32] The thus calculated intrinsic barrier for propane activation increases in the order P/oCNT (139 kJ mol^{-1}) ≤ M1 (143 kJ mol^{-1}) < 6V/SBA-15 (162 kJ mol^{-1}). The similar values for P/oCNT and M1 suggest similar C-H activation mechanisms over these two catalysts. The high value for 6V/SBA-15 is in agreement with the high dispersion of vanadium in 6V/SBA-15. The latter barrier has been calculated based on the heat of propane adsorption of 52 kJ mol^{-1} (Figure 3-6, Table 3-2) that correspond to a density of adsorption sites of 0.0014 nm^{-2} on 6V/SBA-15 (Table 3-2). According to the DFT calculations by Rozanska *et al.*,[31a] these sites could be monomeric species that comprise approximately 0.1% of all V atoms. At higher coverage propane adsorbs with a higher density of 0.0114 nm^{-2} on a different type of sites with a heat of adsorption of 44 kJ mol^{-1}. For these sites a slightly lower barrier of 154 kJ mol^{-1} can be estimated, which is close to the value calculated for silica-supported vanadium oxide dimers (0.6% of all V atoms).[31a] Hence, microcalorimetry apparently allows the determination and quantification of propane adsorption sites in vanadium oxide monolayer catalysts and resolves different degrees of V_xO_y oligomerization.

Intrinsic barriers for ethane activation are (124 kJ mol^{-1}) for M1, and (135 kJ mol^{-1}) for 6V/SBA-15, which is also in agreement with the activity difference.

3.3.2 Differences in selectivity

Hydrogen abstraction is the rate-determining step in ODH of alkanes. Therefore, the discussion above refers only to the differences in the activity. Selectivity, however, is determined by the relative values of the rate constants of the various consecutive and parallel reactions or differences in the reaction pathways, which are basically not known in great detail due to the complexity of the reaction network. Batiot and Hodnett analysed a number of oxidation reactions and observed a correlation between selectivity at fixed conversion and the difference between the bond dissociation enthalpy of the weakest C-H bond in the reactant and the bond dissociation enthalpy of the weakest bond in the selective oxidation product irrespective of the type of oxide-based catalyst that has been used.[33] The concept implies that energetic constraints limit selectivity in oxidation catalysis. It provides a rule of thumb to estimate the threshold value of selectivity that depends on the gas-phase stability of reactant and product. The selectivity to ethylene is expected to be high if the reaction stops at the formation of ethylene since the weakest C-H bond in ethane (bond dissociation energy $D^0_{C\text{-}H} = 419.5$ kJ mol^{-1}) can be activated more readily than the weakest C-H bond in ethylene ($D^0_{C\text{-}H} = 444$ kJ mol^{-1}).[33] In the current work, however, a much higher selectivity to ethylene is observed over M1 compared to 6V/SBA-15. The difference that comprises up to 30% is not obvious within the concept mentioned above, in particular because M1 catalyses the consecutive oxidation of ethylene to acetic acid as well and should, therefore, show a lower selectivity to ethylene. In contrast, a smaller difference between M1 and 6V/SBA-15 is observed in the selectivity to propylene in ODH of propane (10%) under the applied reaction conditions. The result is again not straightforward, because the product distribution of the two catalysts in propane oxidation is very different. The current work illustrates that in addition to the thermodynamic stability of a substrate or product molecule the interaction of reactant or product with the catalyst surface has an impact on the selectivity.

We observed only weak interaction between propylene and the V-containing catalysts, which is an unexpected result. Propylene adsorption on M1 yields adsorbed acrylates already at room temperature in a slow reaction. The high density of adsorption sites on M1 apparently renders possible concerted reactions, which involve oxygen insertion.

Such an ensemble effect together with the balanced oxygen activation[34] result in improved selectivity to acrylic acid over MoVTeNb M1 oxide.

Vanadium oxide supported on an insulating support behaves electronically more like a single-site catalyst, whereas the selectivity over a semiconducting catalyst, such as M1, can be controlled by the redox-level of the (dynamic) surface layer that has an impact on the surface potential barrier, which again determines charge transfer between adsorbed molecules and the catalyst as will be explained in detail below.[34] Comparable dynamic properties have not been proven so far on monolayer catalysts under reaction conditions. The presented results imply that the validity is limited of vanadium oxide monolayers supported on insulating supports to serve as a model for the surface layer of V-containing bulk catalysts. Studies using isotope labeled reactants are underway to further elucidate the differences in the reaction mechanism.

3.3.3 Materials science of model catalysts

The investigated catalysts represent three classes of materials with differing electronic properties. The presented results imply that counting the local density of specific structural elements (V_xO_y oligomers, quinone-hydroquinone couples) is a necessary but insufficient description of the material science required for generating an active and selective catalyst. The electronic properties with respect to charge carriers controlling the overall potential of the active structural elements needs also to be put into consideration. This is often done implicitly by choosing the "support" of an active structure. Figure 3-8 schematically indicates this by illustrating how the charge carriers of an assumed redox reaction are transported from the energy level of the hydrocarbon substrate to the energy level of oxygen. This downhill in energy provides an elementary driving force for the reaction to occur. It may thus be expected that the ease of charge carrier transport will affect the observed kinetics of the reaction. In agreement with the well-known concept of selectivity being the consequence of reactant abundance it can be expected that the ease of charge carrier transport limits selectivity. Resultant is the observation that fast reactions are not so selective and selective reactions are not so fast.

The semiconductor M1 with a termination layer containing V_xO_y is characterized by a situation of band bending caused by formation of surface states in the feed of the reactant

(Figure 3-8a).[28a] This allows connecting the electron donor level of the hydrocarbon with the electron acceptor level of the adsorbed oxygen sitting on the V_xO_y d-states of the active clusters. In this way a self-limiting charge carrier transport situation is created. A facile execution of the elementary steps of hydrocarbon oxidation and oxygen reduction occurs through charge carriers from the catalyst and the steady state is maintained by provision of charge carriers from the reactants.

In Figure 3-8b the situation is shown for V_xO_y supported on the insulator silica. Here no nearly free charge carriers exist in the material, no band bending occurs and no support of the charge carrier exchange between reactants can be expected from the bulk. Only local exchange between co-adsorbed reactants can cause catalytic reaction. This requires highly special geometric situations of V_xO_y clusters that can store 4 redox equivalents and more than one hydrocarbon molecule plus an oxygen molecule in close proximity. It is conceivable that only few sites (1%) are structurally suitable and that combustion is facile due to the proximity of electrophilic oxygen occurring during partial charge exchange between hydrocarbon and molecular oxygen.

In Figure 3-8c, the situation of the semi-metal sp^2 carbon is displayed on which di-ketonic groups capable of undergoing charge carrier exchange with the sp^2 carbon skeleton are the active sites. Here the lack of an energy gap in the carbon backbone allows facile charge carrier exchange. The localization of the electrons in the quinoidic groups provides the energy barrier necessary for selective operation. The very low numbered density of active sites for oxygen activation requires the movement of partially activated electrophilic oxygen as we know from combustion kinetics of carbon and hence provides the opportunity for facile combustion. This mobile active oxygen counteracts the low density of active di-ketonic sites that should be suitable for selective operation and leads to the poor performance both in respect of activity and selectivity.

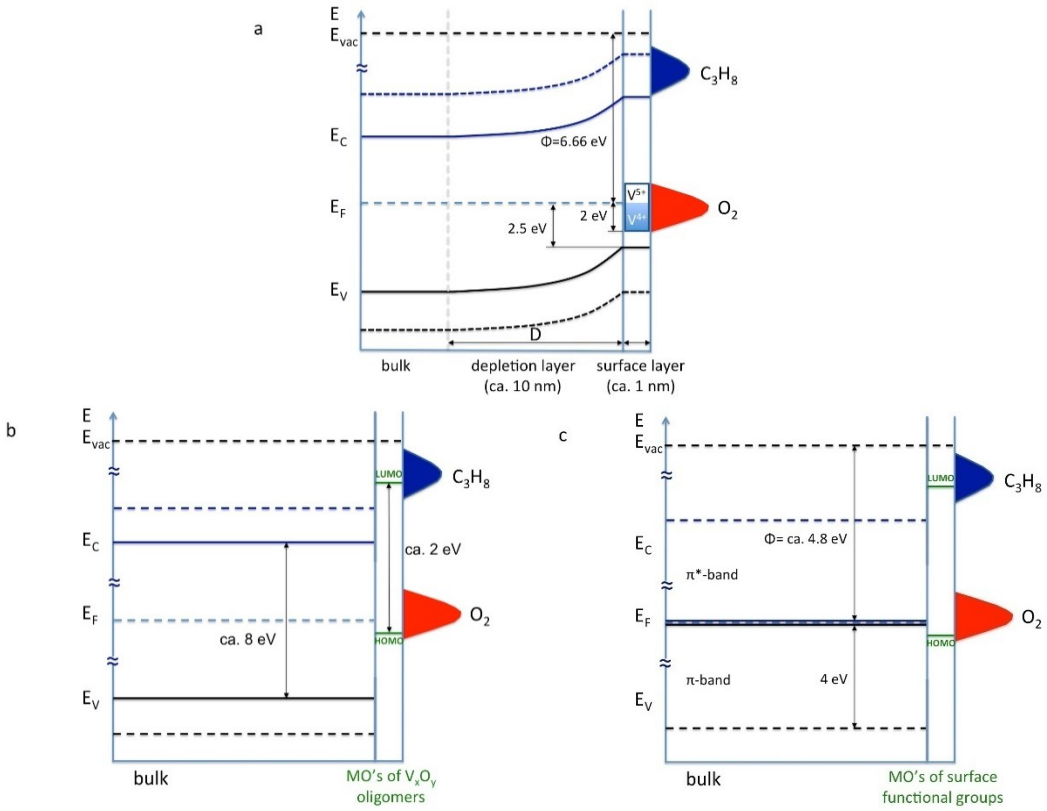

Figure 3-8 Schematic representation of the charge carrier transport situation (not true to scale) in the model catalysts (a) M1,[28a] (b) VxOy/SBA-15,[35] and (c) quinone on oCNTs.

The present study shows that fine-tuning of static and dynamic aspects of catalytic surfaces are necessary. The conventional approach focusing on a single property of a catalyst (such as the nuclearity of V_xO_y clusters or their static oxidation state for example) is insufficient to capture the complexity of the dynamical situation of a redox catalyst. Notably, the elementary processes of handling the protons and the formation of water, which is a kinetically most relevant aspect, have not been considered in the present work. This is because macro-kinetic effects of these reactions in the chosen regime of low conversion are absent here. If catalysts are operated under higher loads these aspects become relevant and complicate the picture further as then acid-base properties are additionally relevant.

3.4 Experimental Section

3.4.1 Catalyst preparation

Synthesis of MoVTeNb M1 oxide

Phase-pure M1 was synthesized according to a precipitation-purification method.[36] Briefly, 22.95 g (18.57 mmol) $(NH_4)_6Mo_7O_{24}\cdot 4H_2O$, 4.56 g (38.98 mmol) NH_4VO_3, and 6.87 g (29.91 mmol) $Te(OH)_6$ were subsequently dissolved in 100 ml H_2O at 80 °C. A solution of 7.16 g (23.63 mmol) $NH_4[NbO(C_2O_4)_2]\cdot xH_2O$ dissolved in 30 ml H_2O at 40 °C was finally added to the Mo/V/Te solution at room temperature. The obtained slurry with a nominal ratio of Mo:V:Te:Nb = 1:0.3:0.23:0.18 was spray-dried. The resulting powder was calcined at 275 °C in a flow of synthetic air (100 ml min^{-1}) for 1 h and subsequently annealed at 600 °C in a flow of Ar (100 ml min^{-1}) for 2 h. The M2 phase present in the as-prepared biphasic MoVTeNb oxide was dissolved in a 15% H_2O_2 solution at ambient temperature under continuous stirring for 24 h. The washed sample was vacuum filtrated, washed with H_2O and dried at 95 °C for 3 h. Finally, the obtained powder was treated at 600 °C for 2 h in a flow of Ar (100 ml min^{-1}) resulting in crystalline, phase-pure MoVTeNb M1 oxide (sample ID 11040). The metal composition normalized to molybdenum corresponds to $Mo_{1.0}V_{0.29}Te_{0.1}Nb_{0.15}O_x$. Results of the basic catalyst characterization are summarized in the Supporting Information. The SEM image (Figure S 3-1) reveals the typical rod-shaped microstructure of the primary catalyst particles that are composed of the M1 phase only. The Rietveld refinement results of the experimental powder X-ray diffraction patterns that confirm phase purity of the catalyst are presented in Figure S 3-2 (lattice parameters (Å): a = 21.1210(13); b = 26.5999(16); c = 4.01689(21)).

Synthesis of 6V/SBA-15

Mesoporous silica SBA-15 (sample ID 9179) was used as support. The synthesis of SBA-15 has been described in detail elsewhere.[37] Dispersed vanadia species were deposited by a grafting procedure.[37] Briefly, 11.24 g support material (dried for 16 h at 130 °C in air) was suspended in 284.4 g toluene. After 30 min, 25.58 g of a solution of 10.01 g (41.0 mmol) vanadium (V) triisopropoxide in 50.23 g toluene was added to the SBA-15 suspension and stirred for 2 h at ambient temperature. The evaporation of isopropanol

was performed in a rotary evaporator at 50 °C at a residual pressure of 50 mbar. The resulting light orange powder with a nominal V content of 6 wt% was calcined at 550 °C in static air for 2 h. The catalyst is called 6V/SBA-15 (sample ID 11713).

Synthesis of P/oCNT

Multi-walled CNTs from Nanocyl (NC3100) have been used as starting material for the synthesis of phosphorous-modified CNTs. The CNTs (sample ID 5664) were refluxed in concentrated HNO_3 for 2 h, filtrated under vacuum, washed with deionized H_2O to pH 6-7 and dried at 110 °C in air (oCNTs, sample ID 11450). Phosphorous modification was done by incipient wetness impregnation, using 30.66 ml of an aqueous $(NH_4)_2HPO_4$ solution (0.247 mol l^{-1} P) mixed with 10.22 g oCNTs and 29.34 ml H_2O to achieve a nominal loading of 5 wt% P_2O_5. The resulting paste was thoroughly kneaded in a mortar and dried at 110 °C for 4 days. The resulting catalyst is called P/oCNT (sample ID 12129).

3.4.2 Catalyst characterization

The morphology of the primary MoVTeNb M1 oxide particles was studied by scanning electron microscopy (SEM) using a Hitachi S-4800 electron microscope operating at 2 kV in secondary electron (SE) mode.

Phase analysis was performed by X-ray diffraction (XRD) using a Bruker D8 ADVANCE diffractometer (Cu Kα radiation, secondary graphite monochromator, scintillation counter). The unit cell parameters of M1 were refined by least-square fitting of the diffraction peak positions using the M1 structure (orthorhombic, space group Pba2 [ICSD 55097]) utilizing the program package TOPAS (v 4.2, Bruker AXS).

Nitrogen adsorption was performed at -196 °C using the Autosorb-6B analyser (Quantachrome) after outgassing the catalysts in vacuum (M1 for 2 h at 120 °C, 6V/SBA-15 for 16 h at 120 °C, P/oCNT for 2 h at 200 °C). All data treatments were performed using the Quantachrome Autosorb software package. The specific surface area S_{BET} was calculated according to the multipoint Brunauer-Emmett-Teller method (BET) in the

p/p_0 = 0.05-0.15 pressure range assuming the N_2 cross sectional area of 16.2 $Å^2$. The pore size distribution of SBA-15 and 6V/SBA-15 was determined by NLDFT method using a model based on equilibrated adsorption of N_2 on silica assuming cylindrical pores at -196 °C. The micropore surface area Sμ was estimated using the t-plot method in the statistical thickness t = 4.5-6.5 Å range. The total pore volume V_P was determined by using the amount of physisorbed nitrogen at a relative pressure p/p_0 = 0.95.

X-ray fluorescence spectroscopy (XRF) was used for elemental analysis of M1 and 6V/SBA-15 applying a Bruker S4 Pioneer X-ray spectrometer. For sample preparation, the mixture of 0.1 g of the catalyst and 8.9 g of lithium tetraborate (> 99.995 %, Aldrich) was fused into a disk using an automated fusion machine (Vulcan 2 MA, Fluxana).

Raman spectroscopic investigation of the catalyst samples was done at 532 nm excitation wavelength using a confocal TriVista microscope setup TR557 (S&I GmbH, Warstein, Germany) equipped with a liquid nitrogen cooled spectroscopy CCD system PyLoN:2kBUV and 750 mm focal length of the monochromator (Princeton Instruments). Spectra resemble an average of multiple measurements at different spots of the sample. Calcination of 6V/SBA-15 and ODP reaction have been done in a CCR1000 reactor cell (Linkam Scientific, Tadworth, UK) at 550 °C in synthetic air and in ODP feed ($C_3H_8/O_2/N_2$ = 10/5/85) at 380 °C, respectively.

In situ X-ray photoelectron spectroscopy (XPS) was performed at the synchrotron radiation facility BESSY II in Berlin. At the ISISS (Innovative Station for In Situ Spectroscopy) beamline monochromatic X-ray light was used to obtain high pressure XP spectra in the presence of reactive gases (alkane + oxygen) at elevated temperatures. Details of the vacuum system and the electronanalyser were reported before.[38] For the XPS studies 10 mg of M1 powder were pressed into a self-supporting pellet (1 ton pressing pressure, diameter of pellet: 8 mm). In the experiment, M1 was heated to 400 °C with a heating rate of 5 °C min^{-1} in the presence of alkane/oxygen feed (volume flow ratio 1 sccm/2 sccm). The total pressure was 25 Pa during the experiment. Alkanes, olefins (ethylene, propylene), CO, and CO_2 were analyzed with a micro gas

chromatograph (micro-GC, Varian) after compressing the gas to atmospheric pressure. In parallel, the oxygenates (acetic acid, acrylic acid, maleic anhydride) were detected with a proton transfer reaction mass spectrometer (PTR-MS, IONICON). Core level spectra of O1s, V2p, Mo3d, Nb3d, Te3d, and C1s were obtained with a constant kinetic electron energy of 150 eV corresponding to an inelastic mean free path (IMFP) of 0.6 nm. To calculate the elemental composition at the surface of M1, normalized core level intensities were evaluated after subtraction of a Shirley type background taking into account the photon energy dependence of the atomic subshell photoionization cross sections,[39] using CASA data analysis software (Neil Farley, www.casaxps.com). Atomic abundance for P/oCNT was performed following the same procedure and same KE (150 eV). The background was subtracted using a Shirley type. The analyzed peaks were C 1s, O1s and P 2p.

3.4.3 Catalytic tests

The catalytic tests were carried out using a setup for partial oxidation (Integrated Lab Solutions) with 8 fixed bed quartz reactors (6 mm inner diameter) in parallel. Each reactor was equipped with a thermocouple for measuring the temperature inside the catalyst bed. The catalytic performance was determined at atmospheric pressure under steady state conditions. The reactant feed comprised the hydrocarbon (C_3H_8 or C_2H_6), O_2, and N_2 as diluent. The reaction conditions have been varied and are indicated in the results part. Starting and reference point for all variations was 360 °C (P/oCNT) or 400 °C (M1, 6V/SBA-15, and SBA-15) and a dry feed of 10% hydrocarbon, 5% O_2, and 85% N_2. The catalysts were pressed under ~55 MPa, crushed and sieved to a particle size of 250-355 µm. Then, different amounts of catalyst were loaded into the reactor to realise different contact times at the same gas flow. In the case of the low amount of M1 samples, the catalyst was diluted with ~3 g of SiC (sieve fraction 250-355 µm). The calculated pressure drop was below 0.5 mbar for all loadings. A total flow of 10 ml min^{-1} was used in all experiments.

An online gas chromatograph (Agilent 7890A) is used for gas analysis. A combination of Plot-Q (length 30 m, 0.53 mm internal diameter, 40 µm film thickness) and Plot-MoleSieve 5A columns (30 m length, 0.53 mm internal diameter, 50 µm film thickness),

connected to a thermal conductivity detector (TCD), was used to analyse the permanent gases CO, CO_2, N_2, O_2, and CH_4. A system of a FFAP (length 30 m, 0.53 mm internal diameter, 1 µm film thickness) and a Plot-Q column (length 30 m, 0.53 mm internal diameter, 40 µm film thickness), connected to a flame ionization detector (FID), was used to analyse C_2-C_3 hydrocarbons and oxygenates.

Conversion of propane X and product selectivity S_k were calculated based on the sum of products as follows:

$$X = \frac{\sum_{i=1}^{n} \frac{n_i(product)}{|\nu_i|}}{\sum_{j=1}^{k} \frac{n_j(C\text{-}compounds)}{|\nu_j|}}$$

Equation 3-2 Formula for calculation of the alkane conversion.

$$S_k = \frac{N_k(C\text{-}atoms) \times n_k(product)}{\sum_{i=1}^{n} N_i(C\text{-}atoms) \times n_i(product)}, k = 1\text{K } n$$

Equation 3-3 Formula for calculation of the product selectivity.

Reaction rates for propane consumption and propylene formation were determined using the following equation.

$$\frac{d(n_i)}{d\left(\frac{W}{F}\right)} = \nu_i r_i$$

Equation 3-4 Formula for calculation of the reaction rates.

Reaction rates at zero contact time are obtained by linear extrapolation of the calculated reaction rates to W/F = 0.

Absence of external and internal transport limitations were verified by calculating the dimensionless Mears and Weisz-Prater criteria and measuring the catalyst performance for different catalyst amounts in two different gas flows (10 and 15 ml min^{-1}) (see Figure

S 3-10, data at contact time 0.06 g s ml^{-1}). The very active M1 catalyst shows the highest Mears-modulus of $3.3 \cdot 10^{-6}$ and a Weisz-Prater modulus of $1.76 \cdot 10^{-3}$ indicating that neither external nor internal mass transport limitations play a role.

3.4.4 Microcalorimetry

Differential heats of propane and propylene adsorption on used catalysts were determined at 40 °C using a MS70 Calvet Calorimeter (SETRAM). The catalysts were pretreated in the calorimeter cell in a feed of 10% hydrocarbon (C_3H_8 or C_2H_6) and 5% oxygen in helium with a total flow rate of 20 ml min^{-1}. The reaction temperature was 400 °C for 6V/SBA-15, 360 °C for P/oCNT and 350 °C for M1. The reaction was performed at steady state for 20 hours, subsequently, the cell was cooled down to room temperature in pure helium. The cell was then sealed and transferred to the calorimeter. The calorimeter is equipped with a custom-designed high vacuum and gas dosing apparatus. Hydrocarbons were stepwise introduced into the evacuated cell ($p < 3 \cdot 10^{-8}$ mbar), and the pressure evolution and the heat signal were recorded for each dosing step.

3.4.5 In-situ FTIR spectroscopy

FTIR spectra of adsorbed species at the surface were measured using a PE100 spectrometer (Perkin Elmer) equipped with a MCT detector and a homemade quartz cell, which is connected to a vacuum and gas dosing system. The spectra were recorded with 64 scans and a resolution of 4 cm^{-1}. Catalyst powders were pressed with 260 MPa into self-supported wafers and the samples were pre-treated as follows. In case of M1, the sample was heated up in vacuum to 400 °C with 10 °C min^{-1}. After a hold time of 30 min the sample was cooled to 40 °C and the final starting pressure for the experiment was $1.3.10^{-6}$ mbar. 6V/SBA-15 was heated up in 200 mbar oxygen to 550 °C with a heating rate of 10 °C min^{-1}. After 30 min hold time the sample was cooled to 100 °C. At this temperature the cell was evacuated and cooled to 40 °C. Final starting pressure for the experiment was $9.1.10^{-6}$ mbar. Propylene was stepwise introduced at 40 °C up to 10 mbar and left for 20 h under these conditions. Then the measurement was performed using the spectra of the pre-treated catalysts as reference.

3.5 Supporting Information

$$\frac{d(C_2H_6)}{dt} = -(k1 + k1a + k1b + k1c)[C_2H_6]$$
$$\frac{d(C_2H_4)}{dt} = k1[C_2H_6] - (k2 + k2a + k2b)[C_2H_4]$$
$$\frac{d(AcA)}{dt} = k1c[C_2H_6] + k2[C_2H_4] - (k3a + k3b)[AcA]$$
$$\frac{d(CO)}{dt} = k1a[C_2H_6] + k2a[C_2H_4] + k3a[AcA]$$
$$\frac{d(CO_2)}{dt} = k1b[C_2H_6] + k2b[C_2H_4] + k3b[AcA]$$

Scheme S 3-1 System of equations for kinetic modelling of the oxidative dehydrogenation of ethane.

$$\frac{d(C_3H_8)}{dt} = -(k1 + k1a + k1b)[C_3H_8]$$
$$\frac{d(C_3H_6)}{dt} = k1[C_3H_8] - (k2 + k2a + k2b + k2c)[C_3H_6]$$
$$\frac{d(AA)}{dt} = k2[C_3H_6] - (k4a + k4b)[AA]$$
$$\frac{d(AcA)}{dt} = k2c[C_3H_6] - (k3a + k3b)[AcA]$$
$$\frac{d(CO)}{dt} = k1a[C_3H_8] + k2a[C_3H_6] + k3a[AcA] + k4a[AA]$$
$$\frac{d(CO_2)}{dt} = k1b[C_3H_8] + k2b[C_3H_6] + k3b[AcA] + k4b[AA]$$

Scheme S 3-2 System of equations for kinetic modelling of the oxidative dehydrogenation of propane.

Table S 3-1 Specific surface area and textural properties of the catalysts.

Sample	S_{BET} (m^2 g^{-1})	S_μ (m^2 g^{-1})	S_μ/S_{BET}	d_P (nm)	V_P (cm^3 g^{-1})
M1	10.6	-	-	-	0.02
SBA-15	758	293	0.39	7	0.80
6V/SBA-15	355	52	0.14	7	0.55
Pristine CNTs	323	-	-	-	0.98
P/oCNT	229	-	-	-	0.88

Table S 3-2 Calculated rate constants for the oxidative dehydrogenation of ethane and propane over MoVTeNb M1 oxide, and 6V/SBA-15 at 400 °C, and over P/oCNT at 380 °C.

rate constant	M1 (g^{-1} s^{-1})	6V/SBA-15 (g^{-1} s^{-1})	P/oCNT (g^{-1} s^{-1})
		Ethane	
k_1	0.643	0.00573	0.00149
k_{1a}	0.0104	0.000610	0.000156
k_{1b}	0.00599	0.000509	0.000103
k_2	0.0405	-	-
k_{2a}	0.0136	0.101	0.0138
k_{2b}	-	0.0413	0.0899
k_{3a}	4.18	-	-
k_{3b}	3.00	-	-
		Propane	
k_1	0.464	0.0529	0.0121
k_{1a}	0.00273	-	0.000491
k_{1b}	-	-	0.000528
k_2	4.89	0.00126	-
k_{2a}	2.15	0.802	0.142
k_{2b}	2.38	0.686	0.103
k_{2c}	0.0628	0.0544	-
k_{3a}	-	0.0101	-
k_{3b}	-	-	-
k_{4a}	-	-	-
k_{4b}	-	-	-

Table S 3-3 Normalized rate constants of Table S 3-2 for the oxidative dehydrogenation of ethane and propane based on the models presented in Scheme 3-2.

rate constant	M1	6V/SBA-15	P/oCNT
		ethane	
k_1	1.00	1.00	1.00
k_{1a}	0.0161	0.106	0.104
k_{1b}	0.00932	0,0889	0.0687
k_2	0.0630	-	-
k_{2a}	0.0212	17.6	9.28
k_{2b}	-	7.21	60.3
k_{3a}	6.50	-	-
k_{3b}	4.67	-	-
		propane	
k_1	1.00	1.00	1.00
k_{1a}	0.00587	-	0.0408
k_{1b}	-	-	0.0438
k_2	10.5	0.0239	-
k_{2a}	4.62	15.2	11.8
k_{2b}	5.13	13.0	8.55
k_{2c}	0.135	1.03	-
k_{3a}	-	0.190	-
k_{3b}	-	-	-
k_{4a}	-	-	-
k_{4b}	-	-	-

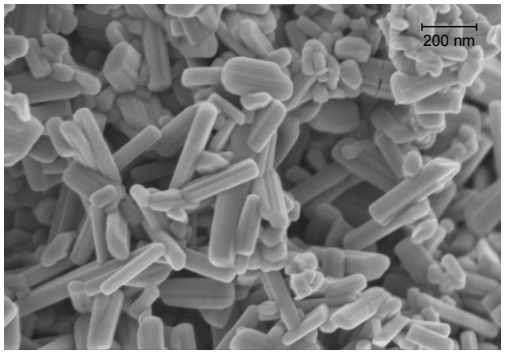

Figure S 3-1 SEM image of the MoVTeNb M1 oxide catalyst.

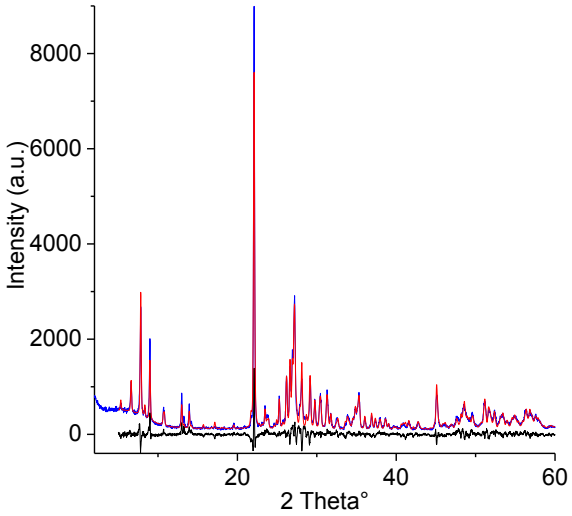

Figure S 3-2 Experimental powder XRD patterns of the MoVTeNb M1 oxide catalyst and result of the Rietveld refinement (experiment in blue, simulation in red, difference calculated-experimental in black).

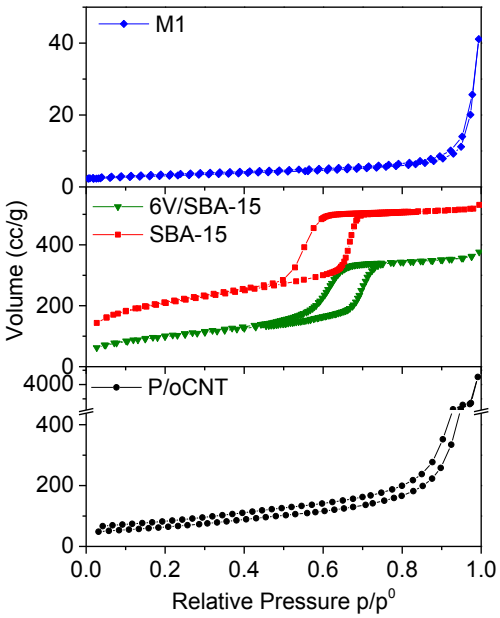

Figure S 3-3 Adsorption isotherms of nitrogen at T = 77 °C for M1, 6V/SBA-15, SBA-15, and P/oCNT.

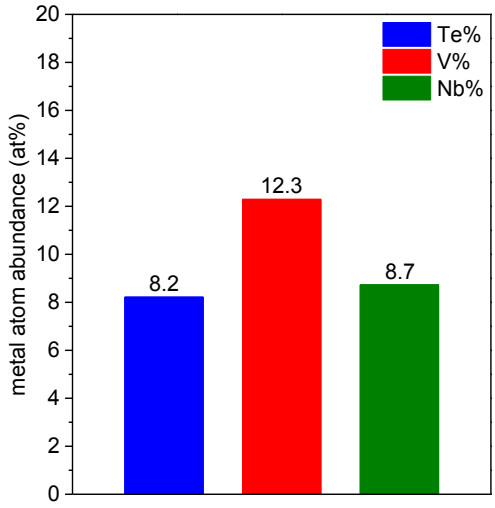

Figure S 3-4 Metal concentration of tellurium, vanadium, and niobium in at% on the surface of M1 (0.6 nm inelastic mean free path (IMFP)) determined by photoelectron spectroscopy at T = 400 °C, p = 0.25 mbar, feed C_3H_8/O_2 = 2:1.

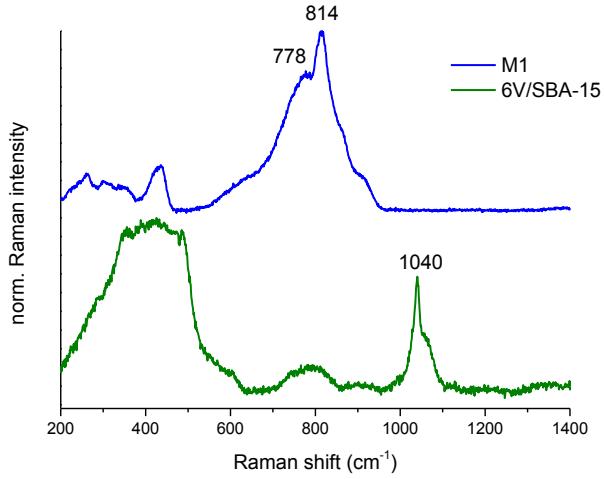

Figure S 3-5 Raman spectra of MoVTeNb M1 oxide (top), and 6V/SBA-15 (bottom) under reaction conditions of oxidative dehydrogenation of propane (T = 380 °C, feed C_3H_8/O_2/He = 10/5/85). The absence of vibrational modes of V_2O_5 nano-crystals at 141, 282, 302, 407, 482, 527, 698 and 995 cm^{-1},[39] confirms high vanadium oxide dispersion.

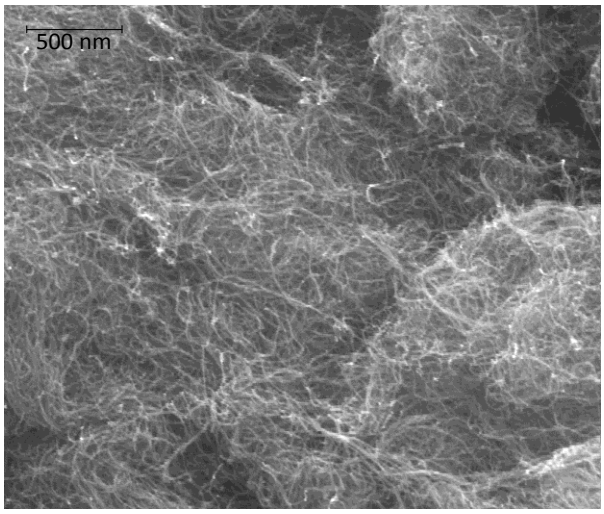

Figure S 3-6 SEM image of P/oCNT.

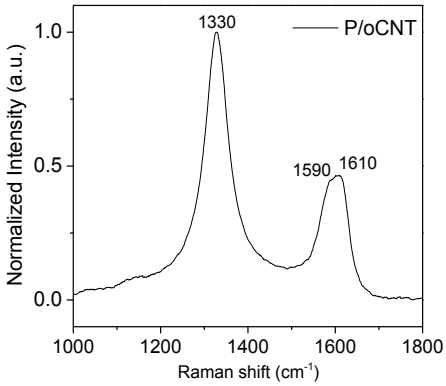

Figure S 3-7 Raman spectrum of P/oCNT (excitation wavelength 632.8 nm and a laser power 20 mW).

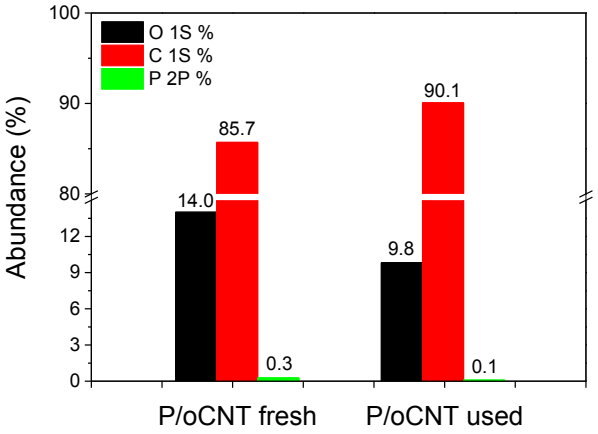

Figure S 3-8 Surface abundance of oxygen, carbon and phosphorous determined by X-ray photoelectron spectroscopy for fresh and used P/oCNT.

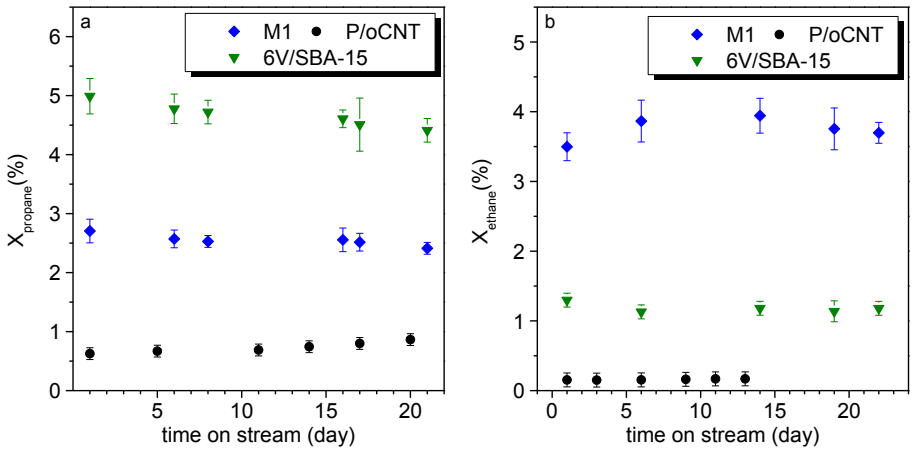

Figure S 3-9 Conversion of a) propane at T = 400 °C (M1 and 6V/SBA-15) and 360 °C (P/oCNT), feed $C_3H_8/O_2/He$ = 10/5/85, W/F = 0.072 g s ml^{-1} (M1), 1.34 g s ml^{-1} (6V/SBA-15) and 2.0 g s ml^{-1} (P/oCNT), and b) ethane at T = 400 °C (M1 and 6V/SBA-15) and 360 °C (P/oCNT), feed $C_2H_6/O_2/He$ = 10/5/85, W/F = 0.06 g s ml^{-1} (M1), 2.4 g s ml^{-1} (6V/SBA-15) and 2.0 g s ml^{-1} (P/oCNT) with time on stream.

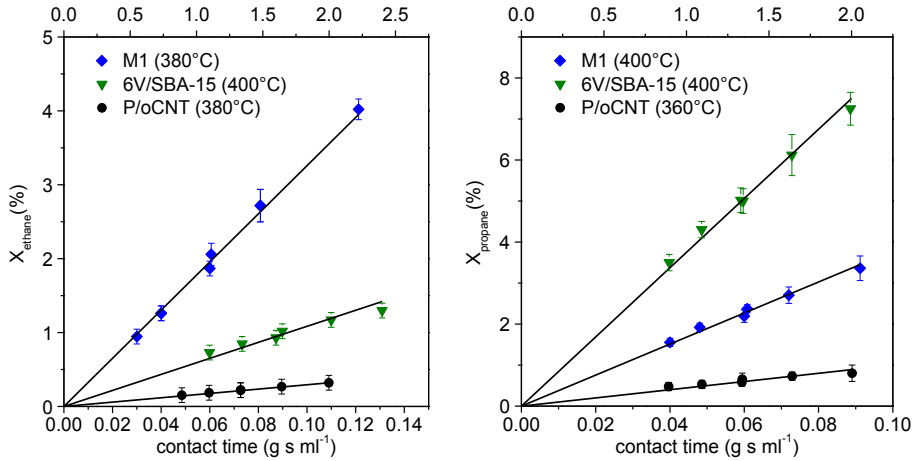

Figure S 3-10 Conversion of ethane (left) and propane (right) as a function of contact time; Feed $C_nH_{2n+2}/O_2/He$ = 10/5/85, W/F = 0.03 – 0.12 g s ml^{-1} (M1) and 0.9 – 2.4 g s ml^{-1} (6V/SBA-15 and P/oCNT). Test for mass transport limitation was performed by changing catalyst mass and total gas flow at the same time to keep the contact time constant (M1 = 0.06 g s ml^{-1} for ODE and ODP; 6V/SBA15 = 1.6 g s ml^{-1} for ODE and 1.3 g s ml^{-1} for ODP, P/oCNT = 1.3 g s ml^{-1} for ODE and ODP).

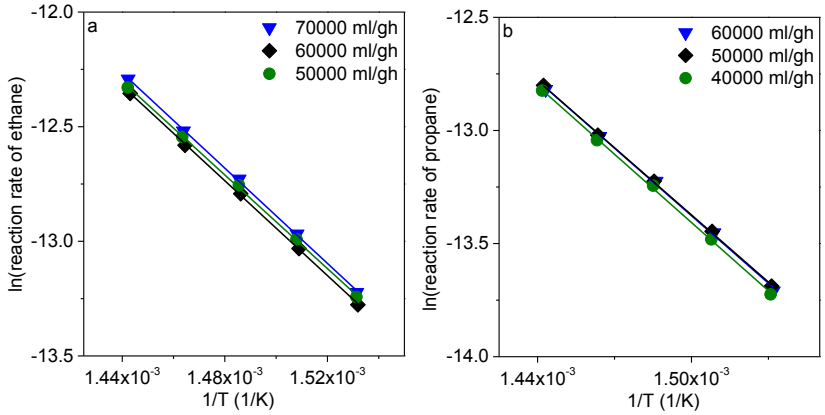

Figure S 3-11 Arrhenius plot for the determination of the apparent activation energy for ethane (a) and propane (b) over MoVTeNb M1 oxide.

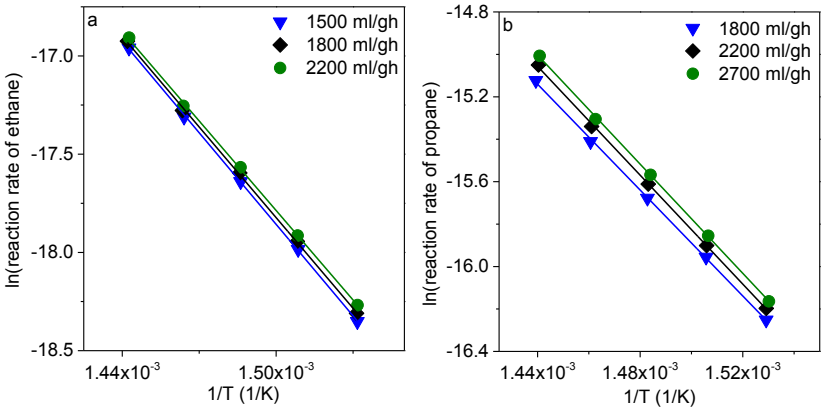

Figure S 3-12 Arrhenius plot for the determination of the apparent activation energy for ethane (a) and propane (b) over 6V/SBA15.

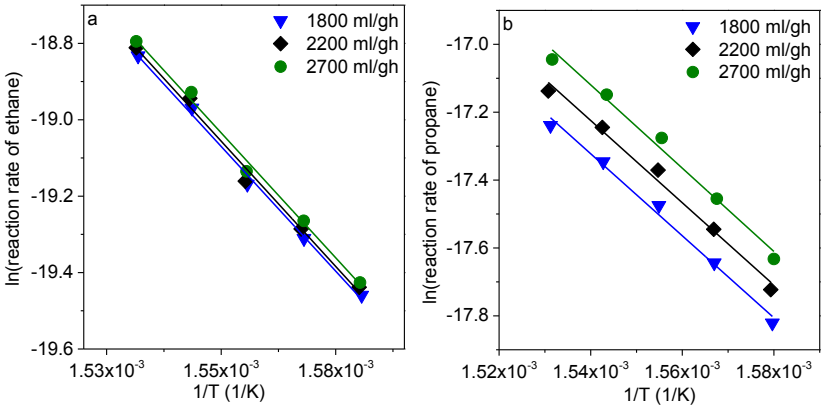

Figure S 3-13 Arrhenius plot for the determination of the apparent activation energy for ethane (a) and propane (b) over P/oCNT.

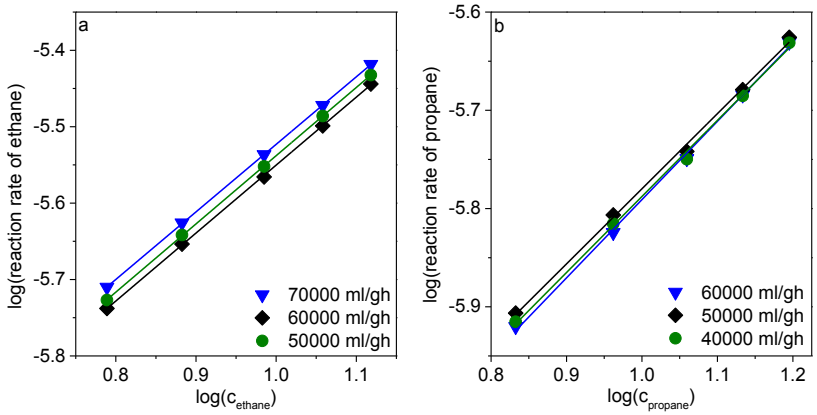

Figure S 3-14 Plot for the determination of the hydrocarbon reaction order for ethane (a) and propane (b) based on hydrocarbon consumption over MoVTeNb M1 oxide.

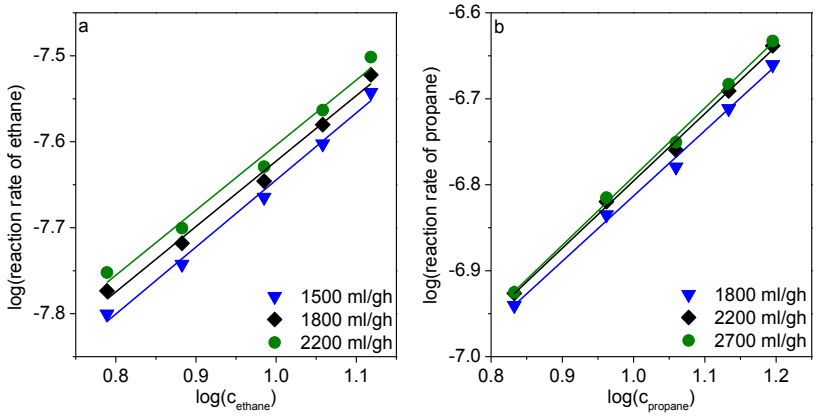

Figure S 3-15 Plot for the determination of the hydrocarbon reaction order for ethane (a) and propane (b) based on hydrocarbon consumption over 6V/SBA-15.

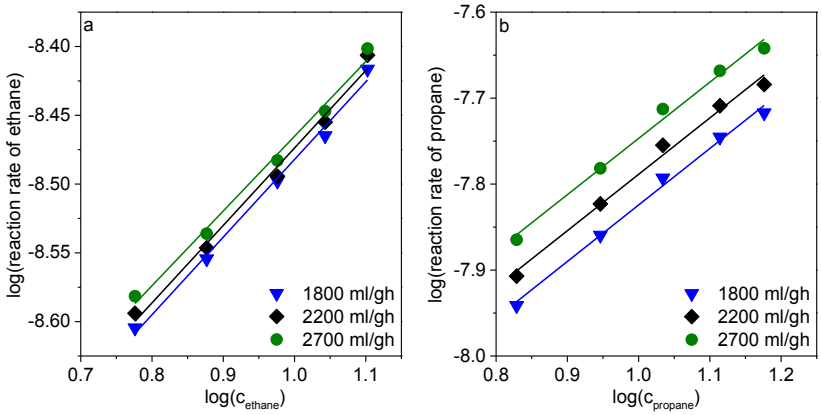

Figure S 3-16 Plot for the determination of the hydrocarbon reaction order for ethane (a) and propane (b) based on hydrocarbon consumption over P/oCNT.

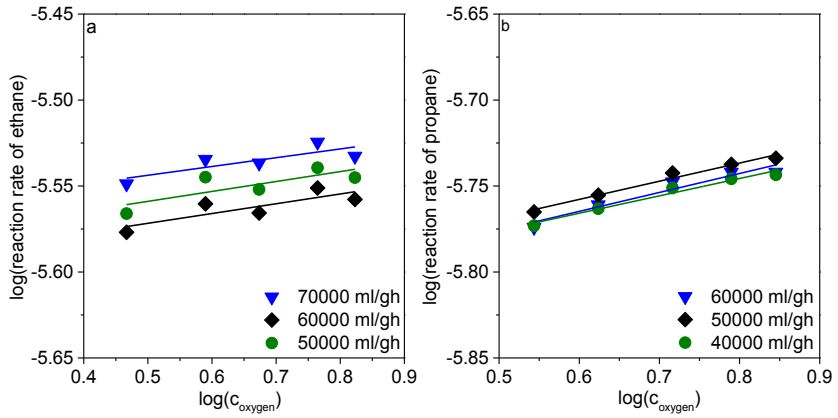

Figure S 3-17 Plot for the determination of the oxygen reaction order for ethane (a) and propane (b) based on hydrocarbon consumption over MoVTeNb M1 oxide.

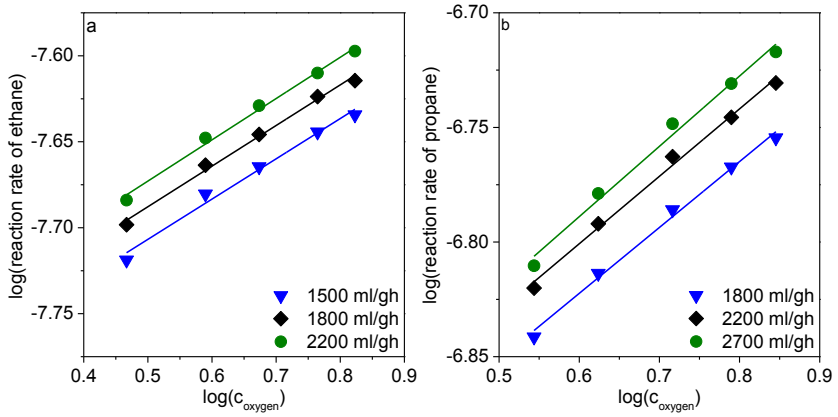

Figure S 3-18 Plot for the determination of the oxygen reaction order for ethane (a) and propane (b) based on hydrocarbon consumption over 6V/SBA-15.

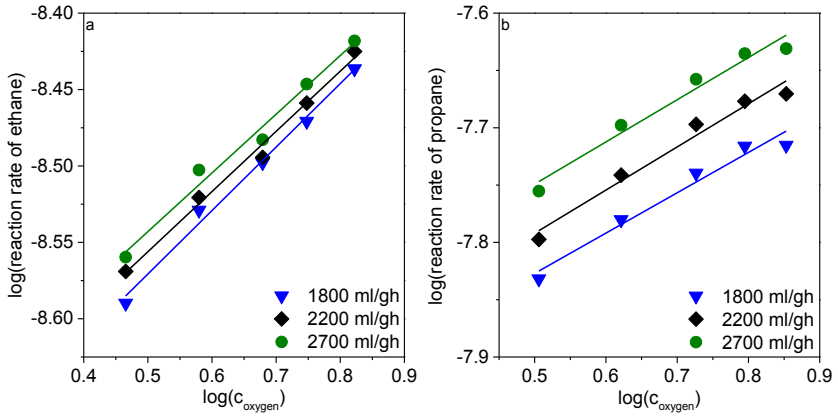

Figure S 3-19 Plot for the determination of the oxygen reaction order for ethane (a) and propane (b) based on hydrocarbon consumption over P/oCNT.

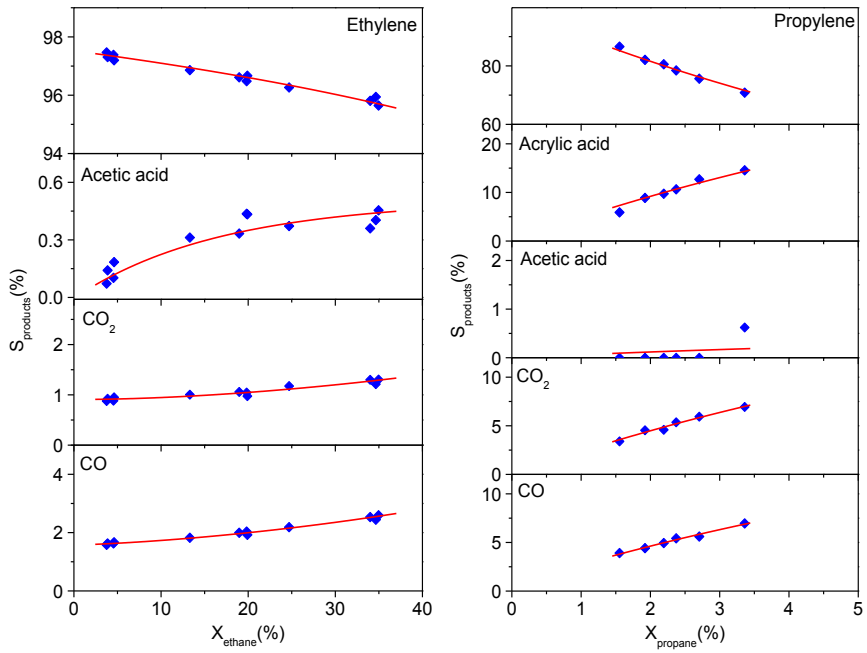

Figure S 3-20 Selectivity as a function of alkane conversion over MoVTeNb M1 oxide (blue points: experimental data; red curves: result of simulation); Left panel, oxidative dehydrogenation of ethane: T = 400 °C, feed $C_2H_6/O_2/He$ = 10/5/85, W/F = 0.075 – 0.3654 g s ml^{-1}; Right panel: oxidative dehydrogenation of propane: T = 400 °C, feed $C_3H_8/O_2/He$ = 10/5/85, W/F = 0.04 – 0.0912 g s ml^{-1}.

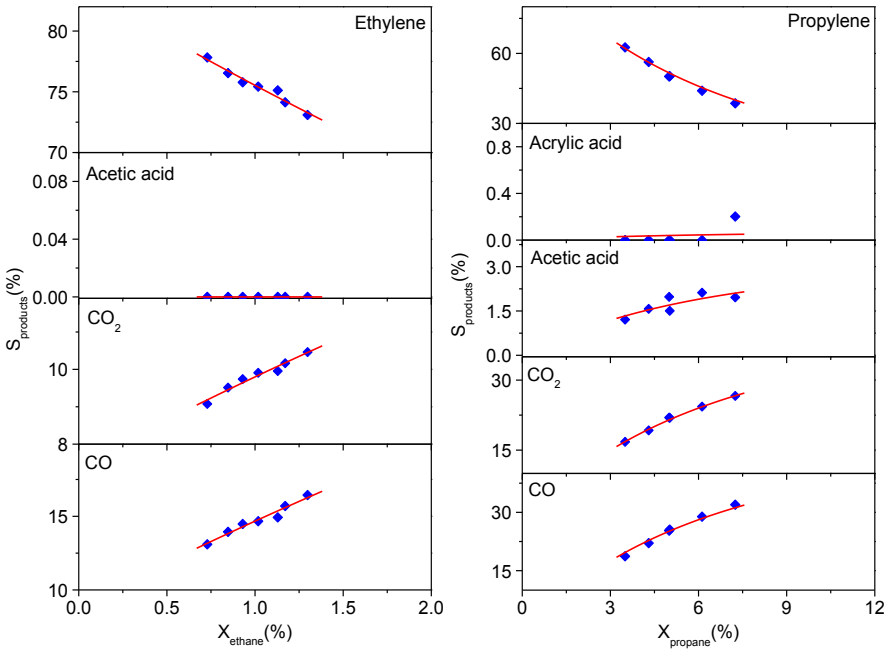

Figure S 3-21 Selectivity as a function of alkane conversion over 6V/SBA-15 (blue points: experimental data; red curves: result of simulation); Left panel, oxidative dehydrogenation of ethane: T = 400 °C, feed

$C_2H_6/O_2/He$ = 10/5/85, W/F = 1.098 – 2.3994 g s ml^{-1}; Right panel: oxidative dehydrogenation of propane: T = 400 °C, feed $C_3H_8/O_2/He$ = 10/5/85, W/F = 0.8956 – 1.9932 g s ml^{-1}.

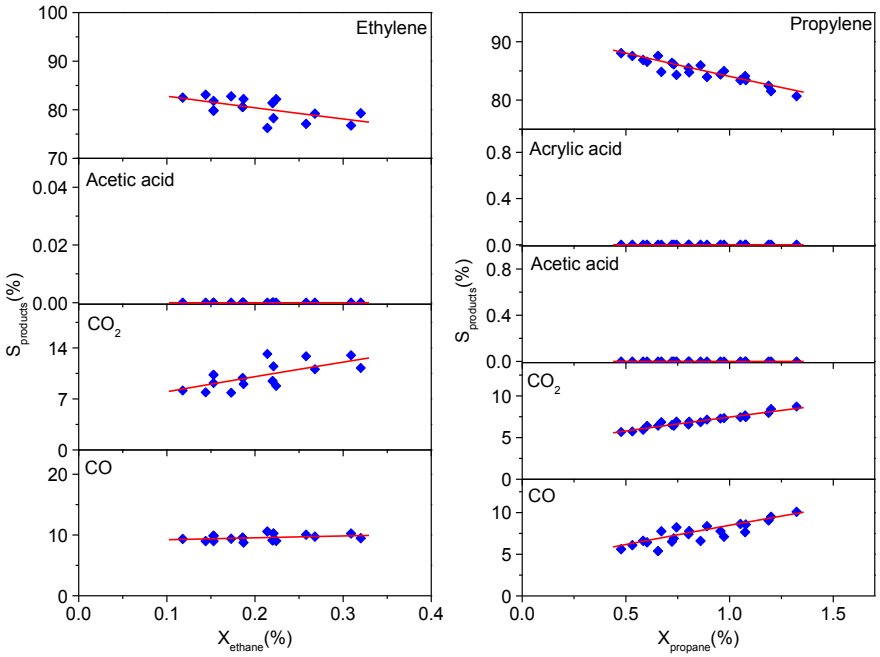

Figure S 3-22 Selectivity as a function of alkane conversion over P/o-CNT (blue points: experimental data; red curves: result of simulation); Left panel, oxidative dehydrogenation of ethane: T = 380 °C, feed $C_2H_6/O_2/He$ = 10/5/85, W/F = 0.6669 – 1.998 g s ml^{-1}; Right panel: oxidative dehydrogenation of propane: T = 360 – 380°C, feed $C_3H_8/O_2/He$ = 10/5/85, W/F = 0.892 – 2.0034 g s ml^{-1}.

3.6 References

[1] a) F. Cavani, N. Ballarini, A. Cericola, *Catalysis Today* **2007**, *127*, 113-131; b) F. Cavani, *Catalysis Today* **2010**, *157*, 8-15.

[2] R. Schlögl, *Topics in Catalysis* **2011**, *54*, 627-638.

[3] a) G. C. Bond, S. F. Tahir, *Applied Catalysis* **1991**, *71*, 1-31; b) E. A. Mamedov, V. Cortés Corberán, *Applied Catalysis A: General* **1995**, *127*, 1-40; c) T. Blasco, J. M. López Nieto, *Applied Catalysis, A: General* **1997**, *157*, 117-142; d) B. M. Weckhuysen, D. E. Keller, *Catalysis Today* **2003**, *78*, 25-46; e) C. Hess, *ChemPhysChem* **2009**, *10*, 319-326; f) N. F. Dummer, J. K. Bartley, G. J. Hutchings, in *Advances in Catalysis* **2011**, *Vol. 54* (Eds.: B. C. Gates, H. Knözinger), Elsevier Academic Press Inc, San Diego, **2011**, p. 189-247; g) I. E. Wachs, *Dalton Transactions* **2013**, *42*, 11762-11769; h) A. Trunschke, in *Nanostructured Catalysts: Selective Oxidation Reactions*, 1 ed. (Eds.: C. Hess, R. Schlögl), RSC Nanoscience & Nanotechnology, Cambridge, **2011**, pp. 56-95; i) W. Ueda, D. Vitry, T. Katou, *Catalysis Today* **2005**, *99*, 43-49; j) H. Launay, S. Loridant, D. L. Nguyen, A. M. Volodin, J. L. Dubois, J.-M. M. Millet, *Catalysis Today* **2007**, *128*, 176-182; k) A. Chieregato, J. M. López Nieto, F. Cavani, *Coordination Chemistry Reviews* **2015**, *301–302*, 3-23.

[4] a) P. DeSanto, Jr., D. J. Buttrey, R. K. Grasselli, C. G. Lugmair, A. F. Volpe, Jr., B. H. Toby, T. Vogt, *Zeitschrift für Kristallographie* **2004**, *219*, 152-165; b) X. Li, D. Buttrey, D. Blom, T. Vogt, *Topics in Catalysis* **2011**, *54*, 614-626.

[5] a) D. Vitry, Y. Morikawa, J. L. Dubois, W. Ueda, *Topics in Catalysis* **2003**, *23*, 47-53; b) R. Naumann D'Alnoncourt, L.-I. Csepei, M. Hävecker, F. Girgsdies, M. E. Schuster, R. Schlögl, A. Trunschke, *Journal of Catalysis* **2014**, *311*, 369-385.

[6] M. Hävecker, S. Wrabetz, J. Kröhnert, L.-I. Csepei, R. Naumann d'Alnoncourt, Y. V. Kolen'ko, F. Girgsdies, R. Schlögl, A. Trunschke, *Journal of Catalysis* **2012**, *285*, 48-60.

[7] a) P. Gruene, T. Wolfram, K. Pelzer, R. Schlögl, A. Trunschke, *Catalysis Today* **2010**, *157*, 137-142; b) M. D. Argyle, K. Chen, A. T. Bell, E. Iglesia, *Journal of Catalysis* **2002**, *208*, 139-149.

[8] a) J. Zhang, X. Liu, R. Blume, A. Zhang, R. Schlögl, D. S. Su, *Science* **2008**, *322*, 73-77; b) D. S. Su , J. Zhang, B. Frank, A. Thomas, X. Wang, J. Paraknowitsch, R. Schlögl, *ChemSusChem* **2010**, *3*, 169-180.

[9] T. T. Nguyen, M. Aouine, J. M. M. Millet, *Catalysis Communications* **2012**, *21*, 22-26.

[10] J. Le Bars, J. C. Vedrine, A. Auroux, S. Trautmann, M. Baerns, *Applied Catalysis A: General* **1992**, *88*, 179-195.

[11] B. Solsona, T. Blasco, J. M. López Nieto, M. L. Pena, F. Rey, A. Vidal-Moya, *Journal of Catalysis* **2001**, *203*, 443-452.

[12] B. Frank, M. Morassutto, R. Schomäcker, R. Schlögl, D. S. Su, *ChemCatChem* **2010**, *2*, 644-648.

[13] R. Naumann d'Alnoncourt, Y. V. Kolen'ko, R. Schlögl, A. Trunschke, *Combinatorial Chemistry and High Throughput Screening* **2012**, *15*, 161-169.

[14] Y.-M. Liu, Y. Cao, N. Yi, W.-L. Feng, W.-L. Dai, S.-R. Yan, H.-Y. He, K.-N. Fan, *Journal of Catalysis* **2004**, *224*, 417-428.

[15] A. Dinse, S. Khennache, B. Frank, C. Hess, R. Herbert, S. Wrabetz, R. Schlögl, R. Schomäcker, *Journal of Molecular Catalysis A: Chemical* **2009**, *307*, 43-50.

[16] O. V. Buyevskaya, A. Brückner, E. V. Kondratenko, D. Wolf, M. Baerns, *Catalysis Today* **2001**, *67*, 369-378.

[17] M. L. Pena, A. Dejoz, V. Fornes, F. Rey, M. I. Vazquez, J. M. López Nieto, *Applied Catalysis, A: General* **2001**, *209*, 155-164.

[18] B. Frank, J. Zhang, R. Blume, R. Schlögl, D. S. Su, *Angewandte Chemie International Edition* **2009**, *48*, 6913-6917.

[19] A. Sadezky, H. Muckenhuber, H. Grothe, R. Niessner, U. Pöschl, *Carbon* **2005**, *43*, 1731-1742.

[20] B. Frank, A. Rinaldi, R. Blume, R. Schlögl, D. S. Su, *Chemistry of Materials* **2010**, *22*, 4462-4470.

[21] B. Frank, R. Blume, A. Rinaldi, A. Trunschke, R. Schlögl, *Angewandte Chemie International Edition* **2011**, *50*, 10226-10230.

[22] a) K. Chen, A. T. Bell, E. Iglesia, *The Journal of Physical Chemistry B* **2000**, *104*, 1292-1299; b) E. Heracleous, M. Machli, A. A. Lemonidou, I. A. Vasalos, *Journal of Molecular Catalysis A: Chemical* **2005**, *232*, 29-39; c) P. Viparelli, P. Ciambelli, L. Lisi, G. Ruoppolo, G. Russo, J. C. Volta, *Applied Catalysis A: General* **1999**, *184*, 291-301; d) C. S. Guo, K. Hermann, M. Hävecker, J. P. Thielemann, P. Kube, L. J. Gregoriades, A. Trunschke, J. Sauer, R. Schlögl, *The Journal of Physical Chemistry C* **2011**, *115*, 15449-15458; e) K. Amakawa, L. Sun, C. Guo, M. Hävecker, P. Kube, I. E. Wachs, S. Lwin, A. I. Frenkel, A. Patlolla, K. Hermann, R. Schlögl, A. Trunschke, *Angewandte Chemie International Edition* **2013**, *52*, 13553-13557.

[23] O. V. Khavryuchenko, B. Frank, A. Trunschke, K. Hermann, R. Schlögl, *The Journal of Physical Chemistry C* **2013**, *117*, 6225-6234.

[24] K. Amakawa, Y. V. Kolen'ko, A. Villa, M. E. Schuster, L.-I. Csepei, G. Weinberg, S. Wrabetz, R. Naumann d'Alnoncourt, F. Girgsdies, L. Prati, R. Schlögl, A. Trunschke, *ACS Catalysis* **2013**, *3*, 1103-1113.

[25] J. Kubo, N. Watanabe, W. Ueda, *Chemical Engineering Science* **2008**, *63*, 1648-1653.

[26] R. Grabowski, J. Słoczyński, *Chemical Engineering and Processing: Process Intensification* **2005**, *44*, 1082-1093.

[27] R. Quintana-Solórzano, G. Barragán-Rodríguez, H. Armendáriz-Herrera, J. M. López-Nieto, J. S. Valente, *Fuel* **2014**, *138*, 15-26.

[28] a) C. Heine, M. Hävecker, M. Sanchez-Sanchez, A. Trunschke, R. Schlögl, M. Eichelbaum, *The Journal of Physical Chemistry C* **2013**, *117*, 26988-26997; b) J.-M. M. Millet, *Topics in Catalysis* **2006**, *38*, 83-92.

[29] a) V. Sanchez Escribano, G. Busca, V. Lorenzelli, *The Journal of Physical Chemistry* **1990**, *94*, 8939-8945; b) M. McEntee, W. Tang, M. Neurock, J. T. Yates, *Journal of the American Chemical Society* **2014**, *136*, 5116-5120; c) P. G. Harrison, B. Maunders, *Journal of the Chemical Society, Faraday Transactions 1: Physical Chemistry in Condensed Phases* **1985**, *81*, 1345-1355; d) E. Finocchio, G. Busca, V. Lorenzelli, V. S. Escribano, *Journal of the Chemical Society, Faraday Transactions* **1996**, *92*, 1587-

1593; e) P. Concepción, P. Botella, J. M. López Nieto, *Applied Catalysis A: General* **2004**, *278*, 45-56; f) R. Coast, M. Pikus, P. N. Henriksen, G. A. Nitowski, *The Journal of Physical Chemistry* **1996**, *100*, 15011-15014.

[30] B. Frank, S. Wrabetz, O. V. Khavryuchenko, R. Blume, A. Trunschke, R. Schlögl, *ChemPhysChem* **2011**, *12*, 2709-2713.

[31] a) X. Rozanska, R. Fortrie, J. Sauer, *Journal of the American Chemical Society* **2014**, *136*, 7751-7761; b) X. Rozanska, R. Fortrie, J. Sauer, *The Journal of Physical Chemistry C* **2007**, *111*, 6041-6050.

[32] a) D. C. Tranca, N. Hansen, J. A. Swisher, B. Smit, F. J. Keil, *The Journal of Physical Chemistry C* **2012**, *116*, 23408-23417; b) E. J. Maginn, A. T. Bell, D. N. Theodorou, *The Journal of Physical Chemistry* **1995**, *99*, 2057-2079.

[33] C. Batiot, B. K. Hodnett, *Applied Catalysis A: General* **1996**, *137*, 179-191.

[34] M. Eichelbaum, M. Hävecker, C. Heine, A. M. Wernbacher, F. Rosowski, A. Trunschke, R. Schlögl, *Angewandte Chemie International Edition* **2015**, *54*, 2922-2926.

[35] D. Maganas, A. Trunschke, R. Schlögl, F. Neese, *Faraday Discussions*, **2016**, *188*, 181-197.

[36] Y. V. Kolen'ko, W. Zhang, R. Naumann d'Alnoncourt, F. Girgsdies, T. W. Hansen, T. Wolfram, R. Schlögl, A. Trunschke, *ChemCatChem* **2011**, *3*, 1597-1606.

[37] N. Hamilton, T. Wolfram, G. Tzolova Müller, M. Hävecker, J. Kröhnert, C. Carrero, R. Schomäcker, A. Trunschke, R. Schlögl, *Catalysis Science & Technology* **2012**, *2*, 1346-1359.

[38] H. Bluhm, M. Hävecker, A. Knop-Gericke, M. Kiskinova, R. Schlögl, M. Salmeron, *MRS Bulletin* **2007**, *32*, 1022-1030.

[39] J. J. Yeh, I. Lindau, *Atomic Data and Nuclear Data Tables* **1985**, *32*, 1-155.

Chapter 4 Isotope Studies in Oxidation of Propane over Vanadium Oxide[**]

Abstract

The oxidation of propane has been studied over silica-supported vanadium oxide and polycrystalline, bulk MoVTeNb oxide with M1 structure. Temperature-programmed reaction experiments were performed, and the reactivity of propane molecules labeled with deuterium and ^{13}C, respectively, was analyzed under steady-state conditions. The measurement of kinetic isotope effects reveals fundamental differences in the activation of propane over the two catalysts. The reaction network of consecutive and parallel reactions of the formed propylene is comparable. However, oxygen insertion into the CHO group of acrolein under formation of acrylic acid is faster over M1 than oxidation at the CH_2 group and decarbonylation to acetaldehyde. In contrast, the latter process is preferred over silica-supported vanadium oxide resulting in lower selectivity to unsaturated oxygenates.

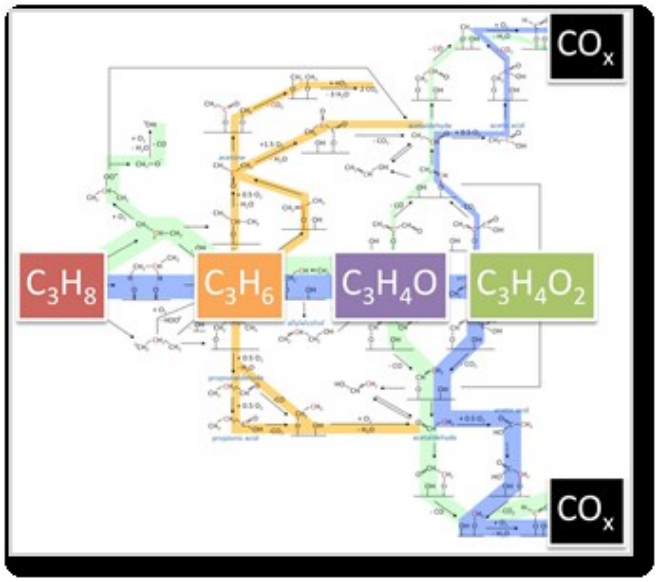

[**]Reproduced from the publication

P. Kube, B. Frank, R. Schlögl, A. Trunschke "Isotope Studies in Oxidation of Propane over Vanadium Oxide" *ChemCatChem* **2017**, *9*, 3446-3455, https://doi.org/10.1002/cctc.201700847, with permission from John Wiley and Sons.

4.1 Introduction

The activation of C-H bonds in small alkane molecules has been widely investigated in chemistry in general and specifically in heterogeneous catalysis with the intent to use the large natural gas reserves of our planet economically in the synthesis of chemicals.[1] Theoretical and kinetic studies of selective oxidation and oxidative dehydrogenation of alkanes with molecular oxygen over metal oxide catalysts disclosed an intricate network of parallel and consecutive reactions that limits the selectivity towards desired olefins or unsaturated oxygenates.[2] In kinetic studies of oxidative dehydrogenation (ODH) of propane over supported vanadium oxide catalysts the reaction network is, however, usually condensed and presented as a triangle (Scheme 4-1, black symbols and lines).[3] Albeit in traces, oxygenates have been detected in the gas phase, revealing that a more complex underlying network (Scheme 4-1, blue symbols) has implications on the selectivity towards the main products propylene, CO, and CO_2.[4] The selectivity to propylene is highly dependent on catalyst composition (nature of support, promoters and modifiers, vanadium oxide loading), catalyst structure (molecular structure of vanadium oxide surface species, degree of oligomerization, degree of hydroxylation, texture of catalyst or support) and reaction conditions (partial pressures, temperature, steam content).[5] Detailed knowledge of the reaction network and its dependence on catalyst structure is the key to control selectivity. But so far, research was mainly focused on the first supposedly rate determining step (RDS) that comprises hydrogen abstraction under formation of a propyl radical (Scheme 4-1, red) and a hydroxyl group. Analyses of kinetic isotope effects (KIE) over supported vanadium oxide revealed that hydrogen in methylene position is abstracted first affecting the rate of the overall reaction.[6] Consequently, the barrier of the first step controls activity, although quantum chemical calculations of the (010) surface of V_2O_5 indicated that subsequent steps such as the regeneration of the active site by dehydroxylation might exhibit high barriers as well.[7]

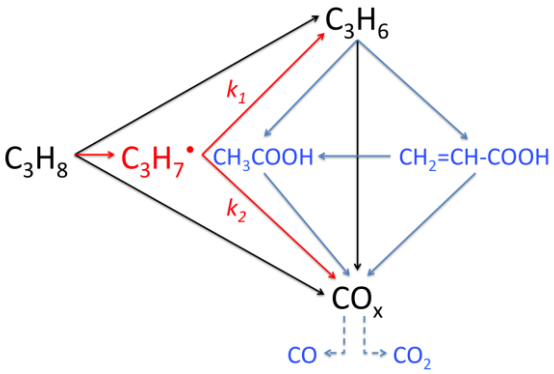

Scheme 4-1 Simplified reaction network in oxidative dehydrogenation of propane over vanadium oxide catalysts (black symbols) and minimum extension based on detected gas phase intermediates[4,8] (blue symbols) and the supposed $C_3H_7^{\bullet}$ surface / gas phase intermediate (red).

In general, selectivity is affected by favouring specific pathways compared to others. High barriers in the multistep pathways to carbon dioxide, i.e., deceleration of the corresponding reaction(s), may then result in increased selectivity to propylene. Herein we investigate the reaction network in propane oxidation over bulk mixed MoVTeNb oxide (M1) and a silica-supported (mesoporous silica SBA-15) vanadium oxide monolayer model catalyst (6V/SBA-15) by temperature-programmed reaction and steady-state experiments using isotope labelled reactants. The reaction conditions are limited to fat, dry feed ($C_3H_8/O_2/He$ = 10/5/85) and low propane conversion. Under these reaction conditions the selectivity to undesired carbon oxides is higher over silica-supported vanadium oxide compared to M1.[4] Factors that determine selectivity in the oxidation of short-chain alkanes over vanadium oxide catalysts are discussed based on the comparative analysis of the reaction network over the two catalysts.

4.2 Results and Discussion

Oxidative dehydrogenation of propane was performed in temperature-programmed experiments by increasing the temperature stepwise (Figure 4-1). Each individual data point presented in Figure 4-1a-b is the average of 3-5 measurement points in steady state at the corresponding reaction temperature. Steady state confirms that the corresponding products are formed catalytically. The reaction products in the gas phase were analysed by gas chromatography. Conversion and selectivity as a function of temperature are

shown in Figure S 4-1. A multitude of products was observed over both catalysts. The types of products are the same over M1 and 6V/SBA-15, with the exception of propionic acid that was only detected over 6V/SBA-15. However, the relative concentrations and the temperatures, at which the individual products appear first, differ.

Propylene is the first product detectable over both catalysts at a temperature as low as 120 °C. The low temperature clearly indicates that C-H activation is not the major problem on vanadium oxide catalysts. At higher temperature (160 – 180 °C) acetone appears as second product, whereas the concentration of propylene and acetone is higher over M1 compared to 6V/SBA-15. It is not possible to conclude from the present experiments whether acetone and propylene are formed via the same iso-propoxide surface intermediate or whether iso-propoxide as probable precursor of acetone is formed after re-adsorption of propylene. It has to be noted at this point that the sensitivity of the thermal conductivity detector (TCD) used for analysis of the carbon oxides is lower compared to the sensitivity of the flame ionization detector (FID) applied for analysis of hydrocarbons and oxygenates. Consequently, the fact that no carbon oxides are observed below 200 °C when acetone is already formed does not necessarily mean that acetone is no precursor for CO_2,[9] because CO_2 is only detectable at a minimum concentration of 1 ppm. On the other hand, it has been shown that acetone is quite stable under oxidizing conditions over MoVTeNb oxide.[8] CO_2 is detected first over M1 at 250 °C. In contrast, CO_2 appears on 6V/SBA-15 with a temperature offset of only 20 K with respect to acetone already at 200 °C and might consequently stem more likely from total oxidation of acetone as well.

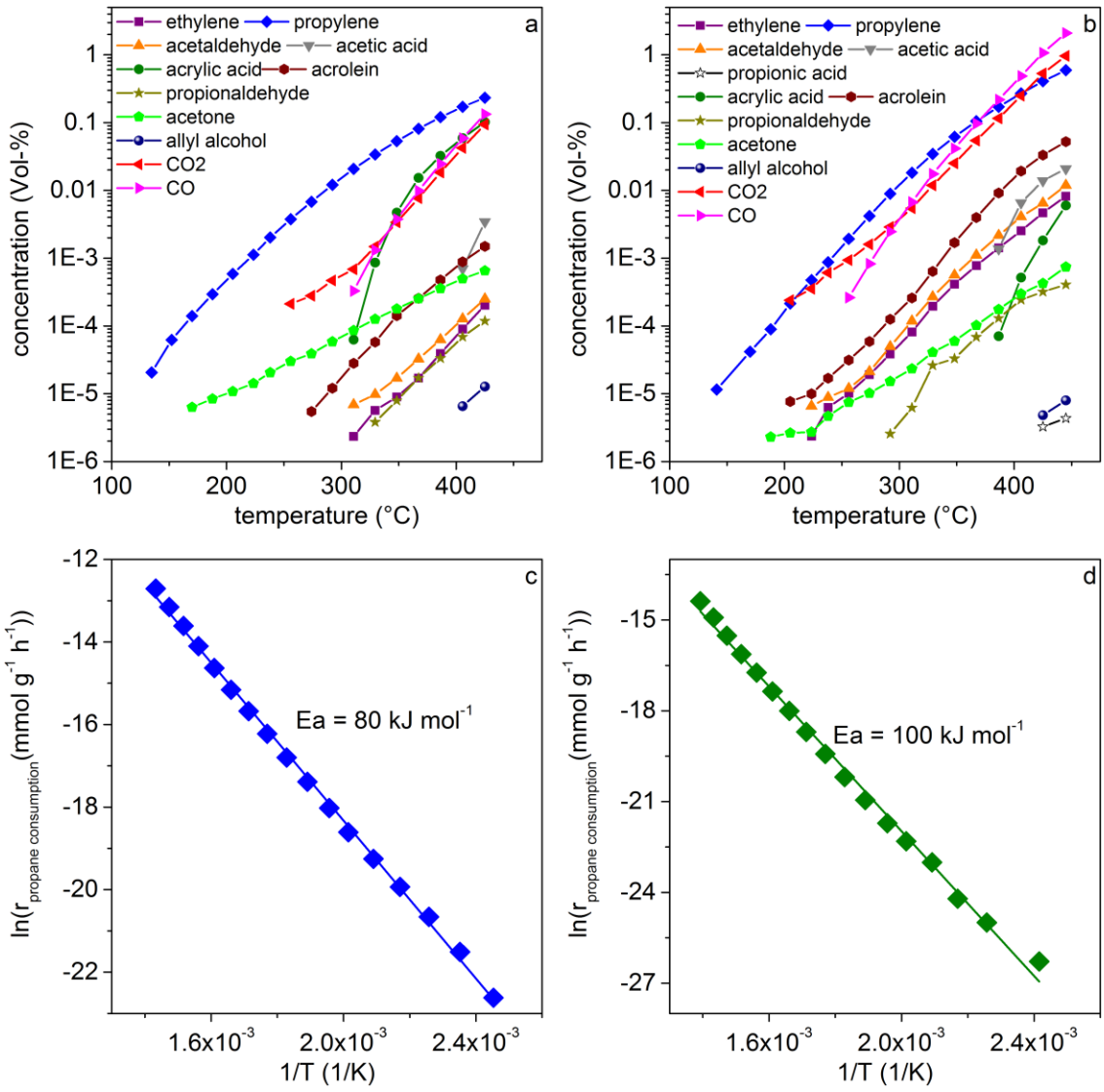

Figure 4-1 Temperature-programmed oxidation of propane (heating rate 1 °C min^{-1}, measurement isothermal every 20 K) over a) M1 (C_3H_8/O_2/He = 10/5/85, W/F = 0.06 g s ml^{-1}, m_{cat} = 10 mg, F_{total} = 10 ml min^{-1}), and b) 6V/SBA-15 (C_3H_8/O_2/He = 10/5/85, W/F = 1.33 g s ml^{-1}, m_{cat} = 222 mg, F_{total} = 10 ml min^{-1}); Arrhenius plots measured over M1 (c) and 6V/SBA-15 (d) taking into account the overall rate of propane consumption calculated based on sum of the reaction products.

The primary formation of carbon oxides (without desorption of reaction intermediates) cannot be excluded based on the present experiments. Indication for the latter process has been found on M1,[8] and supported vanadium oxide catalysts.[10] Here, the propylene selectivity increases with increasing vanadia loading, which has been attributed to

coverage of unselective support sites,[10] or to the higher activity,[10b] and/or a modified reducibility[10a] of supported polyvanadate species.

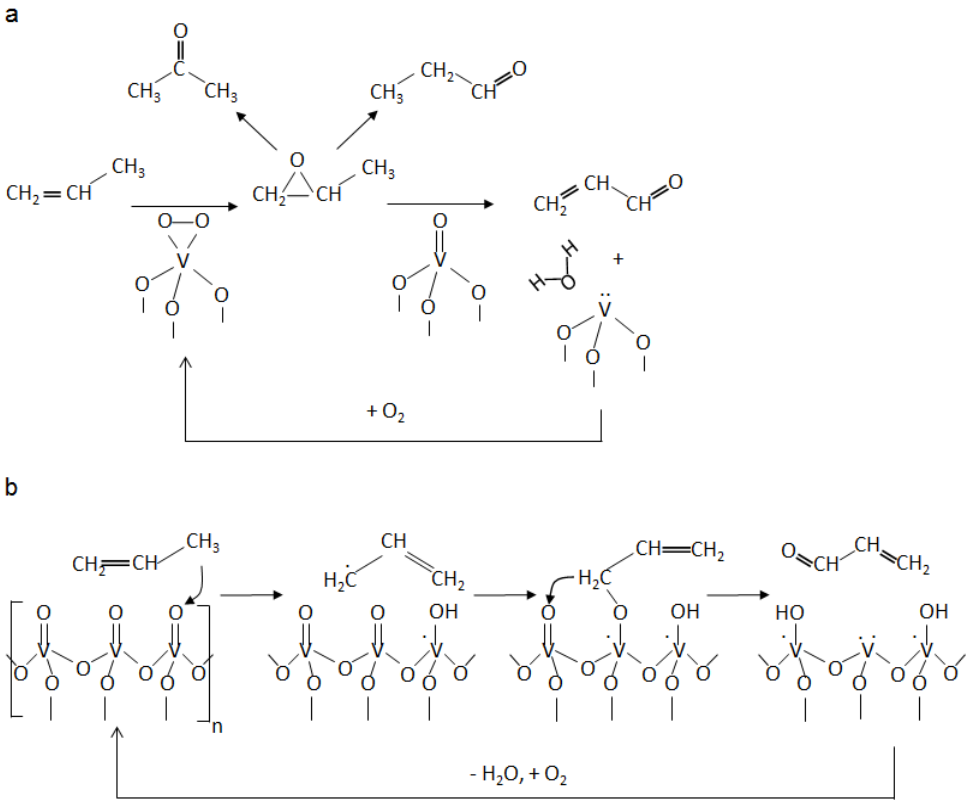

Scheme 4-2 Low-temperature (a) and high-temperature (b) formation of acrolein, acetone and propionaldehyde; Low-temperature oxidation via propylene oxide occurs mainly on silica-supported vanadium oxide; High-temperature allylic oxidation occurs on both M1 and silica-supported vanadium oxide and requires at least V_xO_y trimers.

Acrolein also starts to form already at 200 °C over 6V/SBA-15. Acrolein formation occurs here together with CO_2 and with a temperature offset of + 20 K with respect to acetone. Propylene oxide has been proposed as a common intermediate in the formation of acrolein and acetone in density functional calculations applying silsesquioxane models,[2i] considering either isolated vanadyl surface groups or peroxovanadate species as active sites. Although propylene oxide has not been detected in the gas phase in the present experiment, the nearly simultaneous appearance of acetone and acrolein over 6V/SBA-15 is not in contradiction with such pathways. In contrast, over M1 the two products arise at very different temperatures. While acetone appears first at 160 °C on

M1, acrolein is observed only at 270 °C with an offset of + 70 K compared to 6V/SBA-15. The slope of the acrolein formation curve measured for 6V/SBA-15 changes in the temperature range in which acrolein formation sets in over M1. It might be, therefore, possible that different mechanisms contribute to acrolein formation over 6V/SBA-15, such as a low-temperature (200 – 300 °C) oxidation pathway catalysed by activated oxygen species at the surface, such as peroxovanadate, via propylene oxide as intermediate followed by oxidative dehydrogenation (Scheme 4-2a), and the allylic oxidation of propylene at higher temperatures (> 300 °C) (Scheme 4-2b). In the low-temperature range acetone and propionaldehyde may be formed as isomerization products of propylene oxide.[11] Indications for the participation of peroxide species in oxidative dehydrogenation of propane over supported vanadium oxide catalysts have been found recently by experiment,[12] and theory.[13] Such a change in the shape of the acrolein formation curve is not observed over M1, which is in agreement with a low concentration of electrophilic oxygen species on the surface of M1 also at low temperatures resulting in the dominance of the allylic mechanism.[14]

It is interesting to note that the shapes of the CO_2 evolution curves observed over M1 and 6V/SBA-15, respectively, are very similar. The slopes of the curves change at 300 °C indicating that at higher temperatures additional processes contribute to CO_2 formation.

The next group of products comprises acetaldehyde, ethylene, and CO arising at 220 °C (with an offset for CO of + 20 K perhaps due to the detection limit of the TCD detector) over 6V/SBA-15 and at 300 °C over M1 revealing that also the disintegration of the carbon backbone occurs already at much lower temperature over 6V/SBA-15 compared to M1. Decomposition pathways are not directly retrievable from the present experiment. It is interesting to note that over M1 the appearance of acetaldehyde, ethylene and CO coincide with acrylic acid formation, whereas a temperature difference of about 200 K is observed over 6V/SBA-15 between first detection of these products and the formation of acrylic acid. The reason might be that acetaldehyde is a common intermediate that may be formed starting from acetone, acrolein,[15] as well as acrylic acid (Scheme 4-3, Scheme S 4-1). In particular, the decomposition pathways of acrolein to CO_x and acrylic acid to ethylene and CO_x may share a joint C2 surface intermediate (Scheme 4-3, Scheme S 4-1).

The shapes of the acrylic acid evolution curves (steep slope) are comparable over the two catalysts. Formation starts at 400 °C over 6V/SBA-15. The curve is shifted by 100 K to lower temperatures over M1 indicating that in contrast to other oxygenates formation of acrylic acid is particularly facilitated over M1.

Acetic acid occurs only above 400 °C over both catalysts and the curves progress in parallel to the acrylic acid formation curves confirming previous results that acetic acid might be formed by decomposition of acrylic acid.[8] But it cannot be excluded that acetic acid is also formed by oxidation of adsorbed C2 precursors formed in acrolein decomposition (Scheme 4-3, Scheme S 4-1). C2 and C3 precursors are then apparently oxidized to the corresponding acids in the same temperature range. Acetic acid could also be formed by oxidation of re-adsorbed ethylene, which is formed in C-C bond splitting reactions that occur already at lower temperatures (see ethylene evolution curves in Figure 4-1). However, this is less likely, since the slope of the ethylene evolution curves are not affected by the onset of acetic acid formation (Figure 4-1). Acrylic acid is either more slowly formed or faster decomposed to acetic acid over 6V/SBA-15 compared to M1, because over the former catalyst the concentration of acetic acid is higher than the concentration of acrylic acid whereas the reverse situation is observed over M1.

Remarkably, allyl alcohol, which is an intermediate of propylene allylic oxidation, is still detectable over both catalysts at temperatures above 400 °C when the molecule reaches sufficient high concentration in the gas phase revealing that allylic oxidation is a common pathway over both catalysts.

Finally, a pathway via adsorbed n-propoxide resulting in propionaldehyde (occurrence above 300 °C) and propionic acid (detectable only over 6V/SBA-15 above 400 °C) is operative over both catalysts as well. Formation of propionaldehyde at low temperature by isomerization of propylene oxide cannot be excluded.

The rate of overall propane consumption calculated based on the sum of products has been plotted as a function of 1/T (Figure 4-1c-d). The function is overall linear for both catalysts (R^2 = 0.9985 for M1, and R^2 = 0.9949 for 6V/SBA-15) indicating that significant changes in the reaction network do not occur in the studied temperature range at points where new products appear in the gas phase meaning that all detected products might belong to a single complex reaction network branching out from propane. Slight

deviation occurs at low temperatures over 6V/SBA-15 for the reasons discussed above (Scheme 4-2). The apparent activation energies (Figure 4-1c-d) agree well with published values for M1[4,8] and SBA-15-supported vanadium oxide,[16] respectively.

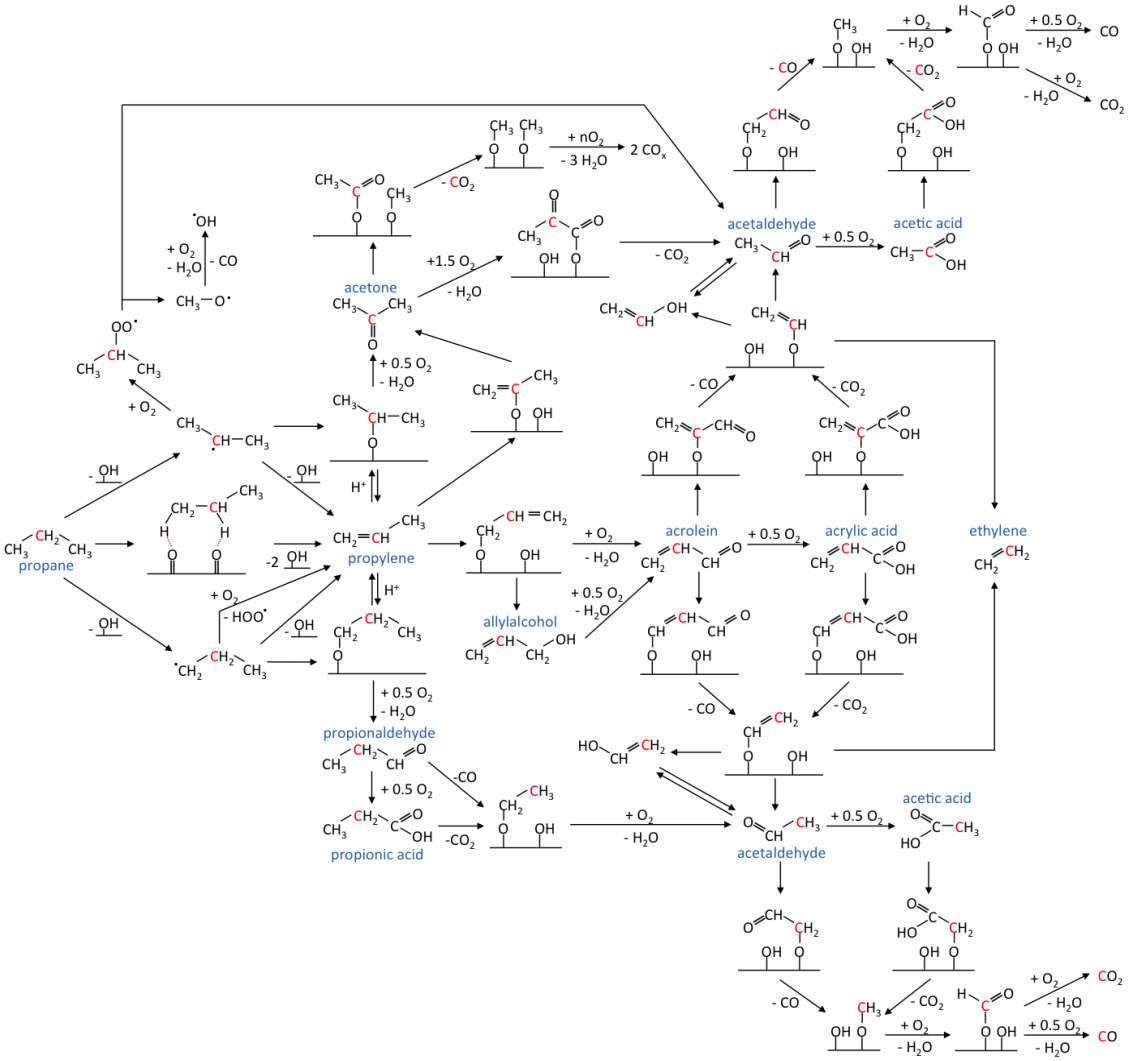

Scheme 4-3 Reaction network in propane oxidation outlined based on intermediate products detected in the gas phase (blue) over M1 and 6V/SBA-15 in dry feed ($C_3H_8/O_2/He$ = 10/5/85) in the temperature range 100 – 450 °C during temperature-programmed propane oxidation; Furthermore, the results of the experiments with D- and ^{13}C-labelled propane (the red colour indicates the ^{13}C-labelled carbon atom) have been integrated into the Scheme; A version of the Scheme that highlights major principal similarities and differences in the reaction networks over 6V/SBA-15 and M1 is presented in the Supporting Information (Scheme S 4-1).

In summary, the temperature-programmed experiments reveal that a multitude of reaction products (11 over M1 and 12 over 6V/SBA-15) are detectable by gas chromatography in the temperature range 100 – 450 °C and consequently involved in the reaction network of propane oxidation over both, M1 and 6V/SBA-15 catalysts. A hypothetical reaction network that includes all intermediates detected so far in the gas phase under the specific reaction conditions applied in the present experiments is presented in Scheme 4-3. The experimentally proven reaction intermediates are highlighted in blue. Surface intermediates have been proposed based on spectroscopic studies of selective and total oxidation catalysts.[17] The type of products detected and the shape of the product evolution curves are strikingly similar at normal reaction temperatures of propane oxidation (300 – 400 °C) suggesting that the same global reaction network predominates over the two catalyst systems, but the rate constants of individual reaction steps differ. However, at temperatures below 300 °C differences are observed in particular with respect to acrolein formation. Hydrogen-abstraction under formation of propylene occurs already at very low temperature over both catalysts followed by oxyhydration/oxidation to acetone or allylic oxidation to acrolein. Acrolein formation and cleavage of C-C bonds are reactions particularly favoured over 6V/SBA-15, while acrylic acid formation is favoured over M1.

Based on the assumption that the entire reaction network in propane oxidation over M1 and 6V/SBA-15 is similar, differences in the selectivity of the overall reaction result from differences in the activation energy of individual reaction steps. In the following, we have analysed kinetic isotope effects (KIE) based on rates of overall propane consumption and propylene formation. If the abstraction of the first hydrogen atom in adsorbed propane is rate limiting, the rate of propane consumption must be affected by deuteration. To verify whether hydrogen abstraction in methylene position is the rate-limiting step of the overall propane oxidation, propane consumption rates were measured using C_3H_8 and 2,2-$C_3D_2H_6$, respectively. Similarly, the impact of splitting a C-H bond in methyl position was studied comparing 2,2-$C_3D_2H_6$ and C_3D_8, respectively. Rates extrapolated to zero conversion determined in contact time variations at T = 400 °C (Figure S 4-2 and Figure S 4-3) have been used (Table 4-1) to calculate the KIE (Table 4-2).

In agreement with isotope studies of propane ODH over zirconia supported vanadium oxide catalysts,[6] the substitution of H by D in methylene position affects the overall consumption rate of the substrate over 6V/SBA-15 (Table 4-1) resulting in a significant KIE of 1.45 (Table 4-2) and revealing that C-H activation of methylene hydrogen in propane affects the propane consumption rate also over silica-supported vanadium oxide. Deuteration in methyl position has no effect resulting in a KIE of 1 again in agreement with the literature.

Table 4-1 Propane consumption rates, propylene formation rates, and selectivity to propylene over the two catalysts obtained in contact time variation experiments (W/F = 0.02 – 0.06 g s ml^{-1} for M1, and 0.30 – 1.34 g s ml^{-1} for 6V/SBA-15) in the feed $C_3H_8/O_2/He$ = 10/5/85 at T = 400 °C with different isotopes after extrapolation to zero propane conversion (raw data shown in the Supporting Information, Figure S 4-2 and Figure S 4-3).

catalyst	Reactant	$r_{C3,0}\cdot10^{-7}$ (mol g^{-1} s^{-1})	$r_{C3=,0}\cdot10^{-7}$ (mol g^{-1} s^{-1})	$S_{C3=,0}$
6V/SBA-15	$CH_3CH_2CH_3$	1.86	1.61	87
	$CH_3CD_2CH_3$	1.25	0.94	75
	$CD_3CD_2CD_3$	1.24	0.33	27
M1	$CH_3CH_2CH_3$	20.8	18.5	89
	$CH_3CD_2CH_3$	14.0	8.7	62
	$CD_3CD_2CD_3$	9.0	7.9	88

In contrast, both, deuteration of the methylene as well as the methyl group affects the rate of propane consumption over the M1 catalyst resulting in a KIE for methylene of 1.49 and for methyl of 1.55. In case of fully deuterated propane the rate is further decreased yielding an overall KIE of 2.31. This means that the hydrogen atoms in methylene as well as methyl position are simultaneously involved in the consumption of propane by rate determining process(es). Parallel formation of iso-propoxide that requires C-H activation in methylene position and n-propoxide that requires C-H activation in methyl position should not be responsible for the observed effect, since propionaldehyde is also formed over 6V/SBA-15 to a similar extent (compare Figure 4-1a-b, and Figure S 4-1), but here the deuteration of the methyl group has no impact.

Table 4-2 Kinetic isotope effects (KIE) in propane consumption (C3) and propylene formation (C3=) calculated based on the rates provided in Table 4-1.

catalyst	Isotopes	KIE (C3)	KIE (C3=)
6V/SBA-15	$CH_3CH_2CH_3$/ $CH_3CD_2CH_3$	1.49	1.72
	$CH_3CD_2CH_3$/ $CD_3CD_2CD_3$	1.01	2.84
	$CH_3CH_2CH_3$/ $CD_3CD_2CD_3$	1.50	4.87
M1	$CH_3CH_2CH_3$/ $CH_3CD_2CH_3$	1.49	2.13
	$CH_3CD_2CH_3$/ $CD_3CD_2CD_3$	1.55	1.10
	$CH_3CH_2CH_3$/ $CD_3CD_2CD_3$	2.31	2.34

The results may be interpreted in terms of a different structure of the intermediate in propylene formation on M1 compared to 6V/SBA-15 that leads to similar barriers for the abstraction of the first and the second hydrogen atom, respectively. For better illustration, the part of the reaction network (Scheme 4-3) that seems to predominate propylene formation is enlarged in Scheme 4-4 and the differences between M1 and 6V/SBA-15 are highlighted in blue and green, respectively. Over M1 the limiting case might be a simultaneous mechanism, which seems to be not unlikely over Mo oxide containing catalysts according to DFT calculations using Mo_3O_9 model clusters.[18] Our experimental numbers agree well with calculated KIEs from a 2 + 4 pathway in which both methyl and methylene C-H bonds are simultaneously involved. However, the calculated barrier for the corresponding transition state (48.3 kcal mol^{-1}) is higher compared to the experimentally determined value of 34 kcal mol^{-1}.[4] The 2 + 4 mechanism corresponds to a concerted heterolytic C-H activation (two-electron process) in which all in all 6 electrons are involved simultaneously including both metal atom and oxygen atom of a M=O species as active site. The one-electron hydrogen abstraction under formation of a radical is, however, the energetically most feasible pathway in propane activation over Mo_3O_9 model clusters,[18] and also over vanadium oxide.[19] Therefore, quasi-simultaneous H-abstraction on neighbouring M=O sites (Scheme 4-4) might be taken into

consideration as an explanation for the KIEs measured over M1. Such a mechanism has not been studied by theory so far. The high density of propane adsorption sites on the surface of M1[4] might render such a mechanism possible. Interestingly, a high density of oxidising sites has been reported to favour propylene formation instead of C-C bond cleavage reactions on vanadium-based oxides.[20]

Furthermore, we analysed the rates of propylene formation albeit interpretation of the corresponding data is less straightforward, since formation of propylene requires the abstraction of two hydrogen atoms that must occur via several elementary steps. Interestingly, the selectivity to propylene is affected in a different way by isotope labelling over 6V/SBA-15 and M1 (Table 4-1). Consecutive reactions of the formed propylene are neglected in the following discussion of the difference, since the initial selectivity to propylene $S_{C3=,0}$ was determined based on extrapolation to zero propane conversion. Still, parallel reactions of propane may affect propylene formation rates at zero conversion, but the selectivity of propylene approaches approximately 90% at X = 0% in the reaction of native propane over both catalysts due to parallel formation of n-propoxide and its further oxidation (Table 4-1). By using fully deuterated propane the selectivity to propylene drops to 27% compared to the reaction of native propane (87% propylene selectivity) over 6V/SBA-15. After abstraction of the first D atom in the reaction of C_3D_8, a C_3D_7 intermediate is formed on 6V/SBA-15 that reacts in the second step either to fully deuterated propylene by another D abstraction at the neighbouring methyl group (k_1 in Scheme 4-1) or to undesired by-products via an unspecified pathway (k_2 in Scheme 4-1). The ratio of the corresponding two rate constants determines the selectivity to propylene in the isotope exchange experiments in the limiting case of zero per cent conversion of propane. The decrease in propylene selectivity in the conversion of fully deuterated propane over 6V/SBA-15 points at a reaction pathway competitive to selective C-D activation in the C_3D_7 intermediate, which is not decelerated by isotope exchange, i.e., which does not involve D-C bond splitting. Competitively, reactions with gas-phase oxygen via alkylperoxy and hydroperoxyalkyl radicals,[21] or fast attack of adsorbed oxygen at the carbon backbone of C_3D_7 in the adsorbed state may occur (Scheme 4-4). By using $CH_3CD_2CH_3$ instead of native propane the selectivity to propylene is only slightly affected over 6V/SBA-15 (Table 4-1), because only the first

step from $CH_3CD_2CH_3$ to CH_3CDCH_3, which determines activity, but not selectivity, involves D abstraction. Propylene is formed in the subsequent step by abstraction of H from the methyl group of the CH_3CDCH_3 intermediate, like in case of native propane. However, the k_1/k_2 ratio may be influenced by secondary isotope effects resulting in slightly diminished selectivity of 75% compared to 87% for native propane (Table 4-1). Trends in the KIE's determined based on propylene formation rates (Table 4-2) are in agreement with this view.

M1 exhibits a different behaviour indicating that only deuteration of the methylene C-H bonds facilitates formation of undesired by-products (Table 4-1). As discussed above, the KIE determined over M1 based on propane consumption rates at zero conversion is invariant with regard to the methylene or methyl position. That means that complete deuteration of propane retards the overall reaction, but will not interfere the structure of the transition states and intermediates, which is reflected in equal selectivity to propylene for native propane (89%) and fully deuterated propane (88%) at zero propane conversion (Table 4-1). Other than on 6V/SBA-15, destruction of the carbon skeleton of the C_3D_7 intermediate does not occur preferentially. No change in the k_1/k_2 ratio (Scheme 4-1) is in agreement with a low concentration of electrophilic oxygen species and adsorbed oxygen on the surface of M1. The equal selectivity in the experiments with native and fully deuterated propane, respectively, also support that consecutive reactions of propylene (at least reactions that involve C-(H,D) splitting, such as allylic oxidation) are indeed negligible under the applied boundary conditions of zero propane conversion. In contrast, selectivity decreases by 27% over M1 when propane is deuterated in 2-position. The difference between M1 and 6V/SBA-15 is easily plausible when a simultaneous H-abstraction mechanism is assumed over M1 (Scheme 4-4), which is in agreement with the KIEs measured over M1 and the much higher number of propane adsorption sites on the surface of M1 compared to 6V/SBA-15.[4] Upon exchange of H by D in 2-position a simultaneous mechanism is no longer possible leading to faster abstraction of methyl hydrogen that results in the formation n-propyl species as precursor of saturated oxygenated products and carbon oxides (Scheme 4-3 and Scheme 4-4).

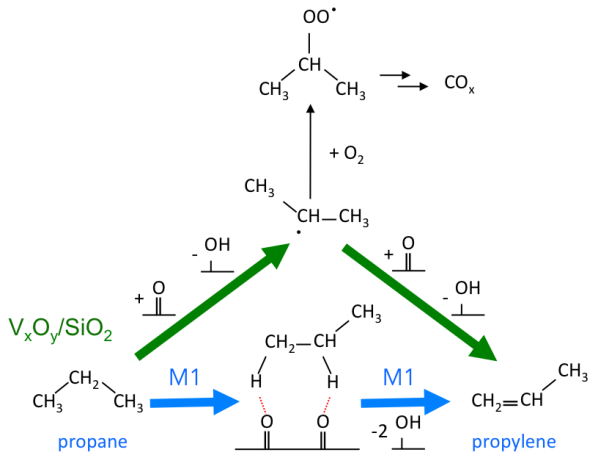

Scheme 4-4 Differences in the formation mechanism of propylene over silica-supported vanadium oxide (green) and M1 (blue) analysed based on KIE measurements.

Table 4-3 Propane conversion and product selectivity in dependence of steam addition (10 vol%) to the feed at 400 °C, W/F = 0.06 g s ml^{-1} (M1), and 1.34 g s ml^{-1} (6V/SBA-15) and C_3H_8/O_2/He = 10/5/85.

	M1		6V/SBA-15	
	H_2O	D_2O	H_2O	D_2O
X [%]	1.8	1.8	2.0	2.1
$r_{propane\ consumption,0}$ (mmol g^{-1} h^{-1})	4.81	4.82	0.247	0.255
S (propylene) [%]	65.8	70.4	77.8	78.1
S (acrylic acid) [%]	30.0	25.0	0.2	0.2
S (acetic acid) [%]	1.3	1.5	5.3	5.2
S (C2) [%]	0.1	0.1	0.2	0.2
S (CO) [%]	2.0	2.2	9.9	9.7
S (CO_2) [%]	0.8	0.9	6.7	6.7

It should be noted that re-establishment of the active catalyst surface after hydrocarbon oxidation (after first half of the catalytic cycle) can also influence the KIE. The rate constant for re-oxidation of an oxygen vacancy on the catalyst surface, which is formed during formation of H_2O from two OH groups, should be the same for (partially) deuterated and native propane. However, the (formal) rate constants of catalyst dehydration likely differ among each other depending on the degree of deuteration of the hydrocarbon substrate, as deuteration of the surface depends on the deuterium content of the substrate and dehydration of the surface in the final step of the catalytic cycle

involves necessarily the cleavage of an O-H/O-D bond. The impact of catalyst re-oxidation on the reaction rates was investigated by adding H_2O or D_2O to the feed of native propane and oxygen under steady state conditions to modify the concentration of surface OH or OD groups (Table 4-3). Switching from H_2O to D_2O does not change the activity of both catalysts, indicating that catalyst dehydration does not affect KIEs obtained with deuterated propane. The selectivity pattern is not affected over 6V/SBA-15 in a measurable way. For M1, selectivity of acrylic acid is slightly higher in H_2O compared to D_2O at the expense of all other products. This indicates direct involvement of water in a kinetically relevant step of acrylic acid formation or vital H/D exchange in the intermediate product propylene, which results in deceleration of allylic oxidation as a consequence of the KIE for C-H/C-D bond cleavage. In any case the observation implies the existence of an additional kinetically relevant step in the reaction network, which is located within the path from propylene to acrylic acid.

The formation pathways of carbon oxides during propane oxidation were studied by means of pulse experiments with ^{13}C-labelled/unlabelled propane/oxygen mixtures at T = 400 °C. A schematic illustration of the experimental procedure is provided in the Supporting Information (Scheme S 4-2). The applied labelled propane contains the ^{13}C atom in 2-position (labelled in red in Scheme 4-3 and Scheme 4-5). The products of the pulse experiments were analysed by mass spectrometry after pre-separation of the product mixture into permanent gases (CO, CO_2, and O_2), hydrocarbons (C_3H_6, C_3H_8), and acids by packed columns (for experiment description see Supporting Information). Propane conversion and product selectivity are summarized in Table 4-4. The conversion of propane has been adjusted for the two catalysts by choosing appropriate contact times. The conversion does not differ between native and ^{13}C-2-propane. The propylene selectivity measured over the two catalysts was only slightly affected by isotope labelling.

In the experiments with the unlabelled reactant, CO and CO_2 are formed in almost equal amounts with some excess of CO, which is reflected in a selectivity ratio $CO/(CO+CO_2)$ slightly greater than 0.5 (Table 4-4). The overall $CO/(CO+CO_2)$ ratio changes only slightly when using labelled propane, resulting in values of 0.54 for 6V/SBA-15 and 0.48 for M1. The observed deviations are within the error of carbon oxides detection. The

proposed reaction network (Scheme 4-3) features a multitude of reaction pathways that finally yield both CO and CO_2. But when the ^{13}C-labelled reactant is pulsed, distinct differences in the origin of CO and CO_2 over the two catalysts become obvious (Scheme 4-5).

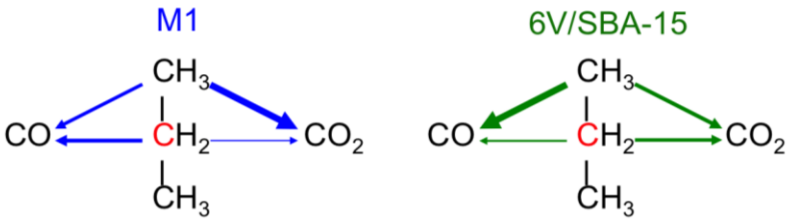

Scheme 4-5 Predominant origin of carbon oxides over M1 (blue) or 6V/SBA-15 (green); Line thickness of arrows reflects the selectivity presented in Table 4-4.

Over M1 the carbon in methylene position contributes slightly more to CO formation compared to the carbon in methyl position as indicated by the higher $^{13}CO/(^{13}CO+^{13}CO_2)$ ratio of 0.75, whereas CO_2 preferentially originates from one of the terminal carbon atoms (Table 4-4, Scheme 4-5). The opposite pattern is observed over 6V/SBA-15, i.e., CO originates mainly from the methyl position and CO_2 from the methylene position, respectively.

Table 4-4 Propane conversion and product selectivity for native and ^{13}C-substituted propane in propane oxidation in a feed of $C_3H_8/O_2/He$ = 10/5/85 at T = 400°C; W/F = 0.06 g s ml^{-1} (M1), and 1.34 g s ml^{-1} (6V/SBA-15).

Catalyst	Reactant	X (C_3H_8) [%]	S (C_3H_6) [%]	S (^{12}CO) [%]	S ($^{12}CO_2$) [%]	S (^{13}CO) [%]	S ($^{13}CO_2$) [%]	$\frac{S_{^{12}CO}}{S_{^{12}CO}+S_{^{12}CO_2}}$	$\frac{S_{^{13}CO}}{S_{^{13}CO}+S_{^{13}CO_2}}$
M1	C_3H_8	4.0	69.4	15.9	14.6	-	-	0.52	-
	^{13}C-2-C_3H_8	4.0	68.1	7.2	13.8	8.2	2.8	0.34	0.75
6V/SBA-15	C_3H_8	4.6	65.3	19.2	15.4	-	-	0.55	-
	^{13}C-2-C_3H_8	4.5	62.8	15.3	9.1	4.7	8.2	0.63	0.36

The observation that the majority of CO_2 formed over M1 is unlabelled indicates that the C3 intermediate to CO_2 predominantly bears a terminal functional group that contains two oxygen atoms (e.g., a carboxylic acid group). The C3 acid is acrylic acid, since

propionic acid is not formed over M1 under the applied reaction conditions (Figure 4-1a). The elimination of unlabelled CO_2 (decarboxylation) from acrylic acid gives a residual C2 fragment.

Acetaldehyde, labelled either at the carbonyl group or at the methyl carbon, and ethylene are the C2 products primary formed either from acrolein or acrylic acid (Scheme 4-3). As discussed above, ethylene might be a quite stable end product. Acetaldehyde can be either oxidized at the methyl group and subsequently decarbonylated to give adsorbed methoxy species or it is further oxidized to acetic acid by oxygen insertion into the C-H bond of the CHO group. Acetaldehyde, which is labelled at the carbonyl group, yields labelled CO by decarbonylation and an unlabelled surface methoxy group. The latter may be oxidized to formate species, which finally form CO by decarbonylation or CO_2 by decarboxylation, both unlabelled (Scheme 4-2, top).

The labelled ^{13}C atom in acetic acid formed over M1 is primarily located in the methyl group, as indicated by mass spectrometry (Figure 4-2). The mass spectrum of pure native acetic acid (Figure 4-2a) displays two major fragments corresponding to a carboxylate CO_2H^+ species (m/z 45) and a CH_3CO^+ species (m/z 43), which are also present in the pre-separated acetic acid fraction of the product mixture observed in oxidation of native propane (Figure 4-2b). Peaks due to $^{13}CH_3CO^+$ or $CH_3{}^{13}CO^+$ (m/z 44), CO_2H^+ (m/z 45) and $^{13}CO_2H^+$ (m/z 46) are observed when labelled ^{13}C-2-propane is pulsed. The measured intensity ratio of these three peaks can be simulated by a $^{13}CH_3CO_2H$:$CH_3{}^{13}CO_2H$ ratio of 3:1 indicating preferred formation of acetic acid with the ^{13}C atom located at the methyl position. This means that either acrolein or acrylic acid is preferentially attacked at the terminal methylene group, but attack at the central carbon is also possible, but less likely.

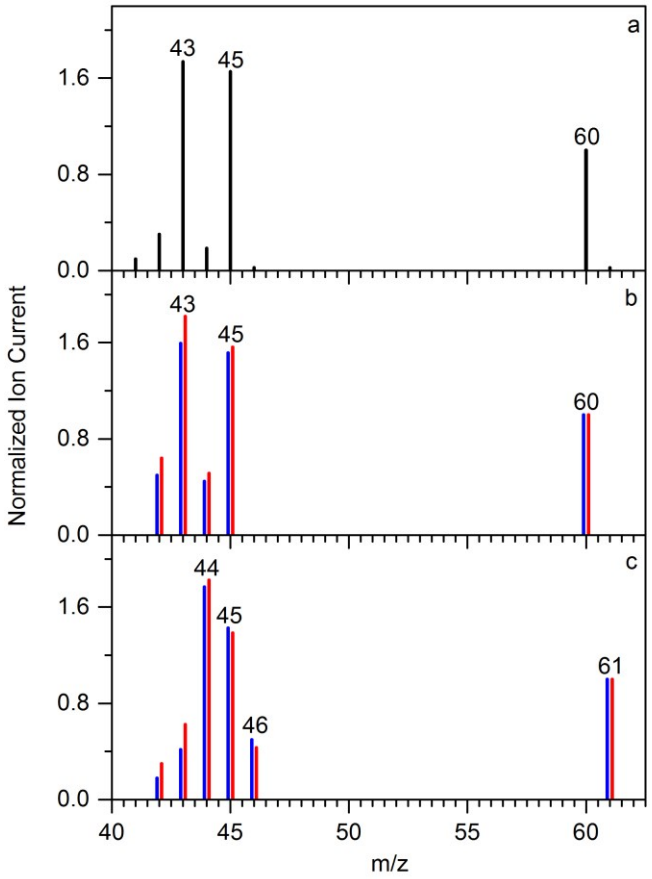

Figure 4-2 Mass spectrum of 2.6vol-% acetic acid in He (a), mass spectrum of the acid fraction of the product mixture in the oxidation of native propane (b), and ^{13}C-2-propane (c) on M1 at T = 400 °C, W/F = 0.3 g s ml^{-1} and C_3/O_2/He = 20/5/75 (blue) and 15/5/80 (red); The propane content in the feed was increased in the corresponding experiments to increase the reliability of acetic acid analysis.

Acetic acid that contains a labelled methyl group releases unlabelled CO_2 in a decarboxylation reaction. The residual labelled surface methoxy group is further oxidized to labelled CO or CO_2, respectively (Scheme 4-2, bottom).

All decomposition reactions of the C3 oxygenates acrolein and acrylic acid outlined in Scheme 4-3 may occur in parallel, but the product distribution observed over M1 and 6V/SBA-15 in the temperature-programmed experiments (Figure 4-1) and the distribution of the ^{13}C isotope in the final combustion products CO and CO_2 (Table 4-4, Scheme 4-3) indicate differences in reaction rates of the individual steps. The high concentration of acrylic acid in the product mixture and the preferential formation of unlabelled CO_2 suggest that over M1 oxidation of acrolein to acrylic acid via oxygen

insertion into the C-H bond of the CHO group is faster than oxidation of the vinyl group followed by decarbonylation of the resulting surface species and acetaldehyde formation. In contrast, decarbonylation of acrolein is preferred over 6V/SBA-15 as indicated by the increased fraction of unlabelled CO. For clarity, the corresponding section of Scheme 4-3 is enlarged in Scheme 4-6 and the major differences between M1 (blue) and silica-supported vanadium oxide (green) are highlighted.

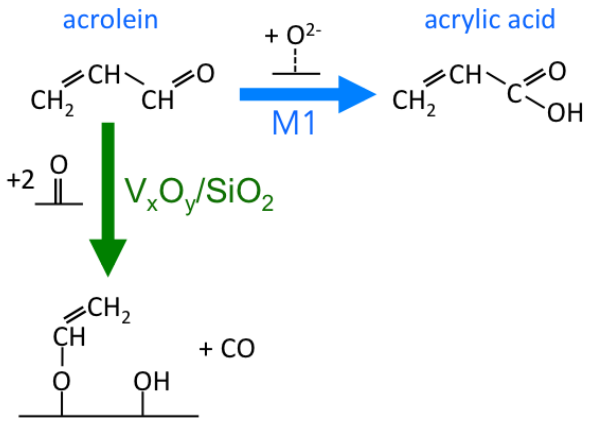

Scheme 4-6 Major differences in consecutive reactions of acrolein over M1 (blue) and 6V/SBA-15 suggested by the distribution of ^{13}C in the formed carbon oxides.

Similarly, over M1 the common intermediate acetaldehyde seems to be faster oxidized at the CHO group under formation of acetic acid. In contrast, over 6V/SBA-15 the methyl group of acetaldehyde is faster oxidized followed by decarbonylation of the corresponding surface intermediate.

An interpretation of the increased abundance of labelled CO_2 over 6V/SBA-15 is less straightforward. The decomposition of adsorbed acetone may contribute more significantly to labelled CO_2 over 6V/SBA-15, whereas acetone formed over M1 is more stable. In addition, differences in the decomposition of the final surface formate (Scheme 4-2, bottom right) either via decarboxylation or decarbonylation may contribute to the observed pattern.

4.3 Summary and Conclusions

In summary, the measurement of kinetic isotope effects in propane oxidation revealed essential differences in the activation of the propane molecule over M1 and silica-supported vanadium oxide, respectively. Whereas over silica-supported vanadium oxide the abstraction of the first hydrogen atom at the methylene group of the C_3H_8 molecule is rate limiting, activation of propane over M1 clearly involves both, methyl and methylene groups, simultaneously in rate-limiting process(es). The difference has no significant impact on the network of consecutive reactions of the formed propylene, but it may explain the lower barrier measured over M1,[4] and the corresponding difference between M1 and 6V/SBA-15 in propane consumption rate that comprises one order of magnitude.[4] At usually applied reaction temperatures (300 – 400 °C) the overall reaction network in propane oxidation seems to be similar over silica-supported vanadium oxide and M1 with the allylic oxidation of propylene being the predominant pathway since the intermediate allylic alcohol has been detected over both catalysts. The final product of the allylic oxidation over M1 is acrylic acid, while the reaction essentially terminates with acrolein formation over silica-supported vanadium oxide. Acetone formation via oxihydration or oxidation of propylene is a minor parallel pathway. Carbon oxides are mainly formed by decomposition of the main selective oxidation products acrolein and acrylic acid, which are preferentially attacked at the terminal methylene group under formation of the common decomposition product acetaldehyde. Differences in the preferred degradation pathways of acetaldehyde have been revealed by pulse experiments using ^{13}C-2-propane. Over silica-supported vanadium oxide acetaldehyde seems to be preferentially oxidized at the methyl group followed by decarbonylation, whereas oxidation to acetic acid followed by decarboxylation is the favoured reaction path over M1.

The most important differences in the reaction network of propane oxidation under the studied conditions over the bulk catalyst M1 and the monolayer catalyst 6V/SBA-15 have been detected in the formation mechanism of propylene (Scheme 4-4) and in the consecutive reaction of acrolein (Scheme 4-6). The differences in the reaction network over the two catalysts originate from differences in the surface concentration and distribution of oxygen species under reaction conditions. Based on the temperature-

programmed experiments the formed products can be classified into olefins, carbonyl compounds, and acids. Propylene is formed at very low temperatures indicating clearly that the strength of the C-H bond is no particular hurdle in propane activation in general. The result is in contrast to the popular opinion in oxidation catalysis that the thermodynamic stability of C-H bonds in substrate molecules and intermediates determines the selectivity.[22] Homolytic hydrogen abstraction has been proposed to be the favoured reaction path in propane activation over vanadium oxide.[19,23] The activation requires nucleophilic oxygen and the vanadyl oxygen has been considered to be the most active one.[19b,19c] The formation of acrolein as the major carbonyl compound in the product mixture occurs also at comparatively low temperatures perhaps via attack of propylene by electrophilic oxygen species, which seem to be more abundant on the surface of silica-supported vanadium oxide compared to M1 due to the different electronic structure of the two catalysts as outlined in detail recently.[4] Finally, formation of acids requires particularly high temperatures, especially over silica-supported vanadium oxide. This implies that oxygen atoms, which are part of surface oxide species, are involved in the corresponding reaction.

Our results confirm that control over occurrence and distribution of the various oxygen species on the surface of vanadium oxide catalysts is the key issue in terms of selectivity. Selective oxidative dehydrogenation of propane to propylene requires the suppression of any electrophilic oxygen species on the catalyst surface, which might be solved by pulsed operation under alternate oxidizing and reducing conditions.[24] The implementation of selective acrolein formation is more challenging, because it requires electrophilic oxygen species and faces the competitive oxidation of propylene in 2-position under formation of acetone and the consecutive oxidation to acetaldehyde that occur in the same temperature range. A more detailed analysis of the impact of reaction parameters on the rates within the network is required to find solutions. The formation of acrylic acid may be controlled via appropriate design of the solid-state chemistry of the catalysts in terms of oxygen species that selectively insert into the C-H bond of a terminal CHO group. At this point we refer to the difference between silica-supported vanadium oxide and M1 in the onset temperature of acrylic acid formation. However, high selectivity to acrylic acid requires in addition and primarily the optimization of acrolein formation as well as the

suppression of consecutive reactions such as the oxidative attack at the CH_2 group of acrylic acid.

4.4 Experimental Section

4.4.1 Catalysts

Synthesis, and detailed bulk as well as surface analysis of the two catalysts have been described elsewhere.[4]

4.4.2 Propane oxidation experiments

Catalytic measurements were carried out in a self-constructed reactor setup with plug-flow characteristics using 10 or 50 mg (M1) and 223 mg (6V/SBA-15) catalyst. SiC was used to dilute the M1 catalyst for adjusting the same bed length as for 6V/SBA-15. The reactor (inner diameter 4 mm) was equipped with a thermocouple for measuring the temperature inside the catalyst bed. C_3H_8 (Westfalen), C_3D_8 (Campro Scientific 99 atom% D, Sigma Aldrich 99 atom% D), 2,2-$C_3D_2H_6$ (Sigma Aldrich 98 atom% D), ^{13}C-2-propane (ICON Isotopes 99 atom% 13C), O_2 (Westfalen) were used as reactants. The product gas mixtures were analyzed by online gas chromatography (Agilent 7890) and online mass spectrometry (QMA 400, Pfeiffer Vacuum). Separation of the gas pulses during ^{13}C-2-propane experiments were achieved by using a self packed column (PorapakTM Type Q 100-120 Mesh or CarbopackTM B-DA 80-120 Mesh) located between reactor outlet and analytics. More details concerning the performed experiments are provided in the Supporting Information (Scheme S 4-2 und corresponding explanation). Starting and reference point for all measurements were a reaction temperature of 400 °C and a dry feed of 10% native propane, 5% oxygen and 85% He. H_2O and D_2O (Sigma Aldrich 99.9 atom % D) were introduced into the reactant stream via vaporizer at 140 °C. The calculation of propane conversion and product selectivity includes a correction for gas impurities in the initial gas mixture (namely labelled propylene in labelled propanes). Isotopic scrambling in propane in the gas phase as well as H/D exchange with the catalyst surface can be neglected (Supporting Information, Figure S 4-4).

4.5 Supporting Information

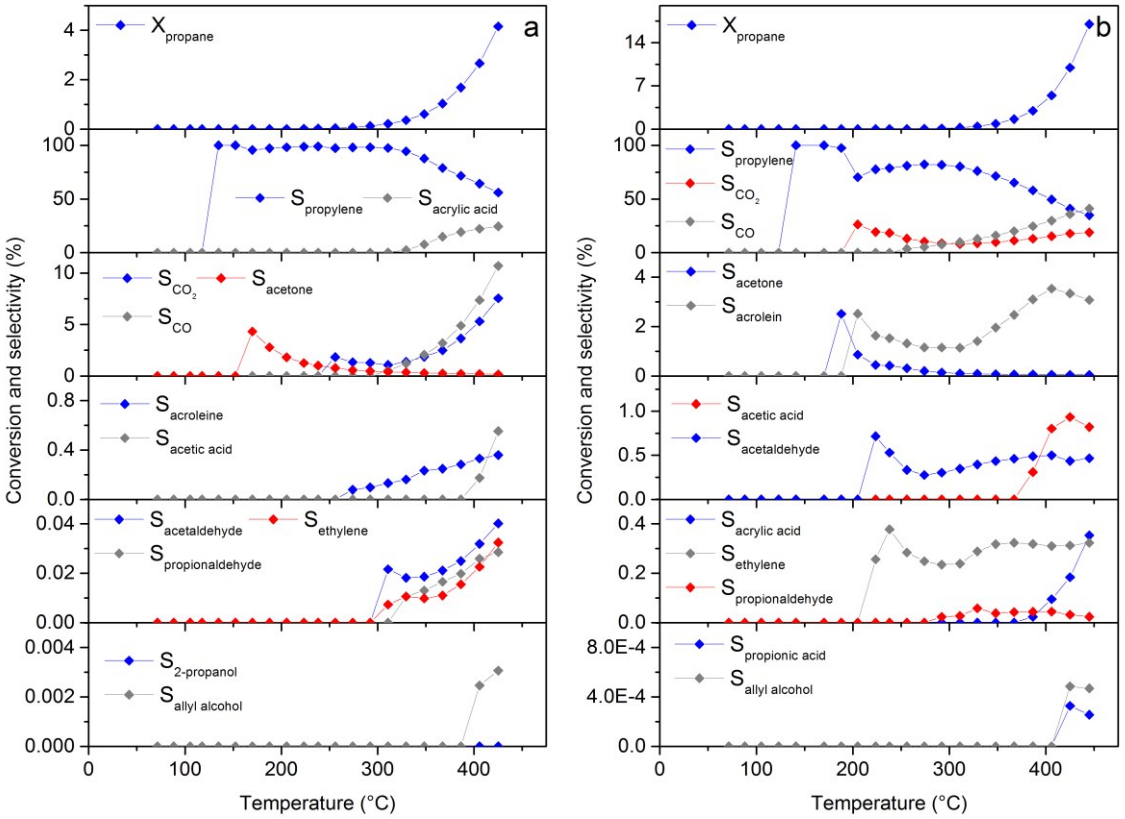

Figure S 4-1 Selectivity of reaction products as a function of temperature for the temperature-programmed oxidation of propane (heating rate 1 °C min^{-1}, measurement isothermal every 20 K) over a) M1 (C_3H_8/O_2/He = 10/5/85, W/F = 0.06 g s ml^{-1}, m_{cat} = 10 mg, F_{total} = 10 ml min^{-1}), and b) 6V/SBA-15 (C_3H_8/O_2/He = 10/5/85, W/F = 1.33 g s ml^{-1}, m_{cat} = 222 mg, F_{total} = 10 ml min^{-1}).

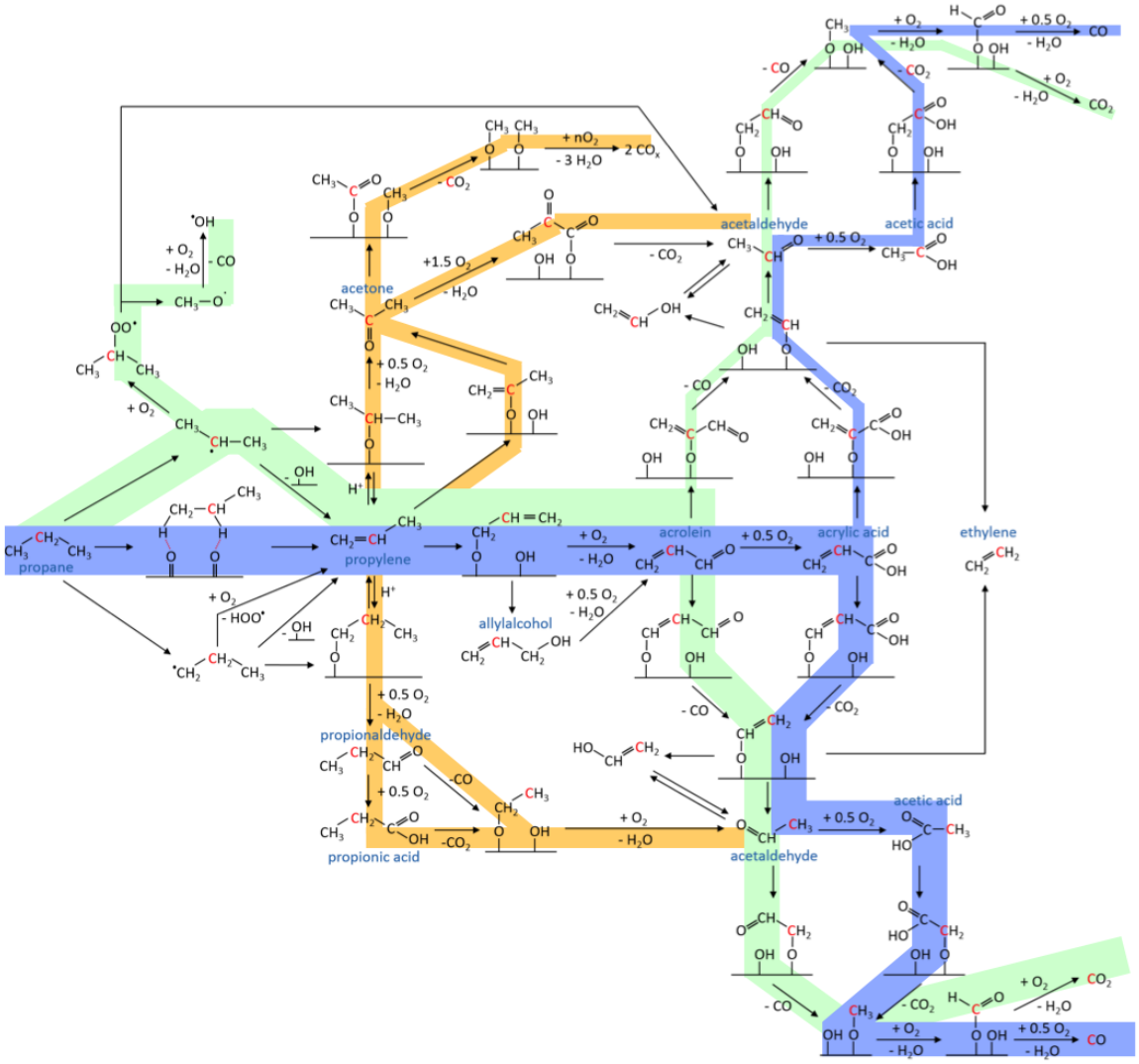

Scheme S 4-1 Coloured version of Scheme 4-3 presented in the main text that highlights the major principal agreements and differences in the reaction networks over 6V/SBA-15 (green path), and M1 (blue path); The pathways highlighted in orange occur on both catalysts in a similar way.

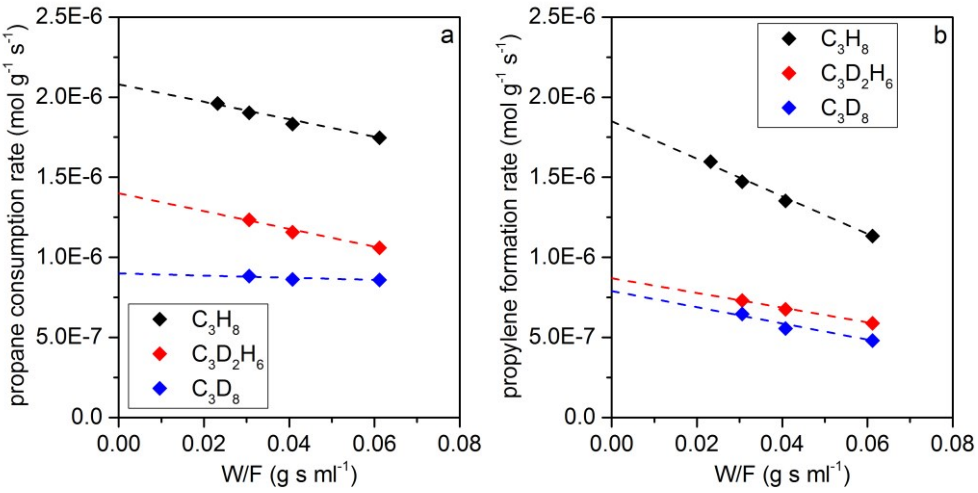

Figure S 4-2 Propane consumption rates (a) and propylene formation rates (b) as function of W/F (0.02 – 0.06 g s ml^{-1}) for M1 in the feed $C_3H_8/O_2/He$ = 10/5/85 at T = 400 °C for different isotopes.

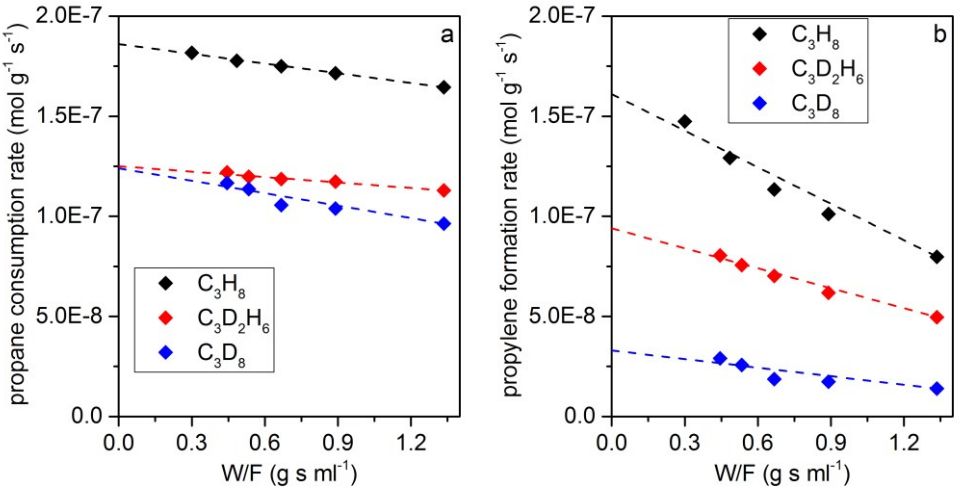

Figure S 4-3 Propane consumption rates (a) and propylene formation rates (b) as function of W/F (0.30 – 1.34 g s ml^{-1}) for 6V/SBA-15 in the feed $C_3H_8/O_2/He$ = 10/5/85 at T = 400°C for different isotopes.

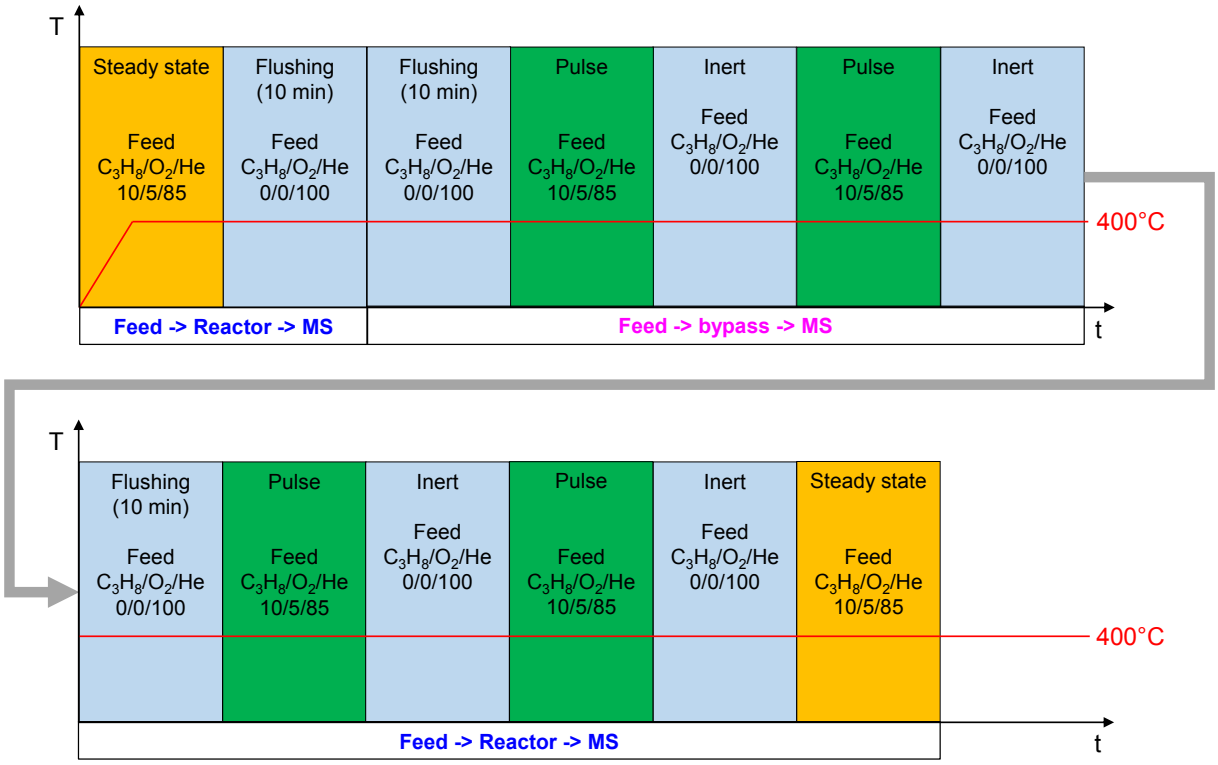

Scheme S 4-2 Schematic illustration of ^{13}C-labelled/unlabelled propane pulse sequence.

The catalysts (W/F = 0.06 g s ml^{-1} for M1 or 1.34 g s ml^{-1} for 6V/SBA-15) were heated to 400 °C (heating rate of 2 °C min^{-1}) in a feed of 10% propane, 5% oxygen, and 85% helium and kept at this temperature and contact time for the entire pulse experiment. After 24 hours at steady state, the reactor was flushed with helium for 10 minutes and switched to bypass mode followed by flushing for 10 minutes with helium. 1 ml of a gas mixture, containing 10% propane, 5% oxygen 85% helium, was injected into the helium flow to determine the blank values of the setup. The system was then flushed for 1 min with helium. The injection of 1 ml gas mixture followed by flushing with helium was performed twice in bypass mode. Afterwards the setup was switched back to reactor mode and flushed for 10 minutes with helium. The injection of 1 ml of the same gas mixture followed by flushing with helium was performed twice in reactor mode on the catalyst. The effluent gas both in bypass and reactor mode were separated into permanent gases and hydrocarbons by a self-packed Porapak Q column. For preparation of the column, a stainless steel tube (1/8" outer diameter, 2 mm inner diameter, 20 cm length) was filled with Porapak Q material (Supelco, particle size 125 to 150 µm). The

composition of the separated fractions was analysed with a QMA-400 mass spectrometer. Propane conversion and product selectivity were calculated based on calibration factors obtained by injection of 1ml of different test gases (1% CO, 1% CO_2, 1% O_2, 47% Ar and balance N_2; 1% propane, 1% propylene and balance N_2). After each pulse experiment, the catalysts were fed with a mixture of 10% propane, 5% oxygen, and 85% helium to check if the steady state has changed. The pulse experiment was repeated with an injection gas mixture, containing 5% propane, 5% oxygen and balance helium and a steady state feed of 10% propane, 5% oxygen, and 85% helium.

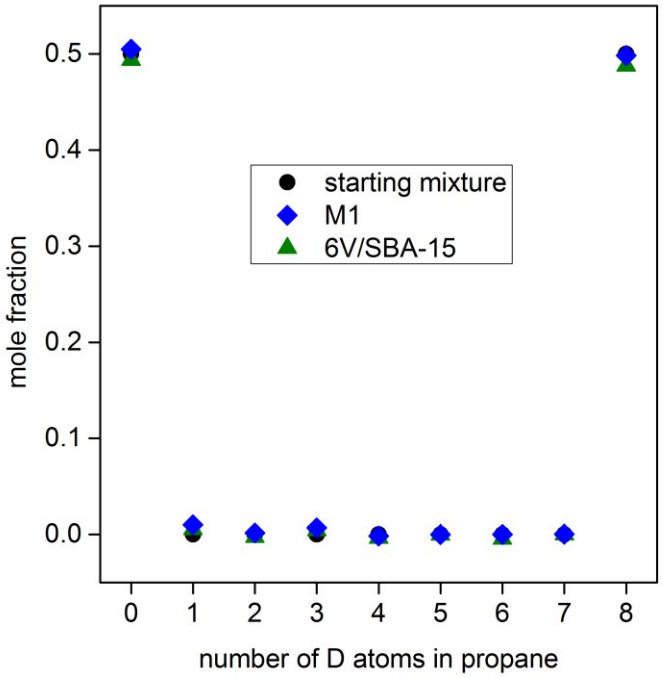

Figure S 4-4 Deuterium distribution in propane during the reaction of $C_3H_8/C_3D_8/O_2/He$ over 6V/SBA-15 and M1 and for bypass measurement at 400 °C, W/F = 1.34 g s ml^{-1} (6V/SBA-15) and 0.06 g s ml^{-1} (M1) and feed $C_3H_8/C_3D_8/O_2/He$ = 5/5/5/85.

A test for H/D exchange of propane with the catalyst surface, which is also a test for reversibility of the C-H bond breaking, was performed to find out if H/D exchange plays a role during KIE experiments. A feed containing $C_3H_8/C_3D_8/O_2/He$ was pulsed over the catalyst and the product gas was measured by mass spectrometry to find a significant evidence for partial deuterated propane as product of H/D exchange. The results are summarized in Figure S 4-4 and show for both catalysts under the applied reaction

conditions no significant H/D exchange of the reactant molecule, meaning that the mole fraction of partial deuterated propane is practically zero. These results also suggest that isotopic scrambling of H and D in partial deuterated propane plays no role.

4.6 References

[1] a) C. Coperet, *Chemical Reviews* **2010** *110*, 656-680; b) C. A. Gärtner, A. C. van Veen, J. A. Lercher, *ChemCatChem* **2013** *5*, 3196-3217.

[2] a) M. M. Bettahar, G. Costentin, L. Savary, J. C. Lavalley, *Applied Catalysis A: General* **1996**, *145*, 1-48; b) D. L. Stern, R. K. Grasselli, *Journal of Catalysis* **1997**, *167*, 560-569; c) M. Lin, T. B. Desai, F. W. Kaiser, P. D. Klugherz, *Catalysis Today* **2000**, *61*, 223-229; d) R. Fushimi, S. O. Shekhtman, A. Gaffney, S. Han, G. S. Yablonsky, J. T. Gleaves, *Industrial & Engineering Chemistry Research* **2005**, *44*, 6310-6319; e) R. Grabowski, *Catalysis Reviews: Science and Engineering* **2006**, *48*, 199-268; f) A. Trunschke, in *Nanostructured Catalysts: Selective Oxidation Reactions*, 1 ed. (Eds.: C. Hess, R. Schlögl), RSC Nanoscience & Nanotechnology, Cambridge, **2011**, pp. 56-95; g) K. Alexopoulos, M.-F. Reyniers, G. B. Marin, *Journal of Catalysis* **2012**, *289*, 127-139; h) K. Alexopoulos, M.-F. Reyniers, G. B. Marin, *Journal of Catalysis* **2012**, *295*, 195-206; i) J. Liu, F. Mohamed, J. Sauer, *Journal of Catalysis* **2014**, *317*, 75-82.

[3] K. Chen, A. T. Bell, E. Iglesia, *The Journal of Physical Chemistry B* **2000**, *104*, 1292-1299.

[4] P. Kube, B. Frank, S. Wrabetz, J. Kröhnert, M. Hävecker, J. Velasco-Vélez, J. Noack, R. Schlögl, A. Trunschke, *ChemCatChem* **2017**, *9*, 573-585.

[5] a) C. A. Carrero, R. Schlögl, I. E. Wachs, R. Schomäcker, *ACS Catalysis* **2014**, *4*, 3357-3380; b) I. Muylaert, P. Van Der Voort, *Physical Chemistry Chemical Physics* **2009**, *11*, 2826-2832; c) C. Hess, *ChemPhysChem* **2009**, *10*, 319-326; d) F. Cavani, N. Ballarini, A. Cericola, *Catalysis Today* **2007**, *127*, 113-131; e) B. M. Weckhuysen, D. E. Keller, *Catalysis Today* **2003**, *78*, 25-46.

[6] K. Chen, E. Iglesia, A. T. Bell, *Journal of Catalysis* **2000**, *192*, 197-203.

[7] P. C. Redfern, P. Zapol, M. Sternberg, S. P. Adiga, S. A. Zygmunt, L. A. Curtiss, *The Journal of Physical Chemistry B* **2006**, *110*, 8363-8371.

[8] R. Naumann D'Alnoncourt, L. I. Csepei, M. Hävecker, F. Girgsdies, M. E. Schuster, R. Schlögl, A. Trunschke, *Journal of Catalysis* **2014**, *311*, 369-385.

[9] G.-L. Dai, Z.-H. Li, J. Lu, W.-N. Wang, K.-N. Fan, *The Journal of Physical Chemistry C* **2012**, *116*, 807-817.
[10] a) X. Gao, J.-M. Jehng, I. E. Wachs, *Journal of Catalysis* **2002**, *209*, 43-50; b) A. Khodakov, B. Olthof, A. T. Bell, E. Iglesia, *Journal of Catalysis* **1999**, *181*, 205-216.
[11] Z. Zhai, X. Wang, R. Licht, A. T. Bell, *Journal of Catalysis* **2015**, *325*, 87-100.
[12] A. Held, J. Kowalska-Kuś, K. Nowińska, *Journal of Catalysis* **2016**, *336*, 23-32.
[13] V. I. Avdeev, A. F. Bedilo, *Research on Chemical Intermediates* **2016**, *42*, 5237-5252.
[14] a) K. Amakawa, Y. V. Kolen'ko, A. Villa, M. E. Schuster, L.-I. Csepei, G. Weinberg, S. Wrabetz, R. Naumann d'Alnoncourt, F. Girgsdies, L. Prati, R. Schlögl, A. Trunschke, *ACS Catalysis* **2013**, *3*, 1103-1113; b) E. Sadovskaya, V. Goncharov, G. Popova, E. Ishchenko, D. Frolov, A. Fedorova, T. Andrushkevich, *Journal of Molecular Catalysis A: Chemical* **2014**, *392*, 61-66; c) C. Heine, M. Hävecker, M. Sanchez-Sanchez, A. Trunschke, R. Schlögl, M. Eichelbaum, *The Journal of Physical Chemistry C* **2013**, *117*, 26988-26997.
[15] L. Bui, R. Chakrabarti, A. Bhan, *ACS Catalysis* **2016**, *6*, 6567-6580.
[16] A. Dinse, S. Khennache, B. Frank, C. Hess, R. Herbert, S. Wrabetz, R. Schlögl, R. Schomäcker, *Journal of Molecular Catalysis A: Chemical* **2009**, *307*, 43-50.
[17] a) E. Finocchio, G. Busca, V. Lorenzelli, R. J. Willey, *Journal of the Chemical Society, Faraday Transactions* **1994**, *90*, 3347-3356; b) A. A. Davydov, *Molecular spectroscopy of oxide catalyst surfaces*, John Wiley & Sons Ltd., Chinchester, **2003**; c) P. Concepción, P. Botella, J. M. López Nieto, *Applied Catalysis A: General* **2004**, *278*, 45-56; d) Y. Wang, W. Zheng, F. Chen, X. Zhan, *Applied Catalysis A: General* **2008**, *351*, 75-81; e) D. Shee, G. Deo, *Journal of Molecular Catalysis A: Chemical* **2009**, *308*, 46-55; f) J. M. Lopez Nieto, B. Solsona, P. Concepcion, F. Ivars, A. Dejoz, M. I. Vazquez, *Catalysis Today* **2010**, *157*, 291-296; g) R. Lopez-Medina, I. Sobczak, H. Golinska-Mazwa, M. Ziolek, M. A. Banares, M. O. Guerrero-Perez, *Catalysis Today* **2012**, *187*, 195-200.

[18] G. Fu, X. Xu, X. Lu, H. L. Wan, *Journal of Physical Chemistry B* **2005**, *109*, 6416-6421.

[19] a) H. Fu, Z.-P. Liu, Z.-H. Li, W.-N. Wang, K.-N. Fan, *Journal of the American Chemical Society* **2006**, *128*, 11114-11123; b) X. Rozanska, R. Fortrie, J. Sauer, *The Journal of Physical Chemistry C* **2007**, *111*, 6041-6050; c) X. Rozanska, R. Fortrie, J. Sauer, *Journal of the American Chemical Society* **2014**, *136*, 7751-7761.

[20] E. V. Kondratenko, M. Y. Sinev, *Applied Catalysis A: General* **2007**, *325*, 353-361.

[21] J. Zádor, C. A. Taatjes, R. X. Fernandes, *Progress in Energy and Combustion Science* **2011**, *37*, 371-421.

[22] C. Batiot, B. K. Hodnett, *Applied Catalysis A: General* **1996**, *137*, 179-191.

[23] F. Gilardoni, A. T. Bell, A. Chakraborty, P. Boulet, *Journal of Physical Chemistry B* **2000**, *104*, 12250-12255.

[24] O. Ovsitser, R. Schomäcker, E. V. Kondratenko, T. Wolfram, A. Trunschke, *Catalysis Today* **2012**, *192*, 16-19.

Chapter 5 Conclusion

In the presented work three model catalysts, namely semiconducting MoVTeNb-oxide with M1 phase that has a dynamic surface enriched in V^{5+} and Te^{4+} (M1) under reaction conditions, vanadium oxide supported on insulating mesoporous silica SBA-15 (VO_x/SiO_2) and surface-functionalized carbon nano tubes stabilized by phosphorous oxide (P/oCNTs) with quinone-hydroquinone groups as active redox couple, which are able to catalyse the oxidative dehydrogenation of the short chain hydrocarbons ethane and propane, were investigated under identical reaction conditions in terms of temperature and feed composition in the mentioned reactions. The results clearly show that the olefins are the main products and the deep oxidation product CO is preferentially formed compared to CO_2 over all three catalysts. Differences are observed in the initial rates of olefin formation, the by-product spectrum and the selectivity to olefin at similar conversion. Over M1 the rate of olefin formation is 1-2 order of magnitude higher compared to VO_x/SiO_2 and P/oCNTs. Initial rate of ethylene formation is by an order of magnitude smaller compared to propylene formation over the vanadia supported and the carbon based catalyst. This is not the case over M1, because here both alkene formation rates are roughly the same. The amount of observed oxygenates in the by-product spectrum at similar conversion decreases in the order M1 > VO_x/SiO_2 > P/oCNT.

The observed activity differences are the result of different densities of propane adsorption sites (propane molecules per nm^2) and the nature of the adsorption sites on the investigated catalysts. From all three catalysts, M1 has the highest density of propane adsorption sites and the highest reaction rates. VO_x/SiO_2 and P/oCNT with their high surface areas (355 $m^2\ g^{-1}$ and 229 $m^2\ g^{-1}$) have similar densities of adsorption sites that are by a factor of 40 lower than on M1 and show nearly equal reaction rates. The fact that a catalyst needs a high surface area is not absolutely necessary in order to show high reaction rates. Much more important is the number of adsorption sites on the surface, because each individual site could undergo a reaction. Accordingly, a high number of adsorption sites are needed to show high reaction rates. Another important factor that has an influence on the activity is the nature of the adsorption site. DFT calculations has shown that the barrier for abstraction of the first hydrogen atom under formation of propyl radical on silica-supported vanadium oxide decreases with increasing cluster size

(160, 148, 139 and 132 kJ mol^{-1} for monomers, dimers, tetramers and octamers, respectively). Our obtained intrinsic barriers for propane activation of 162 and 154 kJ mol^{-1} for VO_x/SiO_2 are in good agreement with the calculated values for monomers and dimers. These sites correspond to only 0.1% and 0.6% of all V atoms at the surface. The other two catalysts M1 and P/oCNT show similar, but much lower intrinsic barriers of 143 and 139 kJ mol^{-1}, which indicates a similar activation mechanism over both catalysts. A low V_{surf} / propane ratio of 4 on M1 can be attributed to a cluster size effect that is perhaps responsible for the low intrinsic barrier on this material.

Selectivity differences over the three catalysts are the result of different rate constants of the individual reaction steps and differences in the reaction pathways of the complex reaction network. The concept by Batiot and Hodnett, which says that selectivity in oxidation catalysis depends on the gas-phase stability of reactant and products, does not work for our observed selectivity. Higher differences in olefin selectivity are observed in ethane oxidation compared to propane oxidation among the catalysts, but the concept would predict an inverse result. Also the product distribution of the investigated catalysts in ODH of ethane and propane is very different. The work clearly shows that in addition to the thermodynamic stability of reactant and product molecules the interaction of these molecules with the catalyst surface has a crucial impact on the selectivity. Weaker interaction of propylene with the V-containing catalysts surface measured by microcalorimetry compared to propane is an unexpected result. P/oCNT shows an equal interaction of propylene and propane, which is also unexpected. The different densities of adsorption sites facilitate different reaction steps in the complex reaction network on the three catalysts.

The comparison of the three model catalysts shows that the density of adsorption sites, the interactions of reactant and product molecules with the catalyst surface, and the electronic properties of the catalysts have an influence on activity and selectivity. Differences in the activation of propane, the complex reaction network, and the formation pathways of oxygenates, CO, and CO_2 for the V-containing catalysts were investigated using isotope labelled reactants and temperature-programmed reaction.

Two different activation mechanism of propane activation are observed for the V-containing catalysts by kinetic isotope effect measurements. M1 with its high density of

adsorption sites shows quasi-simultaneous hydrogen abstraction from propane in a rate-limiting process(es). The low density of adsorption sites on silica supported vanadium oxide leads to stepwise abstraction of hydrogen from propane, whereby the abstraction of the first hydrogen atom at the methylene group is rate-limiting. Differences in the activation mechanism could be the reason for the lower intrinsic barrier and the higher consumption rate measured over M1. Both catalysts show activity at very low temperatures proving that the C-H bond strength is no particular hurdle in propane activation.

The overall reaction network of propane oxidation seems to be similar over both catalysts under typical reaction temperatures, ranging from 300 to 400°C. Main consecutive reaction pathway in the network is the allylic oxidation of propylene to acrylic acid over M1 and to acrolein over VO_x/SiO_2. Minor pathways lead to acetone, propionaldehyde or propionic acid. Carbon oxides are predominantly formed by decomposition of acrolein or acrylic acid, via preferential attack at the methylene group. The resulting adsorbed vinyl group is further oxidized to acetaldehyde that decomposes with different preferred pathways over both catalysts. Decarbonylation of acetaldehyde happened on VO_x/SiO_2, whereas oxidation of acetaldehyde to acetic acid followed by decarboxylation is preferred over M1.

Main differences in the reaction network of propane oxidation between M1 and VO_x/SiO_2 are in the activation of propane/formation of propylene and in the consecutive reaction of acrolein. Origin of these differences is the different density of adsorption sites and the distribution of various oxygen species at the surface of the catalysts. Nucleophilic oxygen, like vanadyl oxygen, is required for the activation of propane and the formation of propylene. Formation of acrolein occurs via attack of propylene by electrophilic oxygen and it seems that this species are more abundant on the surface of VO_x/SiO_2 than on M1. Suppression of electrophilic oxygen during the reaction could stop the consecutive reactions of propylene and leads to a catalyst with high selectivity to propylene. Controlled formation of acrolein and further oxidation to acrylic acid is much more challenging, because it needs electrophilic oxygen and faces off the competitive oxidation of propylene to acetone and the consecutive oxidation to acetaldehyde.

The observed similarities and differences in the reaction mechanism of the three investigated model catalysts cannot be described only by structure elements (density of adsorption sites, different oxygen species) at the surface of the catalysts. Electronic properties of the three different catalysts with respect to charge carriers must be also taken into account, because these charge carriers are controlling/limiting the overall potential of the active structural elements at the surface. Targeted modification of the charge carrier transport will affect the kinetics of the reaction and will result in modified selectivity.

Interaction of the reactants with the surface of semiconducting M1, with V_xO_y clusters in the termination layer, leads to the formation of surface states. These states cause a band bending with the effect that the electron donor level of the hydrocarbon can be connected to the electron acceptor level of adsorbed oxygen sitting on defects. A self-limiting charge carrier transport situation is created and ensures that hydrocarbon oxidation and oxygen reduction occurs via charge carriers from the catalyst. The reservoir of charge carriers in the catalyst is filled up by charge carriers from the reactants.

V_xO_y on insulating SiO_2 is the opposite case to M1, because no electrons can be injected into or extracted from SiO_2 due to an energetic higher located conduction band or/and an energetic lower located valence band of the insulator compared to the acceptor and donor levels of the V_xO_y clusters. Catalytic reactions on this catalyst are the result of local exchange on monomeric and dimeric V_xO_y clusters with hydrocarbon and oxygen in close vicinity. Drawback of the small clusters is that partially activated oxygen (electrophilic oxygen) is in close vicinity to the active site for selective hydrocarbon oxidation and facilitates unselective pathways.

P/oCNT has no energy gap due to the semi-metal sp^2 carbon backbone. This leads to an unhindered charge carrier exchange between the di-ketonic groups (active site) and the sp^2 carbon skeleton. Selective operation is realized by localized electrons in the di-ketonic groups, which provides the required energy barrier. Mobile activated electrophilic oxygen from carbon combustion facilitates the unselective pathways to the carbon oxides and is the reason for the poor performance of the P/oCNT catalyst.

The presented work shows clearly that the local density of active (specific) structural elements at the surface (surface properties) connected to the electronic properties of the catalyst (bulk properties) are responsible for the performance of the catalyst. Obtained insight into the reaction network reveals a complex one with several steps including hydrogen abstraction, oxygen insertion, C-C bond breaking, decarbonylation, and decarboxylation reactions. Activation of oxygen and control of the abundance of activated oxygen are important factors for controlling the catalyst performance. The results of the study contribute to a better understanding of the performance of catalysts and will serve as a basis for new catalyst design concepts.

List of Figures

increased in the corresponding experiments to increase the reliability of acetic acid analysis.

Figure S 2-1 Switch between oxygen and argon with disaccording flow rates and pressures.

Figure S 2-2 Switch between oxygen and argon with harmonized flow rates and disaccording pressures.

Figure S 3-1 SEM image of the MoVTeNb M1 oxide catalyst.

Figure S 3-2 Experimental powder XRD patterns of the MoVTeNb M1 oxide catalyst and result of the Rietveld refinement (experiment in blue, simulation in red, difference calculated-experimental in black).

Figure S 3-3 Adsorption isotherms of nitrogen at T = 77 °C for M1, 6V/SBA-15, SBA-15, and P/oCNT.

Figure S 3-4 Metal concentration of tellurium, vanadium, and niobium in at% on the surface of M1 (0.6 nm inelastic mean free path (IMFP)) determined by photoelectron spectroscopy at T = 400 °C, p = 0.25 mbar, feed C_3H_8/O_2 = 2:1.

Figure S 3-5 Raman spectra of MoVTeNb M1 oxide (top), and 6V/SBA-15 (bottom) under reaction conditions of oxidative dehydrogenation of propane (T = 380 °C, feed $C_3H_8/O_2/He$ = 10/5/85). The absence of vibrational modes of V_2O_5 nano-crystals at 141, 282, 302, 407, 482, 527, 698 and 995 cm^{-1},[39] confirms high vanadium oxide dispersion.

Figure S 3-6 SEM image of P/oCNT.

Figure S 3-7 Raman spectrum of P/oCNT (excitation wavelength 632.8 nm and a laser power 20 mW).

Figure S 3-8 Surface abundance of oxygen, carbon and phosphorous determined by X-ray photoelectron spectroscopy for fresh and used P/oCNT.

Figure S 3-9 Conversion of a) propane at T = 400 °C (M1 and 6V/SBA-15) and 360 °C (P/oCNT), feed $C_3H_8/O_2/He$ = 10/5/85, W/F = 0.072 g s ml^{-1} (M1), 1.34 g s ml^{-1} (6V/SBA-15) and 2.0 g s ml^{-1} (P/oCNT), and b) ethane at T = 400 °C (M1 and 6V/SBA-15) and 360 °C (P/oCNT), feed $C_2H_6/O_2/He$ = 10/5/85,

List of Schemes

List of Tables

List of Equations

List of Abbreviations

BET	Adsorption isotherm model of Brunauer, Emmet and Teller
FCC	Fluid catalytic cracking
FID	Flame ionization detector
GC	Gas chromatograph
IMFP	Inelastic mean free path
IR	Infrared spectroscopy
KE	Kinetic energy
MS	Mass spectrometry
NLDFT	Non localized density functional theory
ODH	Oxidative dehydrogenation of hydrocarbons
ODE	Oxidative dehydrogenation of ethane
ODP	Oxidative dehydrogenation of propane
PTR-MS	Proton transfer reaction mass spectrometry
SE	Secondary electron
SEM	Scanning electron microscopy
TCD	Thermal conductivity detector
XPS	X-ray photoelectron spectroscopy
XRD	X-ray diffraction
XRF	X-ray fluorescence

List of Symbols

c	concentration
c_i^{ein}	Concentration of component i in the initial feed
D_e	Effective diffusion coefficient
D_i	Molecular diffusion coefficient of component i
d_P	Pore diameter
E_a	Apparent activation energy
F	Flow
k	Rate constant
n	Amount of substance
N	Number
r	Rate
$(r_{eff})_S$	Effective reaction rate based on the surface of the catalyst
$(r_{eff})_V$	Effective reaction rate based on the volume of the catalyst
R_o	Internal pipe radius
S	Selectivity
S_{BET}	Specific surface area
S_μ	Micropore surface area
t	Time
T	Temperature
V_P	Total pore volume
W	Mass of catalyst
X	Conversion
δ_K	Thickness of the catalyst layer
ν	Stoichiometric coefficient

Appendix

Publications

P. Kube, B. Frank, R. Schlögl, A. Trunschke

“Isotope Studies in Oxidation of Propane over Vanadium Oxide”

ChemCatChem **2017**, *9*, 3446-3455

Draft final version of this publication is used in this thesis

https://doi.org/10.1002/cctc.201700847

with permission from John Wiley and Sons.

P. Kube, B. Frank, S. Wrabetz, J. Kröhnert, M. Hävecker, J. Velasco-Vélez, J. Noack, R. Schlögl, A. Trunschke

„Functional Analysis of Catalysts for Lower Alkane Oxidation”

ChemCatChem **2017**, *9*, 573-585

Draft final version of this publication is used in this thesis

https://doi.org/10.1002/cctc.201601194

with permission from John Wiley and Sons.

A. Y. Klyushin, T. E. Jones, T. Lunkenbein, P. Kube, X. Li, M. Hävecker, A. Knop-Gericke, R. Schlögl

"Strong Metal Support Interaction as a key factor of Au activation in CO oxidation"

Submitted to Angewandte Chemie.

A. Trunschke, J. Noack, S. Trojanov, F. Girgsdies, T. Lunkenbein, V. Pfeifer, M. Hävecker, P. Kube, C. Sprung, F. Rosowski, R. Schlögl
„The Impact of the Bulk Structure on Surface Dynamics of Complex Mo–V-based Oxide Catalysts"
ACS Catalysis **2017**, *7*, 3061-3071.

J. J. Velasco-Vélez, V. Pfeifer, M. Hävecker, R. Wang, A. Centeno, A. Zurutuza, G. Algara-Siller, E. Stotz, K. Skorupska, D. Teschner, P. Kube, P. Braeuninger-Weimer, S. Hofmann, R. Schlögl, A. Knop-Gericke
„Atmospheric pressure X-ray photoelectron spectroscopy apparatus: Bridging the pressure gap"
Review of Scientific Instruments **2016**, *87*, 053121.

K. Amakawa, L. Sun, C. Guo, M. Hävecker, P. Kube, I. E. Wachs, S. Lwin, A. I. Frenkel, A. Patlolla, K. Hermann, R. Schlögl, A. Trunschke
„How Strain Affects the Reactivity of Surface Metal Oxide Catalysts"
Angewandte Chemie International Edition **2013**, *52*, 13553-13557.

M. Sanchez Sanchez, F. Girgsdies, M. Jastak, P. Kube, R. Schlögl, A. Trunschke
„Aiding the Self-Assembly of Supramolecular Polyoxometalates under Hydrothermal Conditions To Give Precursors of Complex Functional Oxides"
Angewandte Chemie International Edition **2012**, *51*, 7194-7197.

C. S. Guo, K. Hermann, M. Hävecker, J. P. Thielemann, P. Kube, L. J. Gregoriades, A. Trunschke, J. Sauer, R. Schlögl
„Structural Analysis of Silica-Supported Molybdena Based on X-ray Spectroscopy: Quantum Theory and Experiment"
Journal of Physical Chemistry C **2011**, *115*, 15449-15458.

Conference Contributions

June 2017

25th North American Catalysis Society Meeting, Denver

Talk: “Activation of hexagonal boron nitride in propane oxidation”

P. Kube, D. Teschner, F. Girgsdies, E. Willinger, T. Fu, R. Schlögl, A. Trunschke

March 2017

50th Annual German Catalysis Meeting, Weimar

Talk: “Mechanistic Studies of Propane Oxidation”

P. Kube, B. Frank, R. Schlögl, A. Trunschke

March 2016

49th Annual German Catalysis Meeting, Weimar

Poster: “Comparison of Vanadium Oxide-based and Metal-free Catalysts in the Oxidative Dehydrogenation of Ethane and Propane”

P. Kube, B. Frank, R. Naumann d’Alnoncourt, S. Wrabetz, A. Trunschke, R. Schlögl

August 2013

126th BASF International Summer Course, Ludwigshafen

Poster: “Comparative isotopic studies for exploring the reaction network of oxidative dehydrogenation of propane over model catalysts”

P. Kube, B. Frank, R. Schlögl, A. Trunschke

May 2013

112th Bunsentagung (Annual German Conference on Physical Chemistry), Karlsruhe

Poster: “Exploring the reaction network of oxidative dehydrogenation of propane over model catalysts using isotopic tracer studies”

P. Kube, B. Frank, R. Schlögl, A. Trunschke

March 2012

45th Annual German Catalysis Meeting, Weimar

Poster: “Comparative mechanistic studies on oxidative dehydrogenation of ethane and propane over model catalysts”

P. Kube, B. Frank, R. Naumann d’Alnoncourt, M. Sanchez Sanchez, T. Wolfram, R. Schlögl, A. Trunschke

Petershagen, 13th April 2018